Sapphire Fiber Optic Sensor for High Temperature Measurement

Zhipeng Tian

Dissertation submitted to the faculty of the Virginia Polytechnic Institute and State University in partial fulfillment of the requirements for the degree of

Doctor of Philosophy
In
Electrical Engineering

Anbo Wang, Chair
Masoud Agah
Yong Xu
Gary R Pickrell
Yizheng Zhu

November 30, 2017
Blacksburg

Keywords: Sapphire Fiber, Fabry-Perot, Interferometer, Thermal Radiation, Interrogator, Temperature Sensor

Sapphire Fiber Optic Sensor for High Temperature Measurement

Zhipeng Tian

ABSTRACT

This dissertation focuses on developing new technologies for ultra-low-cost sapphire fiber-optic high-temperature sensors. The research is divided into three major parts, the souceless sensor, the simple Fabry-Perot (F-P) interrogator, and the sensor system.

Chapter 1 briefly reviews the background of thermal radiation, fiber optic F-P sensors, and F-P signal demodulation. The research goal is highlighted.

In Chapter 2, a temperature sensing system is introduced. The environmental thermal radiation was used as the broadband light source. A sapphire wafer F-P temperature sensor head was fabricated, with an alumina cap designed to generate a stable thermal radiation field. The radiation-induced optical interference pattern was observed. We demodulated the temperature sensor by white-light-interferometry (WLI). Temperature resolution better than 1ºC was achieved.

Chapter 3 discusses a novel approach to demodulate an optical F-P cavity at low-cost. A simple interrogator is demonstrated, which is based on the scanning-white-light-interferometry (S-WLI). The interrogator includes a piece of fused silica wafer, and a linear CCD array, to transform the F-P demodulation from the optical frequency domain to the spatial domain. By using the light divergence of an optical fiber, we projected a tunable reference F-P cavity onto an intensity distribution along a CCD array. A model for S-WLI demodulation was established. Performance of the new S-WLI interrogator was investigated. We got a good resolution similar to the well-known traditional WLI.

At last, we were able to combine the above two technologies to a sapphire-wafer-based temperature sensor. The simple silica wafer F-P interrogator was optimized by focusing light to the image sensor. This approach improves the signal to noise ratio, hence allows the new integrator to work with the relatively weak thermal radiation field. We, therefore, proved in the experiment, the feasibility of the low-cost sourceless optical Fabry-Perot temperature sensor with a simple demodulation system.

Sapphire Fiber Optic Sensor for High Temperature Measurement

Zhipeng Tian

GENERAL AUDIENCE ABSTRACT

Temperature measurements for high temperature harsh environments is a challenge industrial task. In this work, a low-cost sapphire fiber high temperature sensor is introduced which uses single crystal sapphire fiber as the light guiding and a sapphire-wafer-based Fabry-Perot (F-P) interferometer as the temperature sensing element. The research goal is to provide an optical sensing system whose price is competitive to the high temperature thermocouples.

Two technologies were developed to reduce the cost of the sensing system, the sourceless sensor head design and the low-cost wafer-based F-P interrogator.

The sourceless sensor head makes use of the environmental thermal radiation as a broadband light source, together with the white light interferometry signal demodulation method, for temperature measurements. In this case, the system avoids using not only an external light, but also the light driver and the light coupling element.

A low-cost F-P cavity interrogation method was introduced to demodulate the sapphire-wafer-based temperature sensing F-P cavity. The signal demodulation is based on the scanning white light interferometry, but a reliable and low-cost reference F-P cavity is introduced. It includes only a piece of transparent wafer and a CCD array to transfer the interference fringe from the spectra domain to the spatial domain and therefore a low cost CCD can be directly applied to identify the optical path distance of the sensing OPD.

Eventually, the above two technologies were able to put together and an extremely low-cost F-P temperature sensing system was built. It has a good potential for further applications and commercialization.

Acknowledgement

First of all, I would like to express my greatest gratitude to my advisor, Dr. Anbo Wang, for providing me this great opportunity to work with such a good team at CPT. I am indebted and thankful for his continuous help, guidance, and support throughout my entire Ph.D. life. I have learned so many great things from him, in every aspect of the research and the professional life. He sets a good model for me, which will benefit my entire life.

I would like to thank my other committee professors, Dr. Gary Pickrell, Dr. Masoud Agah, Dr. Yizheng Zhu and Dr. Yong Xu for their tremendous teaching in the classes and the assistance in the Ph.D. project. I would express my gratitude to my project manages, Dr. Cheng Ma and Dr. Zhihao Yu for their wonderful help in my research.

I would like to thank my project partners Dr. Brian Scott and Dr. Adam Floyd. Special thank goes to Guo Yu and Georgi Ivanov who gave me a hand in hand help in the first step of my research at CPT.

I would like to thank my dearest friends at CPT, Bo Dong, Di Hu, Chengnan Hu, Li Yu, Lingmei Ma, Bo Liu, Chaofan Wang, Jing Wang, Nan Wu, Ruohui Wang, and Amiya Behera for their great help and friendship in the past six years. Thanks also extend to Shuo Yang, Jiaji He, Ziang Feng, Chengshuai Li, Shichao Chen, Peng Lv, Yuanyuan Guo, Haifeng Xuan, Chengyuan Hu, Tong Qiu, Shan Jiang, Yun Dong, Yunbin Song, Yujie Cheng, Dorothy Wang, Kathy Wang, Michael Fraser, Cary Hill, and Aram Lee. Thank you for your help and friendship.

I would extend my thanks to my good friends in Blacksburg who provided me great help, Bo Chen, Fang Wang, Yuan Zhou, Li Gui, Wenle Li, Menghui Li, Shunan Zhao, Yuchang Wu, Yanjun Ma, and Qingzhao Wang.

I would like to express my deepest gratitude to my parents, who give me unreserved love, encouragement, and support to let me go this far.

Table of Contents

List of Figures

List of Tables

CHAPTER 1 Background

1.1 Introduction to Optical-fiber-based Ultra-high Temperature Sensors

Fiber optic sensors, which use an optical fiber to interact with the physical environmental parameters and transport light, have attracted much attention in the past 40 years [1, 2]. To date, they have been deployed in a variety of applications, such as temperature, pressure, strain, vibration, chemical components, gas, biomedicine, and electromagnetic field. As a new type of sensors, they have shown significant intrinsic advantages over the traditional sensors, such as the miniature size, the flexibility, the electromagnetic field immunity, and the capability of distributed sensing, etc. Besides, fiber optic sensors, in many applications, offer high resolution, large dynamic range, long lifetime, and stable performance. Because of these advantages, they are playing important roles in the fields where the traditional sensors, such as the semiconductor sensors and the electrical sensors, cannot work.

Ultra-high temperature sensing in a harsh environment is a challenging industrial task. The environment is harsh when it has a high temperature, high pressure, extensive corrosion, or strong electromagnetic field. The temperature is the most important parameter in industry. When the temperature rises higher than 1500ºC, only a few sensors can be used, such as thermocouples, pyrometers, and specially designed fiber optic sensors. For example, in a typical coal-gasifier environment, with high temperature, high pressure and intensive corrosion, a rare-metal Pt-Pb thermocouple last only two weeks, on average. The remote pyrometers suffer from poor resolution and unstable performance. Fiber optic sensors, especially single-crystal sapphire fiber optic sensors, show a good potential in such applications.

Silica-fiber-based temperature sensors, usually, cannot function beyond 1000°C due to the instability issues, such as the devitrification [3, 4], the dopant diffusion [5, 6], the internal stress release [7, 8], and the refractive index change [9]. Therefore, single-crystal sapphire fiber, which melts at 2030°C, is a good choice in the environment where the temperature is higher than 1200°C. Sapphire fiber optic sensors have attracted much attention as a competitive candidate for temperature measurements because of their promising characteristics, such as miniaturization, thermal stability, excellent mechanical property, and a corrosion-resistant nature. These features are highly desirable for applications in harsh environments. In this dissertation, the effort is focused on the sapphire fiber based ultra-high-temperature sensors

The radiation thermometer [10-13], the sapphire fiber Bragg Grating (SFBG) [14-16], and the extrinsic Fabry-Perot interferometer (EFPI) [17-19] are three main types of fiber optic temperature sensors built with sapphire fiber that measures temperatures higher than 1500°C. The sapphire-fiber-based radiation thermometers were first developed to meet the demanding needs for measuring temperatures at targets deeply embedded in hazardous systems. Section 1.2 will discuss this sensor in detail.

The SFBG, fabricated by a femtosecond laser [20-22] is another type of high-temperature sensor. The Bragg grating is created using a phase mask [23, 24] or potentially under a point-by-point procedure[25]. It follows the traditional fiber FBG fabrication process. The femtosecond laser inscribes permanent physical damages inside the sapphire fiber. Given the stability of a sapphire fiber, the SFBGs, theoretically, can function at ultra-high temperatures. The principle of an SBFG is the same as those made in the single mode silica fibers [26]. A broadband light propagates in the fiber with an SFBG, will reflect a narrow linewidth spectrum, according to the wavelength constructive interference. The spectral peak position of the SFBG determines the temperature or strain. However, due to an extremely large mode volume, and the inter-modal conversion effect in the highly multimode sapphire fiber, an SFBG reflects a relatively broad spectral peak. Therefore, the temperature resolution of an SFBG is not as good as a single mode fiber FBG. Grobnic et al., have improved the SFBG performance by exciting only low order modes in the sapphire fiber using a tapered single-mode fiber [16]. The SFBG, in this case, shows a narrower spectral peak. Another approach to achieve a narrow-linewidth peak is to eliminate high order modes via coiling the fiber [27]. However, the surface scattering of a sapphire fiber generates higher order modes as light propagates along the fiber [28]. Based on the published work [16], the low-order-mode excitation can propagate only approximately 20 cm in the sapphire fiber. This limits the application of the SFBG as a temperature sensor. The SFBG, as the sensing element, requires being installed in high-temperature regions. However, the sapphire to silica fiber connection needs to be placed in a lower temperature region. The 20 cm length in many applications is not long enough for the fiber connection to be at a safe temperature. In addition to temperature sensing, SFBGs provide an opportunity to measure high-temperature strains [15, 29]. However, the temperature-strain cross sensitivity issue needs to be considered in practice. To date, the performance of SFBGs is one of the bottlenecks that limits their applications in the market.

In this work, the efforts are focused on the sapphire-fiber-based Fabry-Perot (F-P) temperature sensors. Fiber F-P is one of most promising fiber optic sensor structures due to its simplicity, good stability, and extremely high resolution. Wang et al. demonstrated both intrinsic Fabry-Perot interferometer (IFPI) [30, 31] and extrinsic Fabry-Perot interferometer (EFPI) [32], by using a section of sapphire fiber or an air gap as the F-P cavity. After that, this type of sensor has been improved a lot by constructing compact and reliable air cavities [17] and solid wafer F-Ps [18, 33, 34]. However, as a temperature sensor, the solid single-crystal-wafer F-P cavity functions better than an air gap cavity since the wafer is thermally and chemically stable, and strain insensitive. As a result, the sapphire wafer F-P can be a pure temperature sensor with no cross-sensing issue. Besides the structure, signal demodulation of the optical Fabry-Perot interferometer was continuously developing in the past ten years [35-37]. An F-P interferometer for pico-meter scale measurement has been achieved [38].

Except for the single-crystal sapphire fiber optic sensor, Shen et al. [39] reported a lab-made single-crystal zirconia optical fiber for ultra-high temperature sensing. The zirconia fiber was fabricated by laser-heated pedestal growth method [40], similar to the technology developed for sapphire fibers. Compare to sapphire, single-crystal zirconia has a higher melting point. The zirconia-fiber-based radiation thermometer was demonstrated up to 2300°C [41, 42]. Later, the fiber drawing technique was improved by adding proper dopants to stabilize the zirconia fiber structure [43-46]. However, mechanically, zirconia is softer than sapphire. It shows weaker chemical stability as well, which limits its applications in high temperature and corrosion intensive harsh environments. After some initial publications, no more work was reported about the single crystal zirconia fiber.

1.2 Fiber Optic Thermal Radiation Thermometers

The fiber optic radiation thermometer is one of the earliest temperature sensors made with optical fibers [11-13]. In this part, we discuss only the sapphire-fiber-based radiation thermometers because silica fiber sensors cannot work at ultra-high temperature, limited by their physical and chemical properties. Sapphire-fiber radiation thermometers were developed to measure temperatures at targets deeply embedded in the harsh systems, such as coal gasifiers and engines. The sensing principle is the same as the traditional radiation temperature sensors. Instead of a remote sensing construction, it uses a sapphire fiber to guide the thermal radiation from a hot emitter to a detector.

As a radiation thermometer, Planck's Law governs the thermal radiation spectrum, if an emitter can be considered as an ideal blackbody. It describes that both the spectral pattern and the peak position are a function of temperature. The spectral peak moves to a shorter wavelength as temperature increases. Because of this, radiation thermometers, developed in the early age, detected the peak position to deduce the temperature [41]. However, this method requires recording a wide spectrum with a peak. Besides, indicating temperature by only one peak in the broad spectrum is not accurate. The sensor accuracy was improved by two-color thermometry [47] method. One can calculate the temperature via the intensity ratio of two different wavelengths.

In the actual applications, it was discovered that the radiation spectra are materials dependent. Planck's Law only applies to the ideal blackbodies. In fact, it is difficult to use a radiation thermometer if the environment or the sensing medium has a low emission, such as in a gas environment or with the transparent materials. The sapphire fiber is usually transparent at the wavelength of interest. Therefore, for temperature measurement, an emitter with a good emissivity is needed. The emitter is placed in the high-temperature region or is mounted on the target. In this case, the target temperature is determined by measuring the radiation of the emitter. In the early designs, the emitters were simply attached at the end of the sapphire fiber. Later, researchers fabricated the blackbody cavities directly on the fiber end, by depositing a layer of Pt, Ir, or compound layers [11], to form the emitter. This construction benefits from miniature size, good mechanical stability, and easy fabrication. So far, it is the best construction for the sapphire-fiber radiation thermometer. Besides the sapphire fiber, single crystal zirconia fibers were investigated [48].

Although radiation thermometers have been invented for more than thirty years, two major issues limit their actual applications. According to the Stefan-Boltzmann law, the radiation intensity of a blackbody is proportional to the fourth power of its temperature. Therefore, the radiation power reduces rapidly when the target temperature cools down. Once the background noises, including the radiation from the ambient environment and the thermal noise of the photodetector, are dominant, the radiation thermometer cannot provide a good accuracy anymore or even fail to work. In the published work [13], the low-temperature limit of a sapphire fiber thermometer is ~500°C. This issue is addressed by combining a fluorescence-based algorithm [13, 49-51], together with the radiation thermometer, to extend the temperature range. In this situation, a dopant is added to the blackbody cavity. A pulsed laser excites the dopant fluorescence. One calculates the low-temperature via the temperature-dependent fluorescence decay.

Another limitation to the radiation thermometer is the stability of the optical spectra, which is determined by the emitter, or the blackbody cavity. An emitter, even delicately designed, can never be an ideal blackbody. As described before, Planck's Law does not exactly govern the appearance of the radiation spectra. Because of this, a calibration is needed. The radiation thermometer faces an issue that the indicated temperature drifts from the actual temperature if the recorded spectrum does not match what is calibrated. The drift could happen in several situations, such as when the component of the radiator changes, the metal-film blackbody cavity decays with time [52], and additional absorption spectrum introduced by the contaminations on the sapphire fiber surface.

Because of the two major limitations, the sapphire-fiber radiation thermometer is not competitive, compared to the rare-metal-based high-temperature thermocouples. It has not been widely used in today's market.

1.3 Signal Demodulation of the Fiber Optic Fabry-Perot Interferometers

The optical fiber Fabry-Perot Interferometer (FPI) is one of the most important fiber optic sensor structures. It provides high precision measurements of displacement and distance. Optical Path Distance (OPD) is commonly used in the publication. The OPD calculation is essential since a fiber optic F-P sensor usually works by relating its OPD to the physical parameters being measured.

Owing to the development of the signal demodulation algorithms in the past ten years, highly precise OPD calculation has been achieved. There are two major OPD calculation algorithms, the relative and the absolute demodulation. The relative measurement only calculates the OPD change; while the absolute measurement provides an actual OPD value. In some situations, relative measurement is enough. However, in many applications, especially in the cases of temperature and pressure sensing, the absolute measurement is essential.

1.3.1 Relative OPD Demodulation

Several methods were developed for relative OPD calculation. Typical examples were applied in the Scanning Probe Microscopy, such as atomic force microscopy [53-55], in which a monochromic laser is chosen as the light source. One needs to know only the length differences with respect to the reference. Such applications are intensity-based measurements. As a result, it suffers from the laser intensity instability and other noises from the optical system. Besides, relative measurement requires the OPD variation shorter than the half wavelength of the laser. Otherwise, a phase ambiguity issue occurs. Quadrature detection is widely applied for demodulating OPD relatively. This method can be used for dynamic measurement, providing a high resolution and a large dynamic range. Haider et al. [56], achieved a resolution as high as $2\,fm/\sqrt{Hz}$. One way to realize the quadrature detection is to use two lasers. Similar to the one laser system, only the laser intensity is recorded. Hence, it suffers from the laser intensity noise and optical system noise as well.

The applications of relative OPD detection is quite limited. Although it can achieve a high resolution, usually, the signal demodulation algorithm requires the system to work continuously. This strict requirement prevents its practicability for industrial applications.

1.3.2 Absolute OPD Demodulation

The absolute OPD Demodulation calculates the actual length of a Fabry-Perot cavity. The white light interferometry (WLI) is a widely used algorithm for fiber optic sensors. WLI requires a broadband light source or a wavelength-swept laser. If a broadband light source, such as a low coherent LED or a supercontinuum LED, is chosen, a spectrometer or a monochromator will be employed to record the full optical spectrum. When using a wavelength-swept laser, a photodetector will be applied to acquire the intensity at each wavelength. Anyway, recording a full-length spectrum for WLI demodulation is essential.

With the full optical spectrum, researchers have developed several algorithms to calculate OPDs precisely. In 1992, Chen et al. [57] published a process to track the peak position of an interference fringe. This method is applicable only when one interferometric peak exhibited in the full spectral range, and the OPD change is no more than one wavelength. Otherwise, the OPD demodulation shows ambiguity. This approach was developed as the peak-to-peak method, in which two adjacent fringe peaks, are tracked [58]. The peak-tracking method suffers from a relatively low resolution because it uses only a section of the entire spectrum. As a different approach, using the Fast Fourier Transform (FFT) peak to determine the OPD was developed [59]. Compared to the peak-to-peak tracking method, the FFT approach uses the entire data points to improve the accuracy by interpolating and linear regression. Qi et al., propose to combine the peak-to-peak tracking and the FFT methods to increase the accuracy further. However, this improvement does not eventually solve the fringe order ambiguity. The concept of "additional phase" was first discovered by Han et al. [28] in the fiber-based EFPIs. Further discussion shows that the additional phase is a function of OPD and the angular optical power distribution [60]. Based on the discovery, a jump of the interference fringe order, which is shown as the 2π difference in phase, is inevitable in any actual Fabry-Perot optical sensor [61]. However, if the signal to noise ratio is sufficiently high [62], the probability of jump is negligible, then the fiber-based FPIs shows nearly no fringe-order ambiguity.

The other major procedure for absolute OPD demodulation is scanning white light interferometry (S-WLI) [63-65]. In this technique, a broadband light source is required as well. Instead of obtaining a full-length spectrum, another reference interferometer, with an OPD scanning capability, connects with the target interferometer in series. The maximum value of the total interference is achieved when the OPDs of the two interferometers match each other [66, 67]. As a result, the absolute value of the target OPD is determined from the known reference scanning interferometer. However, this process is sometimes even more expensive than the traditional WLI with a spectrometer, because a reliable and repeatable scanning interferometer is difficult to build, especially in the case when the OPD value needs to change at ultra-high precision.

1.4 Research Goal

The fiber optic Fabry-Perot sensor requires two critical components, the light source, and the interrogator. Both of them are expensive in the system. Take the spectrometer as an example. A compact and so-call low-cost Ocean Optics spectrometer is near \$3,000 on the market. A broadband light source, together with the driver, cost approximately \$500. The drawbacks limit the fiber optic F-P sensors in the cost-sensitive applications.

The goal of this research focuses on designing a low-cost sapphire fiber Fabry-Perot temperature sensor, aiming at reducing the entire cost by order of magnitude. To achieve the goal, we need to develop a novel optical system, as well as establish a new algorithm for signal demodulation.

1.5 Reference

1. V. Vali, and R. Shorthill, "Fiber ring interferometer," Applied optics **15**, 1099-1100 (1976).
2. A. Rogers, "Optical methods for measurement of voltage and current on power systems," Optics & Laser Technology **9**, 273-283 (1977).
3. A. Rose, "Devitrification in annealed optical fiber," J. Lightwave Technol. **15**, 808-814 (1997).
4. P. Bouten, and G. De With, "Crack nucleation at the surface of stressed fibers," Journal of applied physics **64**, 3890-3900 (1988).
5. K. Shiraishi, Y. Aizawa, and S. Kawakami, "Beam expanding fiber using thermal diffusion of the dopant," Lightwave Technology, Journal of **8**, 1151-1161 (1990).
6. J. W. Fleming, C. R. Kurkjian, and U. C. Paek, "Measurement of cation diffusion in silica light guides," Journal of the American Ceramic Society **68** (1985).
7. J. Stone, "Stress-optic effects, birefringence, and reduction of birefringence by annealing in fiber Fabry-Perot interferometers," J. Lightwave Technol. **6**, 1245-1248 (1988).
8. A. Yablon, M. Yan, P. Wisk, F. DiMarcello, J. Fleming, W. Reed, E. Monberg, D. DiGiovanni, J. Jasapara, and M. Lines, "Refractive index perturbations in optical fibers resulting from frozen-in viscoelasticity," Applied physics letters **84**, 19-21 (2004).
9. J. Juergens, G. Adamovsky, R. Bhatt, G. Morscher, and B. Floyd, "Thermal evaluation of fiber Bragg gratings at extreme temperatures," in *43rd AIAA Aerospace Science Meeting and Exhibit, Reno, NV*(2005).

10. M. Gottlieb, and G. B. Brandt, "Fiber-optic temperature sensor based on internally generated thermal radiation," Applied Optics **20**, 3408-3414 (1981).

11. R. R. Dils, "High‐temperature optical fiber thermometer," Journal of Applied Physics **54**, 1198-1201 (1983).

12. Z. Zhang, K. Grattan, and A. Palmer, "Fiber optic temperature sensor based on the cross referencing between blackbody radiation and fluorescence lifetime," Review of scientific instruments **63**, 3177-3181 (1992).

13. Y. Shen, L. Tong, Y. Wang, and L. Ye, "Sapphire-fiber thermometer ranging from 20 to 1800 C," Applied optics **38**, 1139-1143 (1999).

14. D. Grobnic, S. J. Mihailov, C. W. Smelser, and D. Huimin, "Sapphire fiber Bragg grating sensor made using femtosecond laser radiation for ultrahigh temperature applications," Photonics Technology Letters, IEEE **16**, 2505-2507 (2004).

15. V. P. Wnuk, A. Méndez, S. Ferguson, and T. Graver, "Process for mounting and packaging of fiber Bragg grating strain sensors for use in harsh environment applications," in *Smart Structures and Materials*(International Society for Optics and Photonics2005), pp. 46-53.

16. D. Grobnic, S. J. Mihailov, H. Ding, F. Bilodeau, and C. W. Smelser, "Single and low order mode interrogation of a multimode sapphire fibre Bragg grating sensor with tapered fibres," Measurement Science and Technology **17**, 980 (2006).

17. H. Xiao, J. Deng, G. Pickrell, R. G. May, and A. Wang, "Single-crystal sapphire fiber-based strain sensor for high-temperature applications," J. Lightwave Technol. **21**, 2276 (2003).

18. Y. Zhu, Z. Huang, F. Shen, and A. Wang, "Sapphire-fiber-based white-light interferometric sensor for high-temperature measurements," Opt. Lett. **30**, 711-713 (2005).

19. J. Wang, B. Dong, E. Lally, J. Gong, M. Han, and A. Wang, "Multiplexed high temperature sensing with sapphire fiber air gap-based extrinsic Fabry?Perot interferometers," Opt. Lett. **35**, 619-621 (2010).

20. C. Liao, and D. Wang, "Review of femtosecond laser fabricated fiber Bragg gratings for high temperature sensing," Photonic Sensors, 1-5 (2013).

21. M. Busch, W. Ecke, I. Latka, D. Fischer, R. Willsch, and H. Bartelt, "Inscription and characterization of Bragg gratings in single-crystal sapphire optical fibres for high-temperature sensor applications," Measurement Science and Technology **20**, 115301 (2009).

22. D. Grobnic, S. J. Mihailov, and C. Smelser, "Sapphire thermal radiation sensor based on femtosecond induced Bragg gratings," in *Bragg Gratings, Photosensitivity, and Poling in Glass Waveguides*(Optical Society of America2010), p. JThA35.

23. K. O. Hill, B. Malo, F. Bilodeau, D. Johnson, and J. Albert, "Bragg gratings fabricated in monomode photosensitive optical fiber by UV exposure through a phase mask," Applied Physics Letters **62**, 1035-1037 (1993).

24. S. J. Mihailov, C. W. Smelser, P. Lu, R. B. Walker, D. Grobnic, H. Ding, G. Henderson, and J. Unruh, "Fiber Bragg gratings made with a phase mask and 800-nm femtosecond radiation," Opt. Lett. **28**, 995-997 (2003).

25. G. D. Marshall, R. J. Williams, N. Jovanovic, M. Steel, and M. J. Withford, "Point-by-point written fiber-Bragg gratings and their application in complex grating designs," Opt. Express **18**, 19844-19859 (2010).

26. K. O. Hill, and G. Meltz, "Fiber Bragg grating technology fundamentals and overview," J. Lightwave Technol. **15**, 1263-1276 (1997).

27. C. Zhan, J. Kim, S. Yin, P. Ruffin, and C. Luo, "High temperature sensing using higher-order-mode rejected sapphire fiber gratings," Optical Memory and Neural Networks **16**, 204-210 (2007).

28. M. Han, and A. Wang, "Exact analysis of low-finesse multimode fiber extrinsic Fabry-Perot interferometers," Applied optics **43**, 4659-4666 (2004).

29. S. J. Mihailov, D. Grobnic, and C. W. Smelser, "High-temperature multiparameter sensor based on sapphire fiber Bragg gratings," Opt. Lett. **35**, 2810-2812 (2010).

30. A. Wang, S. Gollapudi, K. A. Murphy, R. G. May, and R. O. Claus, "Sapphire-fiber-based intrinsic Fabry–Perot interferometer," Opt. Lett. **17**, 1021-1023 (1992).

31. A. Wang, S. Gollapudi, R. May, K. Murphy, and R. Claus, "Advances in sapphire-fiber-based intrinsic interferometric sensors," Opt. Lett. **17**, 1544-1546 (1992).

32. A. Wang, S. Gollapudi, R. G. May, K. A. Murphy, and R. O. Claus, "Sapphire optical fiber-based interferometer for high temperature environmental applications," Smart Materials and Structures **4**, 147 (1995).

33. Y. Zhang, G. R. Pickrell, B. Qi, A. Safaai-Jazi, and A. Wang, "Single-crystal sapphire-based optical high-temperature sensor for harsh environments," OPTICE **43**, 157-164 (2004).

34. Y. Zhu, and A. Wang, "Surface-mount sapphire interferometric temperature sensor," Applied optics **45**, 6071-6076 (2006).

35. M. Schmidt, and N. Fürstenau, "Fiber-optic extrinsic Fabry–Perot interferometer sensors with three-wavelength digital phase demodulation," Opt. Lett. **24**, 599-601 (1999).

36. J. Jiang, T. Liu, Y. Zhang, L. Liu, Y. Zha, F. Zhang, Y. Wang, and P. Long, "Parallel demodulation system and signal-processing method for extrinsic Fabry–Perot interferometer and fiber Bragg grating sensors," Opt. Lett. **30**, 604-606 (2005).

37. B. Qi, G. R. Pickrell, J. Xu, P. Zhang, Y. Duan, W. Peng, Z. Huang, W. Huo, H. Xiao, and R. G. May, "Novel data processing techniques for dispersive white light interferometer," OPTICE **42**, 3165-3171 (2003).

38. X. Zhou, and Q. Yu, "Wide-range displacement sensor based on fiber-optic Fabry–Perot interferometer for subnanometer measurement," IEEE sensors journal **11**, 1602-1606 (2011).

39. L. Tong, Y. Shen, L. Ye, and Z. Ding, "A zirconia single-crystal fibre-optic sensor for contact measurement of temperatures above 2000° C," Measurement Science and Technology **10**, 607 (1999).

40. M. Fejer, J. Nightingale, G. Magel, and R. Byer, "Laser‐heated miniature pedestal growth apparatus for single‐crystal optical fibers," Review of scientific instruments **55**, 1791-1796 (1984).

41. H. Tominaga, M. Tanaka, M. Koshino, and H. Ishibashi, "Radiation type thermometer," (Google Patents, 1992).

42. J. Fraden, "Radiation thermometer and method for measuring temperature," (Google Patents, 1989).

43. L. Tong, "Growth of high-quality Y 2 O 3–ZrO 2 single-crystal optical fibers for ultra-high-temperature fiber-optic sensors," Journal of crystal growth **217**, 281-286 (2000).

44. L. Tong, "Single-crystal Y2O3-ZrO2 rectangular waveguides for ultrahigh-temperature sensing applications," Applied Optics **41**, 3804-3808 (2002).

45. L. Tong, J. Lou, and E. Mazur, "High-quality rectangular Y2O3-ZrO2 single-crystal optical waveguides for high-temperature fiber optic sensors," in *Environmental and Industrial Sensing*(International Society for Optics and Photonics2002), pp. 251-258.

46. L. Tong, L. Ye, J. Lou, Z. Shen, Y. Shen, and E. Mazur, "Improved Y2O3-ZrO2 waveguide fiber optic sensor for measuring gas-flow temperature above 2000 degrees Celsius," (2002), pp. 392-399.

47. D. P. DeWitt, and G. D. Nutter, *Theory and practice of radiation thermometry* (Wiley Online Library, 1988).

48. Z. Wang, and B. Adams, "Apparatus and method for monitoring a temperature using a thermally fused composite ceramic blackbody temperature probe," (Google Patents, 1994).

49. K. Grattan, "The use of fibre optic techniques for temperature measurement," Measurement and Control **20**, 32-39 (1987).

50. H. Seat, J. Sharp, Z. Zhang, and K. Grattan, "Single-crystal ruby fiber temperature sensor," Sensors and Actuators A: Physical **101**, 24-29 (2002).

51. H. Aizawa, N. Ohishi, S. Ogawa, T. Katsumata, S. Komuro, T. Morikawa, and E. Toba, "Fabrication of ruby sensor probe for the fiber-optic thermometer using fluorescence decay," Review of scientific instruments **73**, 3656-3658 (2002).

52. S. L. Firebaugh, K. F. Jensen, and M. Schmidt, "Investigation of high-temperature degradation of platinum thin films with an in situ resistance measurement apparatus," Microelectromechanical Systems, Journal of **7**, 128-135 (1998).

53. D. Rugar, H. J. Mamin, and P. Guethner, "Improved fiber‐optic interferometer for atomic force microscopy," Applied Physics Letters **55**, 2588-2590 (1989).

54. A. Oral, R. A. Grimble, H. Ö. Özer, and J. B. Pethica, "High-sensitivity noncontact atomic force microscope/scanning tunneling microscope (nc AFM/STM) operating at subangstrom oscillation amplitudes for atomic resolution imaging and force spectroscopy," Review of Scientific Instruments **74**, 3656-3663 (2003).

55. N. Suehira, Y. Tomiyoshi, Y. Sugawara, and S. Morita, "Low-temperature noncontact atomic-force microscope with quick sample and cantilever exchange mechanism," Review of Scientific Instruments **72**, 2971-2976 (2001).

56. H. I. Rasool, P. R. Wilkinson, A. Z. Stieg, and J. K. Gimzewski, "A low noise all-fiber interferometer for high resolution frequency modulated atomic force microscopy imaging in liquids," Review of Scientific Instruments **81**, 023703 (2010).

57. S. Chen, A. Palmer, K. Grattan, and B. Meggitt, "Digital signal-processing techniques for electronically scanned optical-fiber white-light interferometry," Applied optics **31**, 6003-6010 (1992).

58. B. T. Meggitt, "Fiber optic white-light interferometric sensors," in *Optical Fiber Sensor Technology*, K. T. V. Grattan, and B. T. Meggitt, eds. (Springer Netherlands, 1995), pp. 269-312.

59. B. L. Danielson, and C. Boisrobert, "Absolute optical ranging using low coherence interferometry," Applied Optics **30**, 2975-2979 (1991).

60. C. Ma, B. Dong, J. Gong, and A. Wang, "Decoding the spectra of low-finesse extrinsic optical fiber Fabry-Perot interferometers," Opt. Express **19**, 23727-23742 (2011).

61. C. Ma, E. M. Lally, and A. Wang, "Toward Eliminating Signal Demodulation Jumps in Optical Fiber Intrinsic Fabry?Perot Interferometric Sensors," J. Lightwave Technol. **29**, 1913-1919 (2011).

62. C. Ma, "Modeling and Signal Processing of Low-Finesse Fabry-Perot Interferometric Fiber Optic Sensors," (2012).

63. A. Harasaki, J. Schmit, and J. C. Wyant, "Improved vertical-scanning interferometry," Applied optics **39**, 2107-2115 (2000).

64. C. Belleville, and G. Duplain, "White-light interferometric multimode fiber-optic strain sensor," Opt. Lett. **18**, 78-80 (1993).

65. S. Wang, T. Liu, J. Jiang, K. Liu, J. Yin, Z. Qin, and S. Zou, "Zero-fringe demodulation method based on location-dependent birefringence dispersion in polarized low-coherence interferometry," Opt. Lett. **39**, 1827-1830 (2014).

66. S. Chen, B. Meggitt, and A. Rogers, "Electronically scanned optical-fiber Young's white-light interferometer," Opt. Lett. **16**, 761-763 (1991).

67. K. G. Larkin, "Efficient nonlinear algorithm for envelope detection in white light interferometry," JOSA A **13**, 832-843 (1996).

CHAPTER 2 Sourceless Fabry-Perot Temperature Sensor

2.1 Introduction to the Thermal Radiation

2.1.1 Plancks Law

Thermal radiation is a phenomenon that any material at temperature higher than 0 K emits a radiation field. It originates from the kinetic energy of the atoms/molecules. Moden physics has proven that the thermal radiation is an electromagnetic wave, a result of the charge acceleration or dipole oscillation [1]. The average kinetic energy of the atoms indicates temperature. Therefore, the thermal radiation spectrum is temperature dependent.

The thermal radiation was first described by Wien approximation [2] in the short wavelength range and Rayleigh-Jeans Law in the long wavelengths [3]. Neither of them was able to describe the entire radiation spectrum. Later, Planck combined the two laws by introducing the concept of Quanta, known as Planck's Law. Planck's Law characterizes the whole thermal radiation spectrum, in theory, from ultraviolet to infrared.

According to Planck's Law, the frequency spectra (B_v) of a blackbody radiation, relates to the absolute temperature (*T)* by,

$$B_v(\nu,T)=\frac{2h\nu^3}{c^2}\frac{1}{e^{\frac{h\nu}{k_BT}}-1} \tag{2.1}$$

Here *h* is Planck's constant; and k_B is Boltzmann constant. *v* represents light frequency. In practice, The Planck's law is commonly expressed by using wavelength λ as the variable,

$$B_v(\lambda,T)=\frac{2hc^2}{\lambda^5}\frac{1}{e^{\frac{hc}{\lambda k_BT}}-1} \tag{2.2}$$

According to Equation (2.2), one can draw the radiation spectra at different temperatures. *Figure 2-1* illustrates the radiation spectra at 700ºC, 1000 ºC, 1300 ºC, and 1600 ºC, respectively. The peak positions show a clear blue shift at a higher temperature. In other words, the power distribution of the thermal radiation moves to the shorter wavelength at a higher temperature.

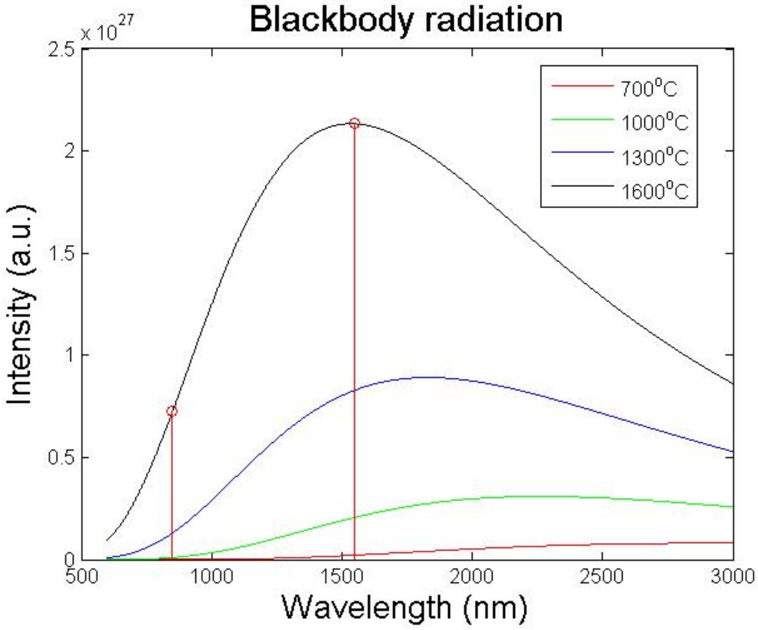

Figure 2-1 Simulation of the thermal radiation spectra at 700ºC, 1000 ºC, 1300 ºC, and 1600 ºC, respectively.

2.1.2 Blackbody

Planck's law works well if an emitter is a blackbody. A blackbody is the definition of an ideal material which absorbs all the radiations illuminate it. In this case, at thermal equilibrium, a blackbody must radiate energy as well, which is called the blackbody radiation. When this happens, the radiational spectral field follows the Kirchhoff's law of thermal radiation, which indicates that a blackbody emits all the light power absorbed as the electromagnetic waves in the thermodynamic equilibrium status.

Hence, the blackbody radiation spectrum is dimensionless but only relates to its temperature. An important parameter, the coefficient of emittance $\varepsilon(\lambda)$, is defined by [4],

$$E(\lambda,T)=\varepsilon(\lambda)E_b(\lambda,T) \tag{2.3}$$

The actual radiation spectrum $E(\lambda,T)$ relates to the theoretical blackbody radiation spectrum $E_b(\lambda,T)$ by the coefficient of emittance $\varepsilon(\lambda)$. In fact, $\varepsilon(\lambda)$ for an actual material, is affected by its surface condition and the wavelength of interest; and it is usually smaller than 1. Such material is also called the gray body [5]. It has been noticed that $\varepsilon(\lambda)$ varies a lot for different materials.

According to the Kirchhoff's law, there is a relationship between the emittance $\varepsilon(\lambda)$ and the absorptance $\alpha(\lambda)$ of the materials, under the equilibrium status [6],

$$\alpha(\lambda)=\varepsilon(\lambda)=\frac{E}{E_b} \tag{2.4}$$

$\alpha(\lambda)=\varepsilon(\lambda)$ describes the Kirchhoff's Law of radiation mathematically, which indicates that the blackbody's emission and absorption spectrum must be absolutely the same. Therefore, a good emitter must be a good absorber as well.

2.2 Thermal-Radiation-Induced Interference

2.2.1 Coherent Thermal Radiation

Thermal radiation, as an electromagnetic wave, is coherent. The quantum theory established the coherent property of the spontaneous radiation, as early as the 1950s [7]. Quantum Mechanical models were built to analyze the coherent and incoherent properties of the radiation field [8], including the blackbody radiation. The coherent length of thermal radiation is temperature dependent. In 1995, Peter et al. [9], investigated the coherent thermal radiation effects in the thin film Fabry-Perot structures. In which, the thin film thickness was set the same order of magnitude as the coherent length. Clear radiation interference pattern was also observed in a plane and parallel resonator [10] from 4 to 16μm.

2.2.2 Principle of the Sourceless Fabry-Perot Interferometer

The analysis in theory and the successful investigations of the coherent thermal radiation inspire us to design a radiation-based interferometric sensor. In this study, we create a sourceless sapphire fiber Fabry-Perot interferometric temperature sensor, by using the broadband thermal radiation to generate an interference pattern. We acquired the optical spectrum at ~850nm. Thus, a low-cost silicon CCD camera is commercially available.

The schematic of the sourceless wafer-based extrinsic Fabry-Perot interferometer is shown in *Figure 2-2*. The environmental thermal radiation illuminates a sapphire wafer F-P cavity from one side. The direct transmitting radiation $I_1(\lambda)$, along with $I_2(\lambda)$, which reflects twice inside the sapphire wafer, generates interference. A sapphire fiber aligns the wafer perpendicularly, on the other side. It guides the interference signal to the spectrometer.

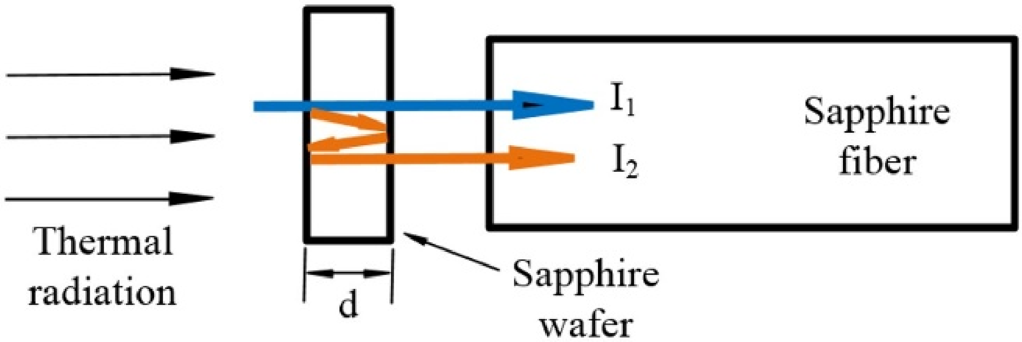

Figure 2-2 Optical design for thermal-radiation-induced interference.

We assume, that the radiation field generated by the sapphire fiber itself, is negligible, based on the fact that single-crystal sapphire is highly transparent in the wavelength range of our interest. Therefore, the interference spectrum may be expressed as [11],

$$I(\lambda) = (I_1(\lambda) + I_2(\lambda)) \cdot (1 + F_v \cos(\frac{2\pi}{\lambda} \cdot OPD + \phi)) \tag{2.5}$$

$I_1(\lambda) + I_2(\lambda)$ indicates the DC background. The cosine term represents the optical interference. The Optical Path Difference (OPD) between the two interfering lights equals to *2nL*. ϕ is defined as the initial phase [12]. OPD is a function of temperature, because both the wafer thickness (*L*) and the refractive index (*n*) are temperature dependent, due to the thermal expansion and the thermal-optic effect. Usually, we describe the OPD vs. T relation by a second-order polynomial function. In practice, one needs to determine the OPD-temperature calibration curve, before using the temperature sensor.

The fringe contrast, denoted as F_v, is commonly used to describe the visibility of the interference fringe from the background signal,

$$F_v = \frac{I(\lambda)_{max} - I(\lambda)_{min}}{I(\lambda)_{max} + I(\lambda)_{min}} \tag{2.6}$$

For an F-P interferometer, a larger F_v is usually more desirable when doing signal demodulation, as a better fringe contrast provides a more accurate optical length calculation. In an ideal case, when $I_1(\lambda)$ and $I_2(\lambda)$ both illuminate the wafer perpendicularly, with 100% transmission and no inter-modal conversion in the lead-in fiber [13], we have,

$$F_v = \frac{2\sqrt{I_1(\lambda) I_2(\lambda)}}{I_1(\lambda) + I_2(\lambda)} \tag{2.7}$$

In the proposed F-P structure, there are two additional reflections inside the sapphire wafer. Therefore, $I_2(\lambda)$ is proportional to $I_1(\lambda)$ and lower by a factor of R^2,

$$I_2(\lambda) = R^2 I_1(\lambda) \tag{2.8}$$

R represents the reflection coefficient at sapphire and air interface. At perpendicular incidence, *R* is deduced as,

$$R = \left(\frac{\mathrm{n}_{sapphire} - 1}{\mathrm{n}_{sapphire} + 1}\right)^2 \tag{2.9}$$

In our case, while acquiring optical spectrum at ~850nm, $\mathrm{n}_{sapphire} = 1.7589$ [14]. Given that $I_2(\lambda) = I_1(\lambda)R^2$, F_v is calculated to be 0.14.

2.2.3 Thermal Radiation of Sapphire Fiber

As discussed in the last section, Equation (2.5) is valid only when the thermal radiation generated by the sapphire fiber itself is negligible, compared to the power collected from outside of the sapphire fiber. For near-infrared wavelength at ~850nm, the sapphire fiber is almost transparent, given by the transmission properties of sapphire. A commercial sapphire fiber holds a transmission loss of less that 3dB/m at 850nm. According to Kirchhoff's Law of thermal radiation, the sapphire fiber with a weak absorption would exhibit a weak emission as well.

To confirm this assumption, we measured thermal radiation of a sapphire fiber in the experiment. The measurement was done in a 5” lab-made tube furnace, as illustrated in *Figure 2-3*. The heating wires heated the furnace up to ~800°C. A piece of sapphire fiber was inserted into the furnace as the radiation medium. Its one end was finely polished and exposed to the air. The other end is butt-coupled to a multimode fiber. According to the setup, all the light power, no matter collected from the sapphire fiber end surface, or generated by the sapphire fiber itself, will be guided to the spectrometer (Ocean Optics USB 2000). We measured at five positions when pulling out the sapphire fiber from deep inside the furnace. The sapphire fiber tip located at the positions which were 1” separated for each measurement. Points 1 to 5 indicate the sapphire fiber tip position.

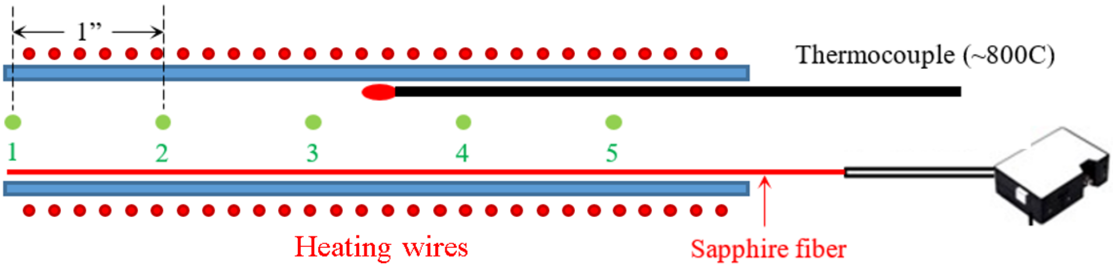

Figure 2-3 Thermal radiation test for a sapphire fiber inside a lab-made tube furnace.

Figure 2-4 (a) shows the power spectra recorded by the spectrometer, from positions 1 to 5. The background curve was collected at room temperature. *Figure 2-4* (b) illustrates the spectra after removing the background. The result shows a gradually increased thermal radiation power from positions 1 to 5. At position 1, all 5” long sapphire fiber was heated. However, its end surface was exposed outside the furnace in the ambient environment. As a comparison, at position 5, although only 1” fiber was heated, the sapphire fiber was able to collect the most of the thermal radiation generated by the furnace. It is clear the radiation collected by the fiber was dominant, and it was approximately two orders of magnitude stronger than the radiation generated by the sapphire fiber itself. Based on this result, we conclude that the thermal radiation of the transparent sapphire fiber is negligible.

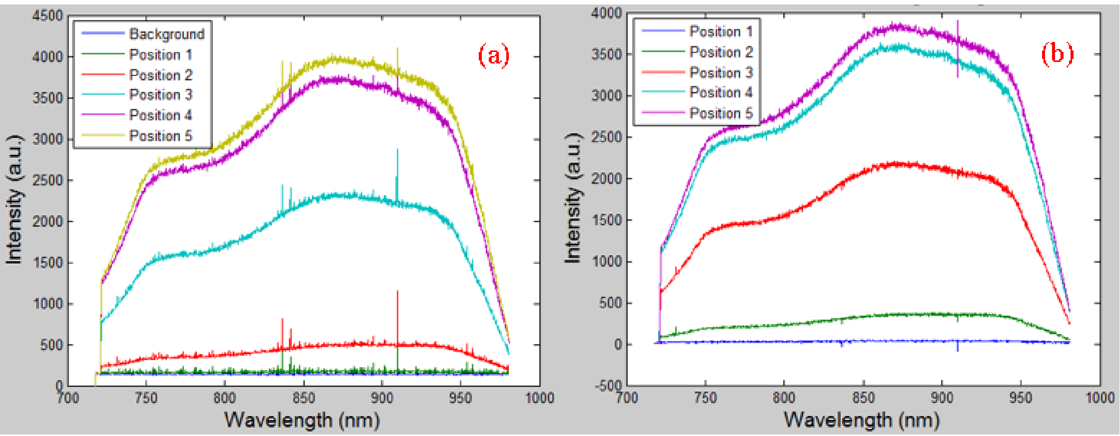

Figure 2-4 Thermal radiation strength investigation of a bare sapphire fiber.

2.2.4 Fringe Contrast of the Sourceless Fabry-Perot Cavity

When putting the sourceless sapphire-wafer Fabry-Perot temperature sensor in actual applications, the thermal radiations from the environment do not ideally illuminate the sapphire wafer F-P perpendicularly, as what is drawn in *Figure 2-2*. In fact, the accepted light is a combination of the thermal radiations within the acceptance angle of the sapphire fiber. The incident rays at deeper angles generate larger OPDs when demodulated from the optical spectrum. At the same time, these rays also excite higher order modes in the sapphire fiber, which experience a stronger attenuation due to stronger fiber surface scattering losses. The multimode excitation and the inter-modal coupling, reduce the interference fringe contrast [12]; which is also one of the origins of the additional phase that causes the signal jump issue. Hence, the calculated wafer OPD is an equivalent value, depending on the angular power distribution of the thermal radiation, and the mode distribution in the sapphire fiber.

Besides the equivalent OPD, the fringe contrast of the interference signal also depends on the angular power distribution of the thermal radiation, which results in an OPD distribution at any fixed wavelength. From Equation (2.5), the maximum interference value is obtained only when $2\pi \cdot OPD / \lambda + \phi = m\pi$ ($m \in integer$). From the above analysis, the OPD distribution does not allow the interferences of differently angled rays to get the maximum value simultaneously. The superposition of all radiation components reduces the local maximum peak, which is the highest value when all incident rays transmit at the same angle. Similarly, we cannot get the theoretical local minimum value as well. The overall effect makes the fringe contrast of a real sensor smaller than what is theoretically calculated for a single incident angle of the thermal radiation.

According to the above analysis, the equivalent wafer OPD and the fringe contrast of the wafer F-P cavity are both dependent on the spatial power distribution of the thermal radiation field. Therefore, the sapphire wafer should not be exposed directly to the environment if the radiation field is unknown or unstable. Instead, it should be contained in a structure that provides a predictable and repeatable radiation field for a given temperature.

2.3 Sourceless Optical Temperature Sensor

2.3.1 Sensor Head Fabrication

Figure 2-5 sketches the cross-section design of the optical sensor head. A sapphire wafer is mounted on the end of a finely polished alumina tube. It functions as the temperature sensing F-P cavity. A sapphire fiber is aligned with the wafer via a through-hole cast inside the tube. A one-end-sealed alumina cap covers the sapphire wafer. While blocking the environmental radiations, the cap also generates a stable thermal radiation field as the illuminator. High purity alumina adhesives mount all the parts together. This all-alumina structure makes the entire sensor head thermally stable and also offers a mechanical protection to the optical elements.

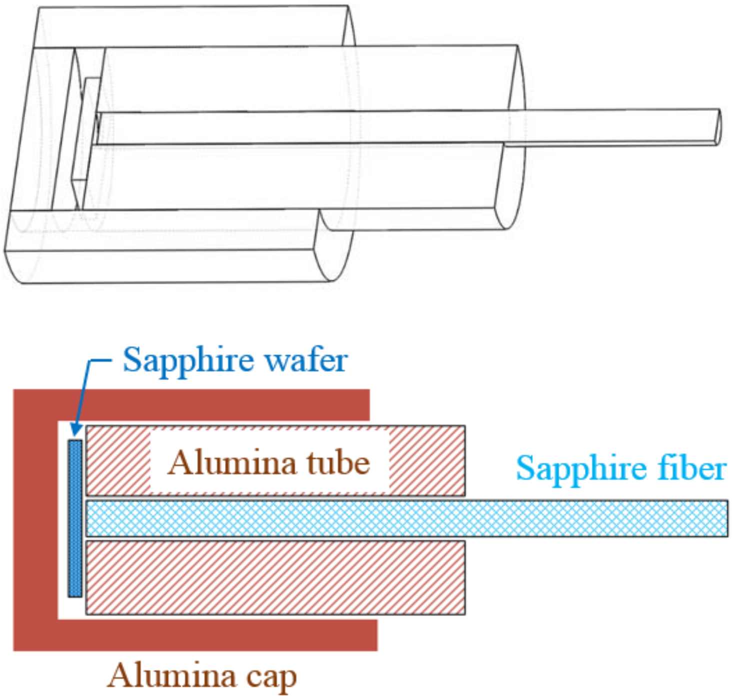

Figure 2-5 Cross-section of the optical sensor head [17].

The actual sensor head was fabricated similarly to [16, 17]. A four-hole (inner diameter: 220μm) alumina tube (outer diameter: 1.2mm, Advanced Ceramics Inc.) was finely polished down to 1μm roughness. The alumina tube stood upside-down with the polished side faced up. A piece of sapphire wafer laid on top of the polished side (*Figure 2-6*) by using vacuum tweezers. Its position was carefully adjusted to cover at least one hole on the tube. A tiny amount of sol-gel was added in between the wafer and the tube for bonding.

The sol-gel contains three components, the Polyureasilazane (Ceraset SN), the Dicumyl Peroxide as the catalyst to speed and control the polymerization time, and the ethanol as the solvent. When this sol-gel style precursor was heated under appropriate conditions, it can generate either silicon nitride, silicon carbide or silica [18]. Heating the sol-gel to generate silica is expected since silica reacts with sapphire at high temperature to form mullite. The mullite layer in between the sapphire wafer and the alumina tube permanently mount them together.

The sol-gel was treated according to the following procedure to achieve a high strength bonding between the wafer and tube. A heating lamp dried the sol-gel at first. Then, the sol-gel was heated to 120°C, 250°C, and 600°C for 2 hours, 2 hours, and 4 hours, respectively. The heating rate was set at 3°C/min.

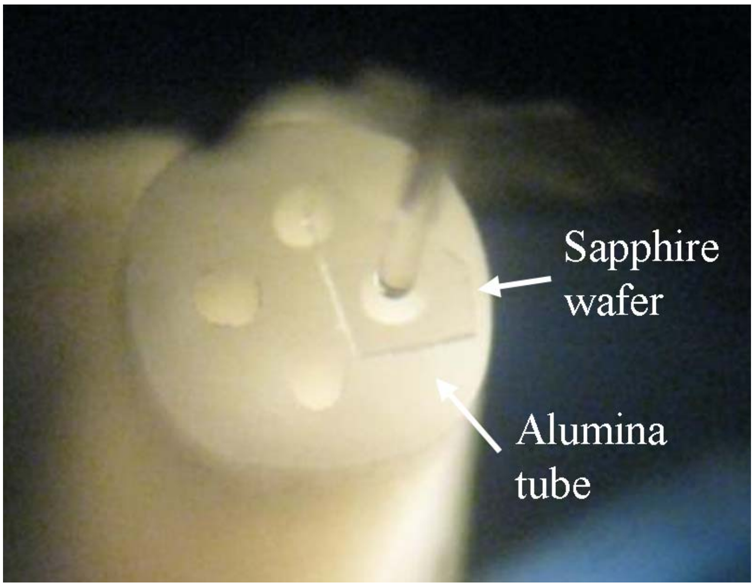

Figure 2-6 Sapphire wafer placed on the alumina tube with four holes.

After bonding the sapphire wafer on the tube, the one-end-sealed alumina cap covered the sapphire wafer. The cap has an outer diameter of 1.6 mm. *Figure 2-7* shows the microscopic image of an assembled sensor head. A fine polished sapphire fiber was inserted into the hole with sapphire wafer covering. A small amount of high purity (>99%, HP903, Cotronics Inc.) alumina adhesive was applied to hold all components in position.

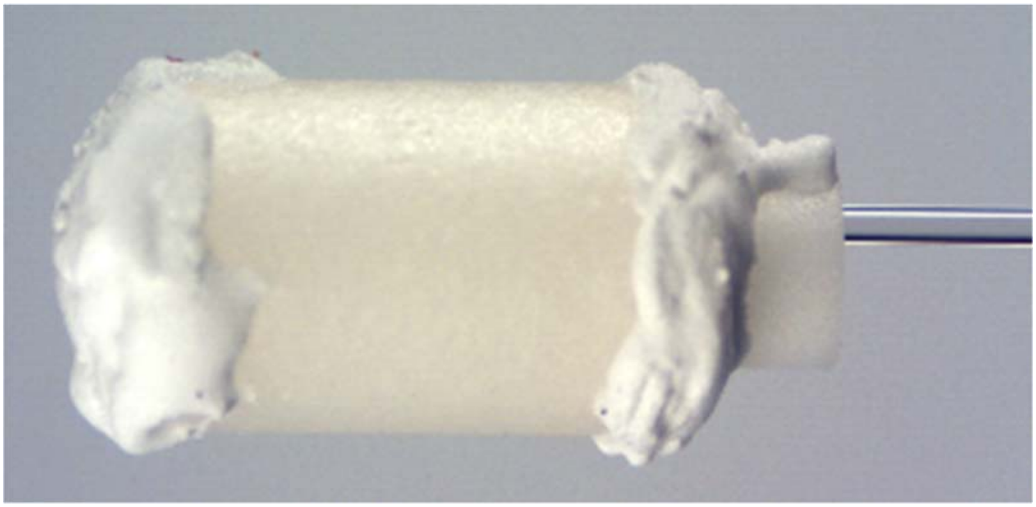

Figure 2-7 Assembled sensor head with the sapphire fiber alignment.

Careful material selection is essential for sensor head fabrication. Usually, silica fiber (pure or doped) and sapphire fiber are two types of fibers commercially available for sensing applications. Silica fiber faces several issues in high temperature greater than 1000°C, such as the surface devitrification [19], the dopant diffusion [20], the internal stress release [21], and the refractive index change [22]. Single crystal sapphire fiber is almost the only choice within the commonly used fibers. For temperature measurement higher than 1200°C, the thermal expansion mismatch is important if the sensor head has several components. The thermal expansion would introduce significant thermal stresses. They would bend the thin sapphire wafer, or the fiber inside the alumina tube.

Hence, we propose an all-alumina sensor head to minimize the thermal stresses. The meterial is alumina for all components, such as the sapphire wafer and fiber (single crystal alumina), and the high purity polycrystalline alumina tube and adhesive.

2.3.2 Optical System

Figure 2-8 shows the schematic of a traditional optical sensing system. It includes a broadband LED (60nm linewidth, center at 850nm) and its driver. The broadband light propagates through an optical coupler and launches to the sapphire wafer F-P sensing cavity. The interference signal reflected from the sensor head propagates through the optical coupler again and is finally collected by a spectrometer.

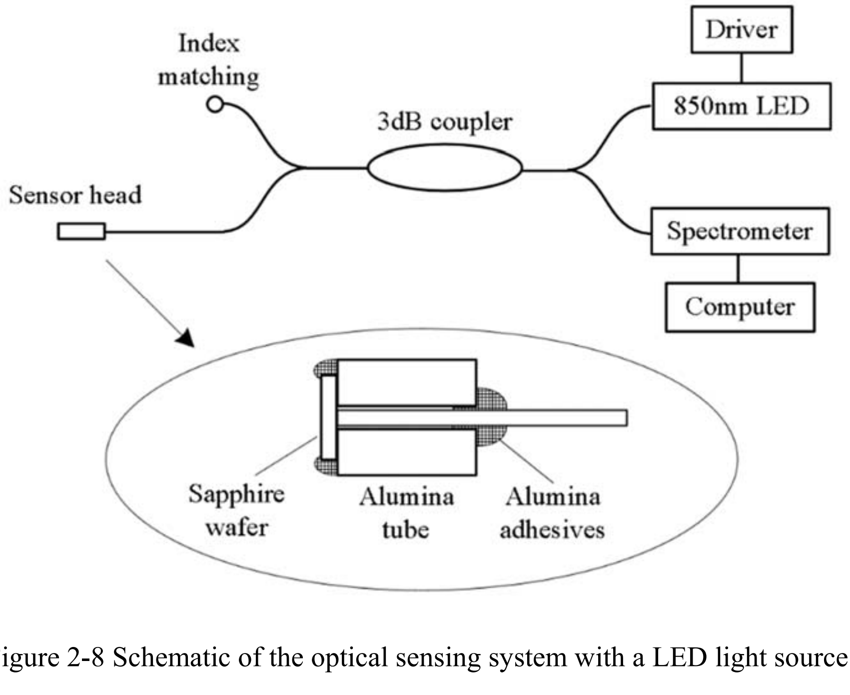

Figure 2-8 Schematic of the optical sensing system with a LED light source.

With the thermal radiation light source, the optical system becomes much simplified, as shown in *Figure 2-9*. The sapphire fiber collects thermal radiation from the sensor head and guides it to a multimode silica fiber via a butt coupling. A spectrometer (Ocean Optics USB2000) records the interference spectrum. A computer is used to conduct the signal processing in real time. The system avoids using an external light source and its driver, as well as the optical coupler. The simpler structure reduces the labor work significantly.

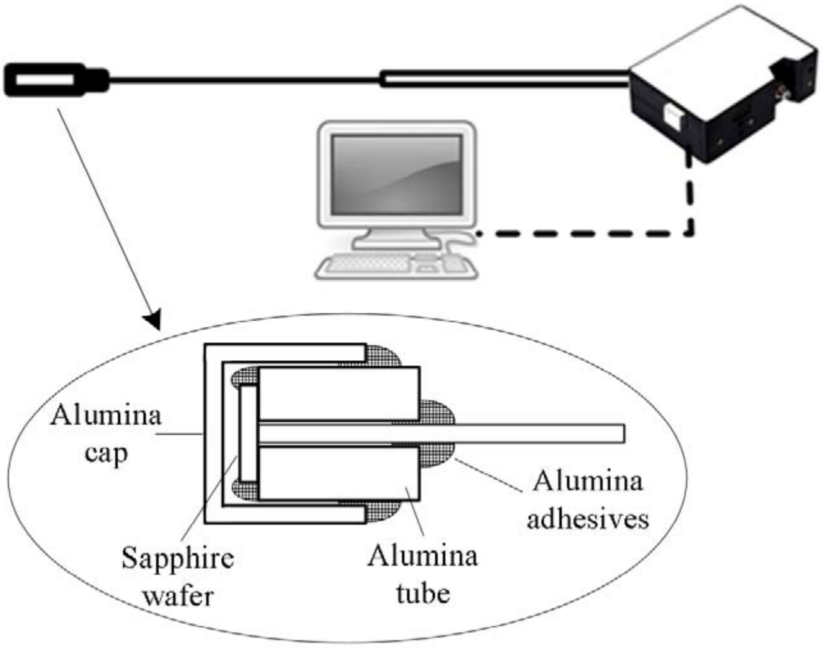

Figure 2-9 Schematic of the sourceless optical system [17].

2.4 Result and Discussion

2.4.1 High-Temperature Sensor Test System

The actual temperature sensor is investigated in a tube furnace, shown in *Figure 2-10*. A type B thermocouple colocates with the optical sensor head for temperature reference. The thermal radiation-induced interference signal is guided to the Ocean

Optics spectrometer. The thermocouple and the spectrometer acquire data simultaneously for temperature calibration.

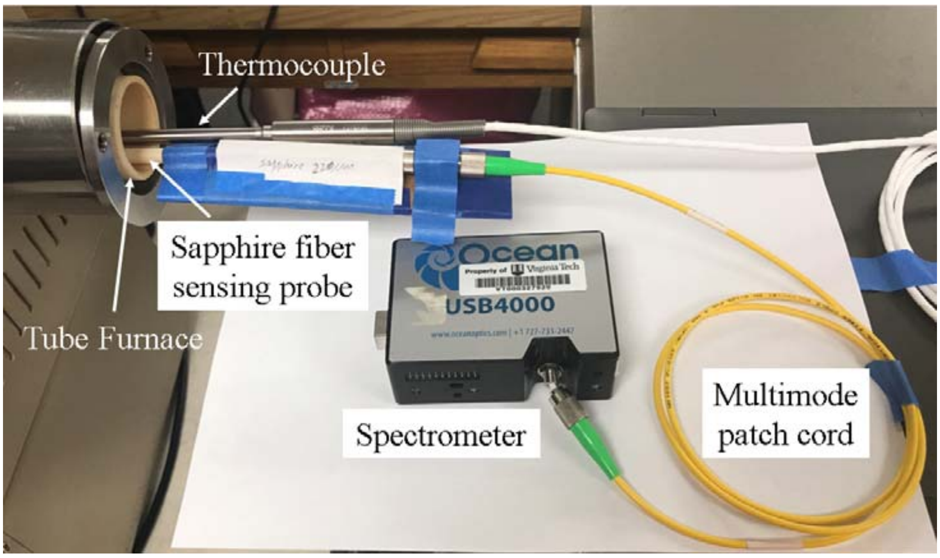

Figure 2-10 High-temperature optical sensor investigation system in the lab.

2.4.2 Description of the Interference Signal

Figure 2-11 illustrates a typical optical spectrum obtained at 1593°C, from the sourceless optical system (Figure 2-11). A clear interference fringe pattern appears on the background signal. It is the result of the thermal-radiation-induced interference. However, the actual optical background is different from the shape of the ideal thermal radiation, simulated in *Figure 2-1*. For an ideal blackbody, the radiational at 1500C° has a peak at ~1.6 µm. For the wavelength shorter than 1.6 µm, the radiation power decreases with the wavelength. In our case, the spectrometer exhibits two shallow peaks at 725nm and 830nm, which is different from the ideal blackbody radiation. In this section, we discuss several factors that will affect the actual optical spectrum.

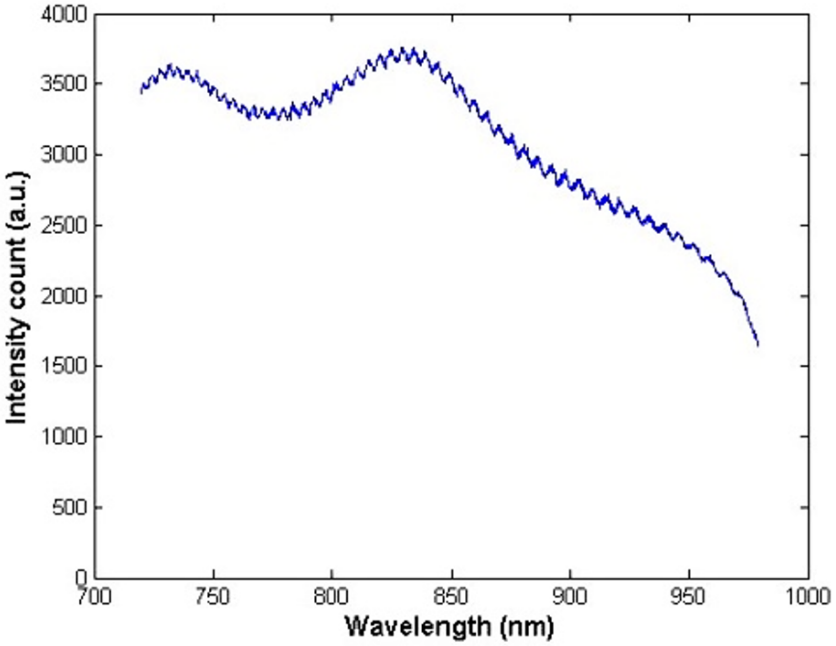

Figure 2-11 The thermal-radiation-induced interference spectrum at 1593ºC [17].

The actual optical signal indicated by a spectrometer is described, theoretically, by the following equation,

$$I(\lambda) = [I_B(\lambda) + I_N(\lambda)] \cdot [1 + I_F(\lambda)] \tag{2.10}$$

Equation (2.10) is modified from Equation (2.5). $I_B(\lambda)$ represents the optical signal collected from the sensor head only; while $I_N(\lambda)$ indicates the noise signal. Here, the wafer interference signal $I_F(\lambda)$ is expressed as,

$$I_F(\lambda) = F_v \cdot \cos(2\pi \cdot OPD / \lambda + \phi) \tag{2.11}$$

The sensor head signal $I_B(\lambda)$ can be further described by,

$$I_B(\lambda) = B(\lambda, T) A(\lambda) R(\lambda) \tag{2.12}$$

$B(\lambda,T)$ indicates the thermal radiation of the alumina cap, being collected by the sapphire fiber. We roughly assume that $B(\lambda,T)$ is the same as the alumina emission. In fact, $B(\lambda,T)$, after traveling through the optical fiber system and being recorded by the spectrometer, will be modified by fiber attenuation $A(\lambda)$ and the responsivity $R(\lambda)$ of the spectrometer. $A(\lambda)$ relates to the contamination absorptions and the surface scattering of a sapphire fiber. $A(\lambda)$ may keep increasing when contaminants accumulate on the cladding-less sapphire fiber over time. Physical degradation on the sapphire fiber surface also enlarges $A(\lambda)$. Compared to $A(\lambda)$, the responsivity $R(\lambda)$ of a commercial spectrometer is usually stable, although it varies for different image sensors.

$I_N(\lambda)$ in Equation (2.10) describes the background noise. Like $I_B(\lambda)$, $I_N(\lambda)$ is also part of the background. $I_N(\lambda)$ includes the thermal radiation generated by the sapphire and silica fiber, and the spectrometer noise. It is, largely, determined by the optical exposure time, or integration time. In our case, while increasing the optical exposure at a lower temperature, $I_N(\lambda)$ becomes stronger. Given these understandings, the overall background signal $I_B(\lambda)+I_N(\lambda)$ is temperature and exposure-time dependent. Therefore, the indicated background is a modification of the ideal alumina radiation spectrum ($B(\lambda,T)$). It appears that the background signal varies slowly with wavelength.

Showing in *Figure 2-11*, the data processing aims at extracting the sapphire wafer interference $I_F(\lambda)$ from the background signal. A clear interference pattern is observed. The fringe contrast F_v, calculated to be 0.016, is smaller than the ideal theoretical value of 0.14, calculated by Equation (2.7). The F_v reduction is a result of $I_N(\lambda)$, which is not included in the theoretical model, the fringe cancellation between rays at different incident angles, and the intermodal conversion effect [23].

2.4.3 Signal Demodulation

The data processing aims at extracting the wafer interference from the background.

$$I(\lambda) = [I_B(\lambda) + I_N(\lambda)] \cdot [1 + F_v \cos(\frac{2\pi}{\lambda} \cdot OPD + \phi)] \tag{2.13}$$

Expressed by Equation (2.13), the cosine term describes the periodic interference signal in the frequency domain. Although the fringe contrast F_v is low, the periodic signal is still able to demodulate by the white light interferometry (WLI) algorithm, described in [12]. The Fast Fourier Transform (FFT) spectrum to *Figure 2-11* curve shows a clear peak, illustrated in *Figure 2-12*. The peak corresponds to the equivalent OPD of the sapphire wafer, defined as $2n(\lambda, T)L(T)$. As expected, the background signal exhibits a strong low-frequency component in the FFT. However, the optical interference still shows a signal peak approximately 7 dB in the FFT spectrum, marked by the red arrow in *Figure 2-12*, which is strong enough for signal demodulation.

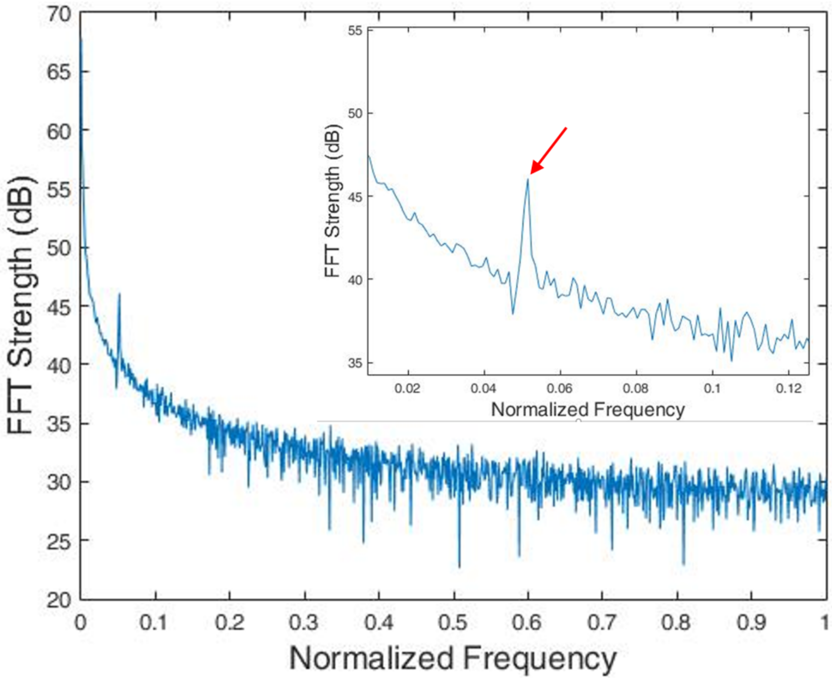

Figure 2-12 Fast Fourier Transform (FFT) to the optical interferometric spectrum at high temperature. The 7dB signal is achieved, pointed by the red arrow [17].

A bandpass FIR filtering can extract the periodic signal from the FFT spectrum [12], illustrated in *Figure 2-13*. The *OPD* in the cosine term $F_v \cos(\frac{2\pi}{\lambda} \cdot OPD + \phi)$ is called the type I OPD [24], symbolled as OPD_I. Recent research has shown that the additional phase ϕ is not constant [12]. It is a function of the angular power distribution, and the OPD itself [23]. To facilitate the signal demodulation, a type II OPD (OPD_{II}), also called the total phase OPD, is introduced [11],

$$\frac{2\pi}{\lambda} \cdot OPD_{II} = \frac{2\pi}{\lambda} \cdot OPD_I + \phi \tag{2.14}$$

In the actual application, one can simply generate an accurate relationship between the sensing parameter and the type II OPD via a standard calibration. The sensor will then work according to the calibration curve.

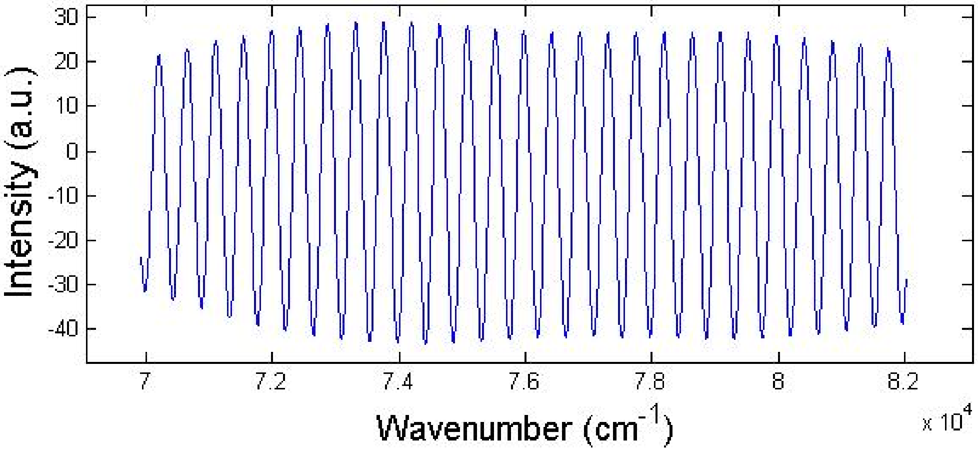

Figure 2-13 Interferometric spectrum after the bandpass FIR filtering [17].

Since the variable in the cosine term is $\frac{1}{\lambda}$, the optical signal, shown in *Figure 2-11*, needs to be converted to the wavenumber domain, and then equalize the spacings via an interpolation. Therefore, *Figure 2-13* shows the signal with a constant periodicity in the wavenumber domain. Given the above signal, we can use the established type II method [11] for OPD demodulation.

2.4.4 Temperature Sensor Investigation

The sourceless sapphire wafer temperature sensor was examined in a thermal test up to ~1600°C [17]. The optical spectra and temperatures were recorded simultaneously and continuously during the entire process. The light exposure was adjusted according to the radiation power. At 1593°C, integrations as short as 8ms almost saturated the spectrometer. At 600°C, on the other hand, we set the integration time to 10s. 3650 data points were collected in the heating-up process. We used the white-light-interferometry algorithm to calculate the OPDs of the sapphire wafer F-P. Equation (2.15) expresses the fitted calibration curve with a second-order polynomial function, illustrated in *Figure 2-14*. The measured points match the calibration curve very well. At 1593°C, the temperature responsivity is calculated to be 0.319 °C/nm.

$$OPD = 3.49030\times10^{-13}T^2 + 2.015565\times10^{-9}T + 1.398866690\times10^{-4} \tag{2.15}$$

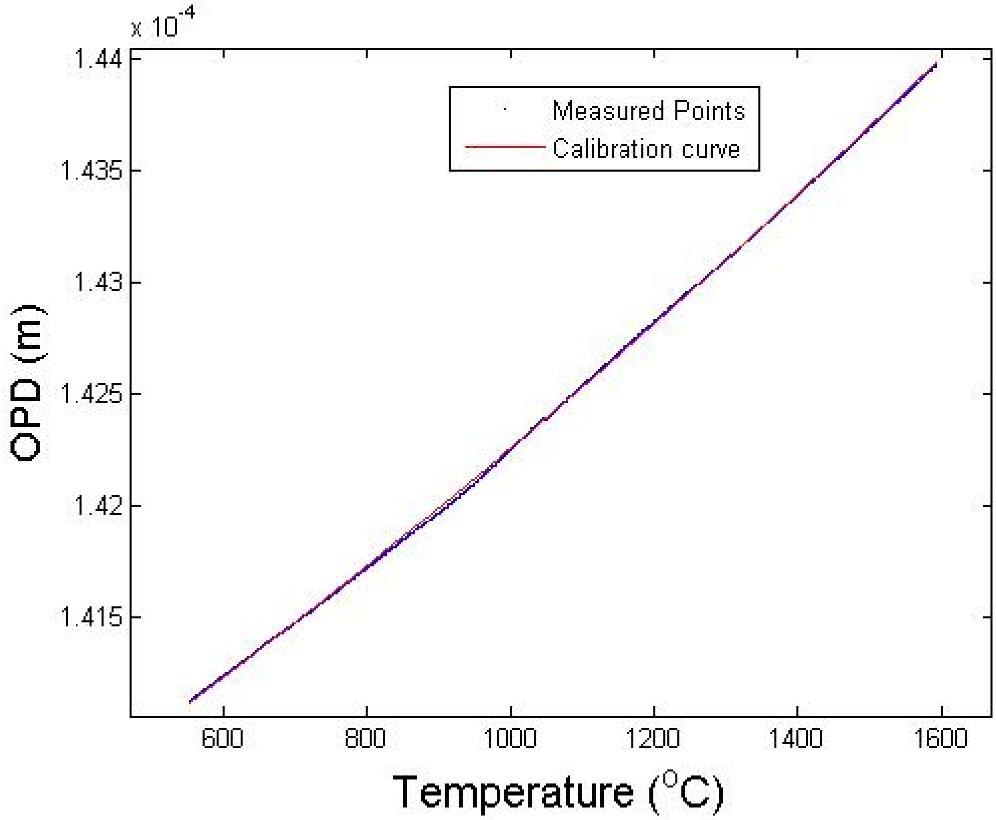

Figure 2-14 OPD-temperature calibration curve of the sourceless temperature sensor [17].

Once the OPD-temperature calibration curve is obtained, the wafer F-P temperature sensor calculates the temperature in practice by the following equation,

$$\begin{aligned}\frac{OPD(T)}{OPD(T_0)} &= \frac{2n(T)d(T)}{2n_0d_0} \\ &= \frac{2n_0[1+\alpha_n(T-T_0)]d_0[1+\alpha_d(T-T_0)]}{2n_0d_0} \\ &= 1+(\alpha_n+\alpha_d)(T-T_0)+\alpha_n\alpha_d(T-T_0)^2 \\ &\sim 1+(\alpha_n+\alpha_d)(T-T_0)\end{aligned} \tag{2.16}$$

Equation (2.16) is further deduced as,

$$T = \frac{1}{\alpha_n+\alpha_d}\cdot\frac{OPD(T)-OPD(T_0)}{OPD(T_0)}+T_0 \tag{2.17}$$

We usually simplify the above equation as,

$$T = f\left[\frac{OPD(T) - OPD_0(T_0)}{OPD_0(T_0)}\right] + T_0 \tag{2.18}$$

In the above equations, n_0 and d_0 are refractive index and the thickness of the Fabry-Perot cavity, respective. α_n and α_d indicate the coefficient of thermo-optic effect and the thermal expansion. $OPD_0(T_0)$ represents the initial optical path length at temperature T_0. $OPD_0(T_0)$ and T_0 have to be obtained and saved as the reference for further calculation. Usually, room temperature is chosen as the reference. Equation (2.18) sets a simple relationship between the indicated temperature T and the calculated $OPD(T)$, given the initial status.

2.4.5 Characterization of Temperature Performance

To characterize the temperature perfornace of the sensor, the sensor head was heated together with a type-B thermocouple, at several set temperature levels, started at 1400°C, and then cooled to 600°C at 100°C intervals. During the test, 100 optical spectra and thermocouple readings were recorded simultaneously, at each set temperature level. The sampling interval was set to 10 seconds.

Figure 2-15 shows the thermocouple readings at each temperature step. The mean temperatures and the standard deviations (σT) were calculated and noted on the figure.

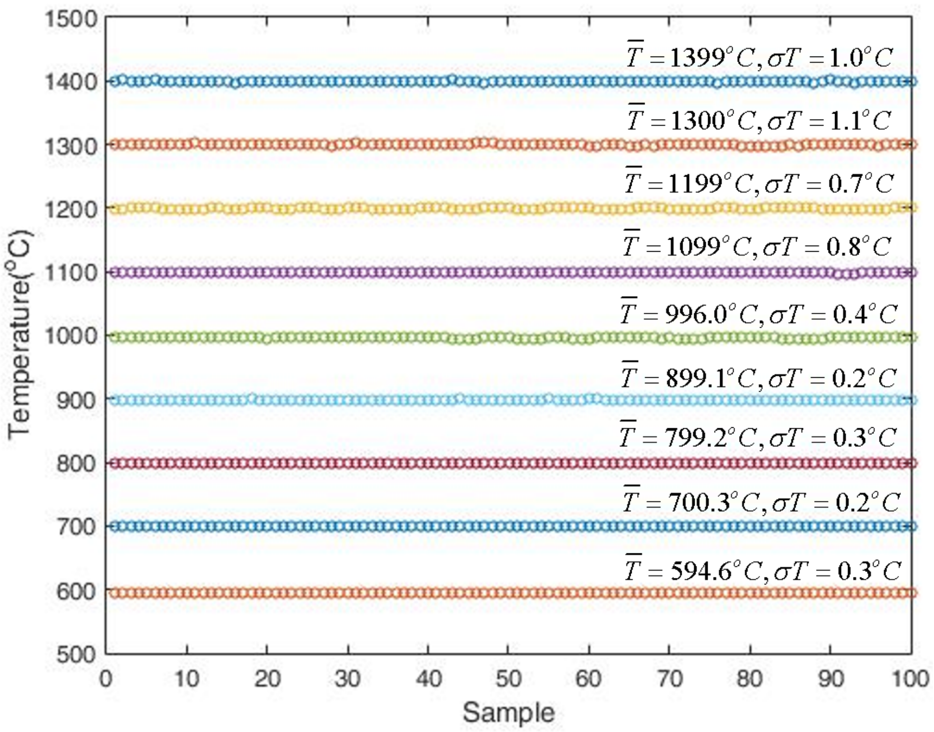

Figure 2-15 Temperatures recorded by the type B thermocouple during the thermal test. The mean temperature values and the temperature standard deviations of each temperature step are calculated and noted on the figure.

It was noticed that the commercial thermocouple controller (Dpi32-C24, Omega Inc.) displays only four digits, which gives an observable difference in temperature indications between lower than 999.9°C and higher than 1000°C. This change can be observed clearly in Figure 2-16. Figure 2-16 (a) shows the thermocouple readings above 1000°C. The output values have discrete increments of integer numbers, such as 1°C, 2°C and 3°C. As a comparison, the controller gives a better temperature reading at below 1000°C, which is able to display at 0.1°C scale. This directly affect the temperature standard deviation. The thermocouple readings shows observable larger temperature standard deviations.

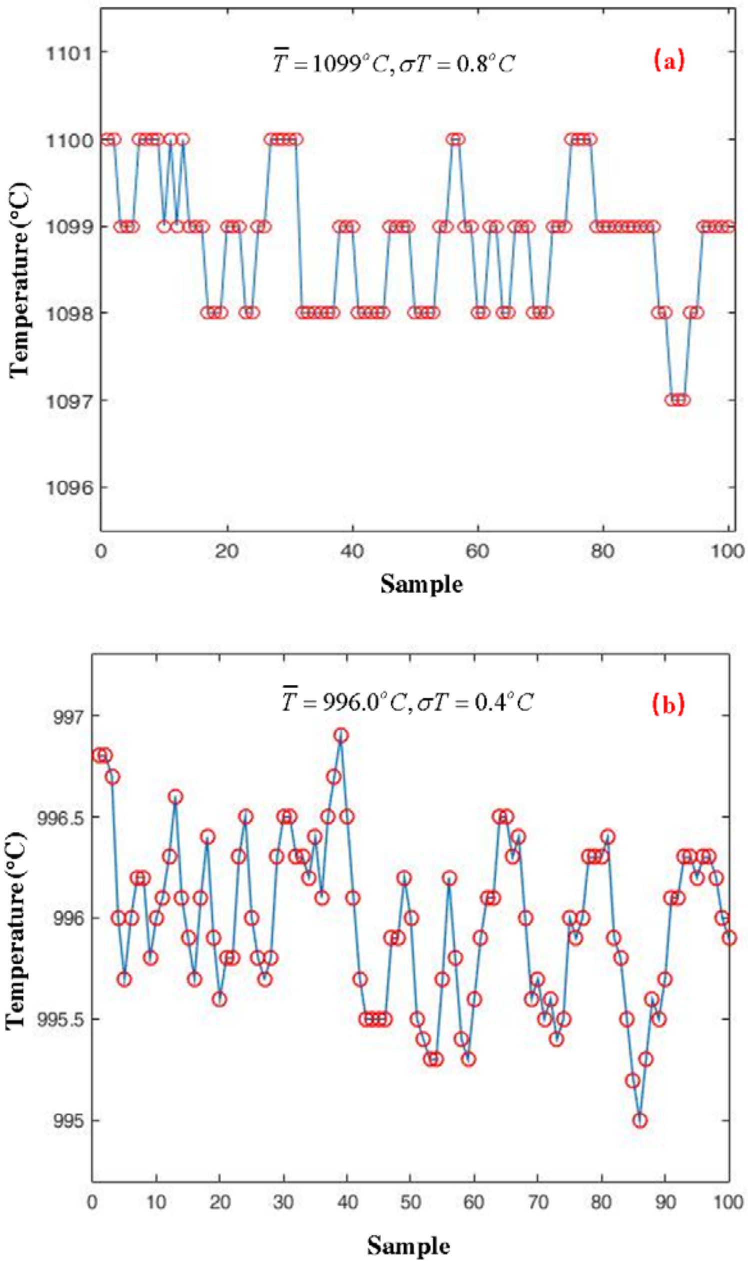

Figure 2-16 Comparison between the thermocouple readings at temperatures above 1000ºC (a) and below 1000ºC (b).

The OPDs were calculated using the white light interferometry algorithm. The calculation result is illustrated in *Figure 2-17*. The temperature noted in *Figure 2-17* is the average temperature obtained from the measurements.

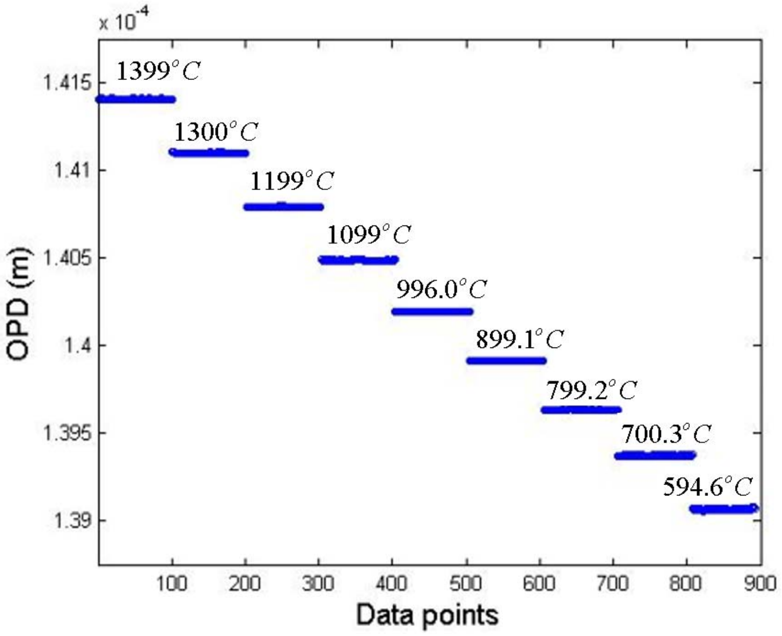

Figure 2-17 OPD calculation at different temperature levels [17].

A detailed OPD values, calculated at each temperature level, are illustrated in *Figure 2-18*.

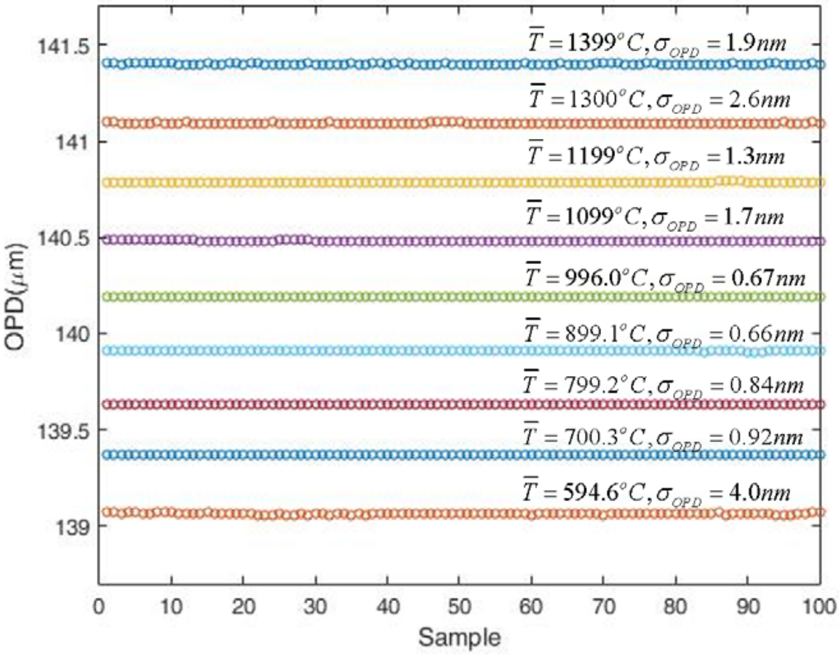

Figure 2-18 OPD calculations based on WLI at each temperature step. The standard deviations are calculated and noted on the fiber.

The standard deviation of the wafer OPD (σ_{OPD}) was calculated according to the data listed in *Figure 2-17*. From the OPD-temperature calibration curve, the temperature responsivity with respect to the OPD change has been obtained, which is the slope of the calibration curve. Therefore, we get two sets of temperature standard deviations at each given temperature level. One of them is direct calculation from the thermal couple readings, noted as $\sigma_{T\text{-TC}}$. The other one, noted as $\sigma_{T\text{-}WLI}$, was obtained from the OPD-temperature calibration curve,

$$\begin{aligned} \sigma OPD &= \frac{dOPD}{dT} \cdot \sigma T \\ \Rightarrow \sigma T &= \frac{1}{\dfrac{\partial OPD}{\partial T}} \cdot \sigma OPD \end{aligned} \tag{2.19}$$

Figure 2-19 compares the two sets of the temperature standard deviations $\sigma_{T\text{-TC}}$ and $\sigma_{T\text{-}WLI}$, respectively. Generally, the control of thermal environment in the furnace is more stable at lower temperatures, indicated by both values. Limited by the display digits, $\sigma_{T\text{-TC}}$ which was directly calculated by the thermocouple readings, is larger than $\sigma_{T\text{-}WLI}$, at temperatures higher than 1000ºC. When temperature drops below 1000 ºC, with a stable heating control and a better display, $\sigma_{T\text{-TC}}$ and $\sigma_{T\text{-}WLI}$ show close values. As temperature continuously cools down, the thermal radiation intensity reduces dramatically, which causes a poor signal to noise ratio in the sourceless sensor spectra; and results in a poorer thermal performance for the sourceless fiber optic temperature sensor. We get the smallest temperature standard deviation in experiment result at 900~1000ºC when thermal control in the furnace is relatively stable, while at the same time, the thermal radiation is still strong. 0.2ºC temperature standard deviation was achieved. As a high temperature sensor, its high temperature performance is more desirable. If ±2σ is defined as the temperature resolution, we may expect that the sourceless optical sensor will have a temperature resolution of no worse than ±0.4ºC at temperatures higher than 1000ºC for the reason that higher temperature provides stronger thermal radiation, which is the origin of the optical interference. In this case, we can use less light exposure time to the spectrometer CCD, which reduces the CCD noise. Furthermore, with a given data acquisition interval, shorter exposure time allows doing more sampling and averaging, which further enhances the sensor performance.

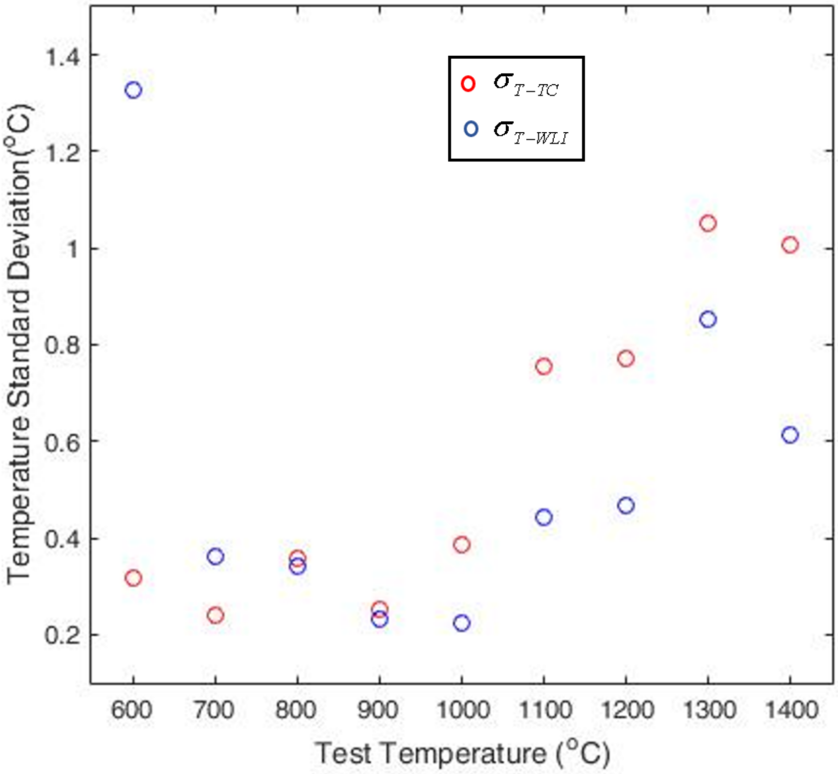

Figure 2-19 Comparison of temperature standard deviations at different temperature levels.

It is noticed that the light exposure time is important for sampling. Since the light intensity of the thermal radiation increases with the temperature, an automatic algorithm was developed to adjust the exposure time of the spectrometer according to the radiation power to make full use of the intensity measurement range of the spectrometer. *Figure 2-20* shows the light exposure time vs. temperature curve. 10 seconds is the longest light exposure time set in the experiment.

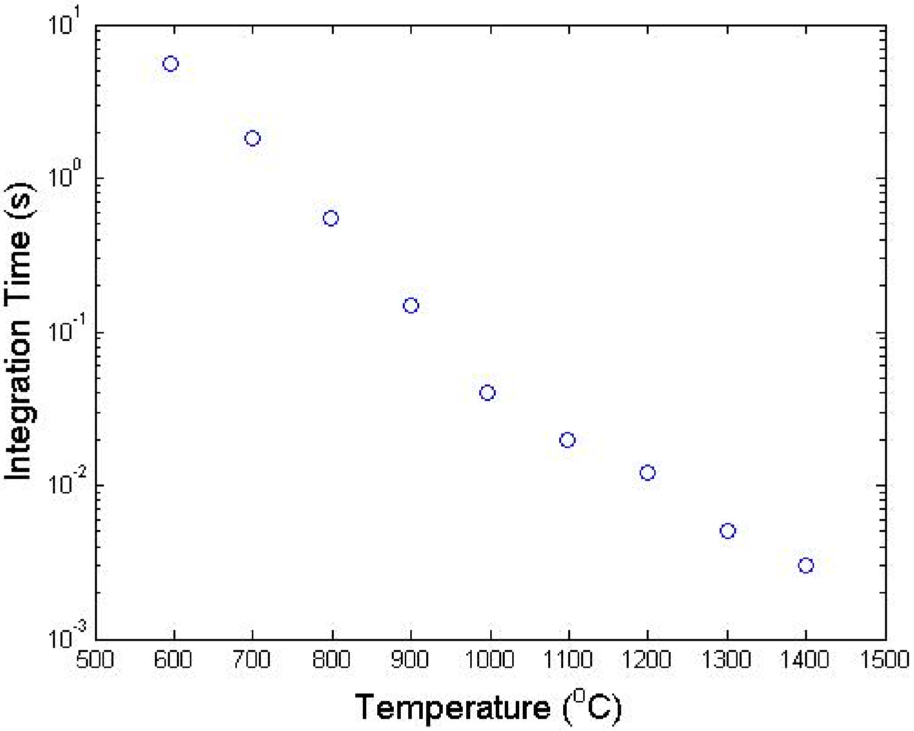

Figure 2-20 Spectrometer integration time increases as the temperature cools down.

2.4.6 Signal Demodulation Jump

Due to the nature of the thermal radiation, the sensor performance will decline at a lower temperature. According to Stefan-Boltzmann law, the radiation intensity from a blackbody is proportional to the fourth power of its temperature. Therefore, the radiation power reduces rapidly when a blackbody cools down. In our case, the lower sensing limit is defined at the temperature when the signal becomes so low that signal demodulation jumps [25] begin to occur. Shown in *Figure 2-21* (a), while using a 75 µm diameter sapphire fiber and an Ocean Optics USB2000 spectrometer, with 10s integration time, the OPD demodulation starts to exhibit a jump at 554°C. While the sensor head continues to cool down, more jumps happened.

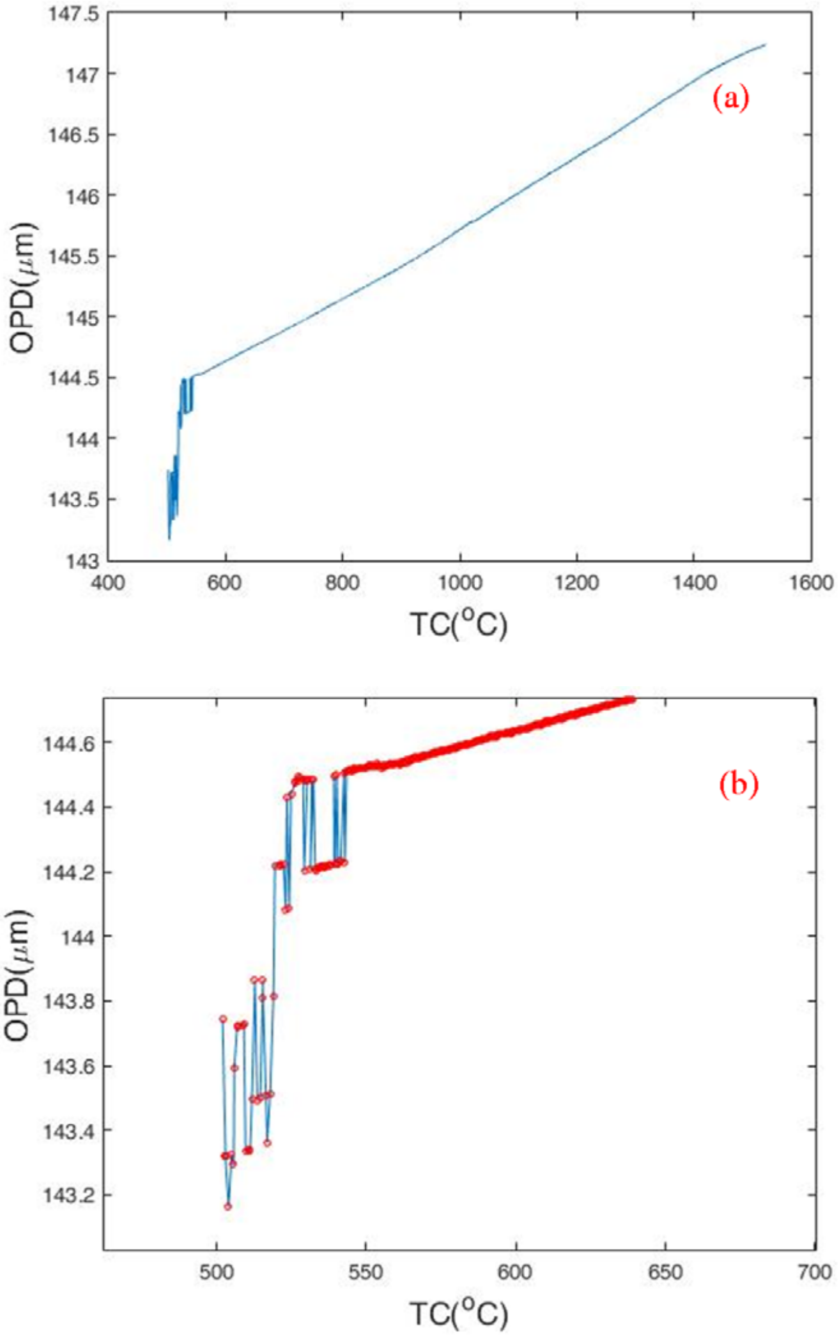

Figure 2-21 A demonstration of the OPD demodulation jump when the sapphire-wafer sensor head cooled from 1500ºC (a); The enlarged figure shows the signal jump region (b).

2.5 Challenges and the Future Work

Enhance the radiation power is key to a radiation-based sourceless sensor to improve the performance and extend its sensing limits. Several approaches can potentially work as solutions, such as using a larger-diameter sapphire fiber, extending the light exposure time, or working at a longer wavelength.

Using a larger sapphire fiber is a direct solution to increase collection of the radiation power. The traditional fiber-based radiation thermometer uses a sapphire fiber as large as 1mm [26]. The sapphire fiber, in a radiation thermometer, functions only as a light guiding. However, for a sapphire-fiber EFPI sensor, one needs to balance between the benefit of more light and the drawbacks of fringe contrast reduction. The mode volume of a multimode fiber is proportional to the fiber core area [27]. Therefore, when the sapphire fiber radius is doubled, its mode volume will increase by a factor of four. When working with highly diverged LED light, we may assume that all modes are evenly excited. If the mode volume of a sapphire fiber increases significantly, the inter-model conversion issue would potentially reduce the fringe contrast of the interference signal, which might eventually kill the benefit of using a larger fiber, as discussed in [13]. Hence, a smaller diameter sapphire fiber is preferred to get a better interference fringe pattern, when a sapphire wafer F-P sensor works with an LED. However, for sourceless design, the radiation power generated by the alumina cap which is mounted just above the sapphire wafer Fabry-Perot cavity, illuminates the wafer in its central region. It may distribute more power in lower order modes. Therefore, the fringe contrast reduction issue, when working with an LED, may not necessarily apply to the sourceless Fabry-Perot sensor.

To investigate the feasibility of using a larger diameter sapphire fiber, a preliminary test was done with three different sized sapphire fibers. Their diameters are 75 µm, 125 µm, and 220 µm, respectively. The test system was built like Figure 2-22. The sapphire fiber was aligned to the same optical sensor head. The sensor head did not have any cover. A halogen lamp (Ocean Optics HL-2000) illuminated the sapphire wafer F-P cavity from the other side. The sapphire fibers guided the interference signals to the spectrometer.

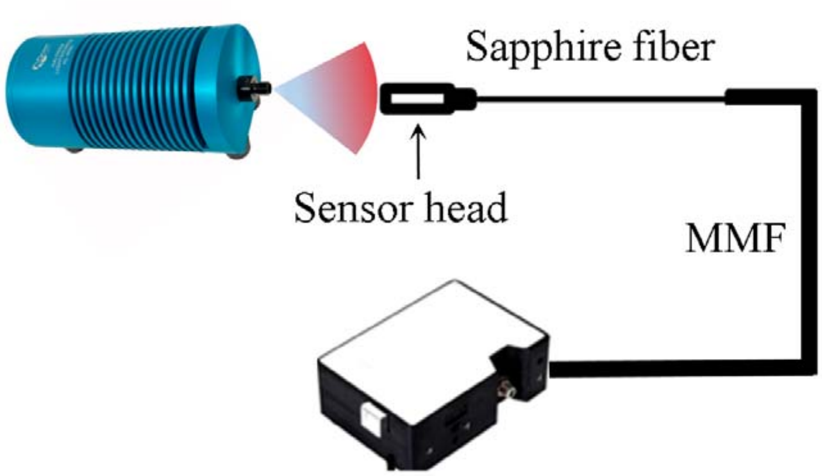

Figure 2-22 Fringe contrast simulation of a transmission Fabry-Perot interferometer.

Figure 2-23 (a) to (c) list the interference signal received by the spectrometer, for three different sized sapphire fibers. The light exposure time is adjusted to bring the intensity similar to each other. Although the overall fringe contrasts are low, it is encouraging to find out that the fringe contrasts of all cases, do not have a significant reduction, when the sapphire fiber diameter increases from 75 μm to 220 μm. This result indicates that it is possible to use a larger sapphire fiber to collect more light, as a possible improvement. It provides a direct solution to extend the temperature sensing range to a lower temperature.

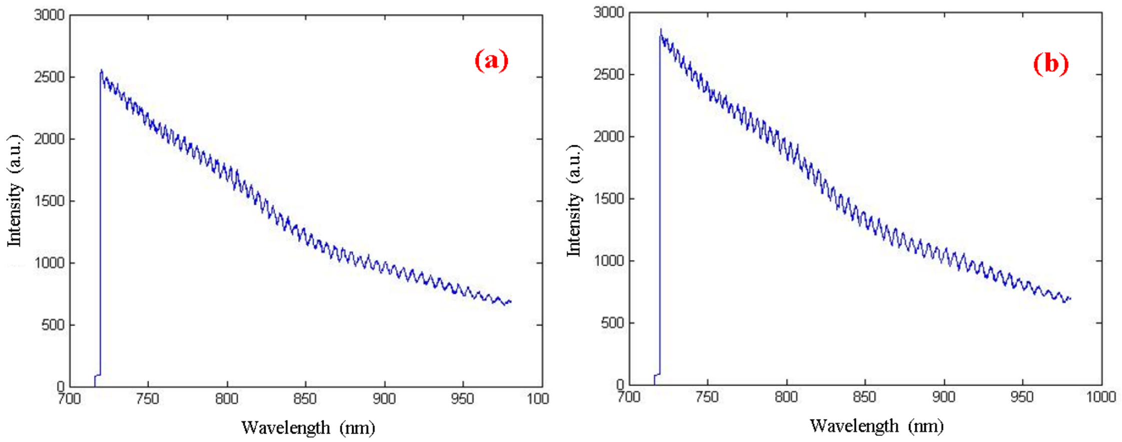

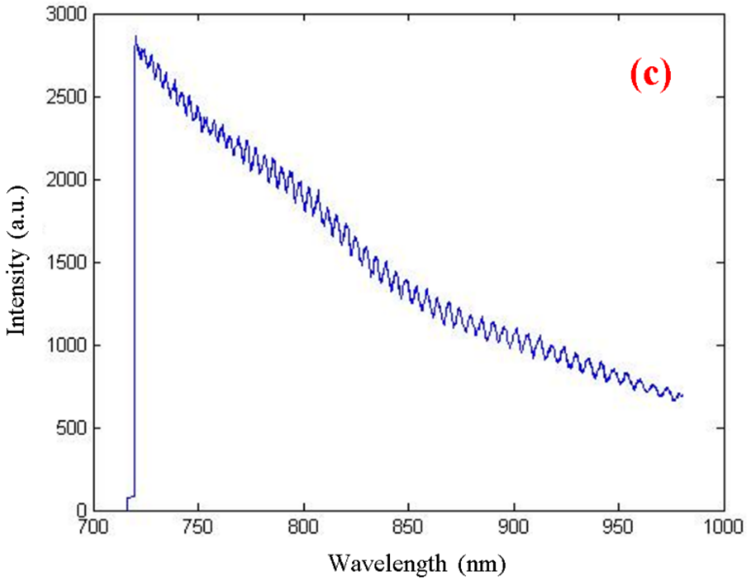

Figure 2-23 Fringe contrast comparison between three different sized sapphire fibers with the same sapphire wafer sensor head. (a) 75µm sapphire fiber; (b) 125µm sapphire fiber; (c) 220µm sapphire fiber.

Collecting radiations at longer wavelength range is another possible, optimizing approach. According to Planck's Law, the radiation power reduces extremely fast when the detected wavelength is further away from the peak wavelength. Moreover, the thermal radiation spectral peak moves to the longer wavelength at a lower temperature. At 1600°C, the peak radiation power of an ideal blackbody locates at ~1.5 µm. This wavelength is approximately 0.65µm away from the central wavelength (850 nm) of our spectrometer. Therefore, it has a good potential to improve the radiation power collection by moving the spectral range to ~1.5 µm, as the sapphire fiber is still transparent. However, this approach might be suffering from a relatively expensive spectrometer. To achieve the low-cost goal, the price of the spectrometer is a key issue. A typical 1-D CCD array for an 850 nm spectrometer cost less than $20.

Extending the light exposure time would improve the signal to noise ratio to some level, but not significantly. Theoretically, the signal to noise ratio would be improved by a fact of $\sqrt{t/t_0}$, where t and t_0 indicate the light exposures, t_0 is the reference. However, it may work that well since the background noise also increases with the integration time, at almost the same rate.

As described in Chapter 2.1, the emissivity is a coefficient that describes the radiation efficiency of an emitter. For a real target, the emissivity is a function of material, surface condition, and wavelength of measurement. *Table 2-1* lists the emissivities of some commonly used oxides. The values are collected from [28]. The emission of the alumina oxide is not very strong, compared to the other oxides. Therefore, making a radiation cap by the a high-temperature oxide, with a strong emission, could enhance the optical power by 2 ~ 3 times, such as niobium dioxide.

Table 2-1 List of emissivity for some commonly used oxides.

Materials	Emissivity
Aluminium oxide	0.26~0.42
Niobium dioxide	0.70~0.73
Cast Iron (oxidized)	0.64~0.78
Magnesium oxide	0.20~0.55
Nichrome oxide	0.95~0.98
Nickel oxide	0.59~0.86

2.6 Conclusion

A sourceless sapphire fiber extrinsic Fabry-Perot Interferometer temperature sensor was developed. The miniaturized sensor head was constructed by all-alumina-based components with excellent thermal stability. With an alumina cap designed for generating a stable thermal radiation field, a smooth calibration curve was obtained in a thermal test up to 1593°C. The sensor exhibited a resolution around or better than 1°C throughout the sensing range. This sensor design shows a good potential for low-cost measurement of ultra-high temperatures.

2.7 Reference

1. S. M. Stewart, and R. B. Johnson, *Blackbody radiation: A history of thermal radiation computational aids and numerical methods* (CRC Press, 2016).
2. W. Wien, "XXX. On the division of energy in the emission-spectrum of a black body," The London, Edinburgh, and Dublin Philosophical Magazine and Journal of Science **43**, 214-220 (1897).
3. J. H. Van Vleck, "The absorption of radiation by multiply periodic orbits, and its relation to the correspondence principle and the Rayleigh-Jeans law. Part II. Calculation of absorption by multiply periodic orbits," Physical Review **24**, 347 (1924).
4. J. R. Howell, M. P. Menguc, and R. Siegel, *Thermal radiation heat transfer* (CRC press, 2010).
5. R. Petela, "Exergy of radiation of a perfect gray body," Zesz Nauk Politechniki Slaskiej **5**, 33-45 (1961).
6. H. McMahon, "Thermal radiation from partially transparent reflecting bodies," JOSA **40**, 376-380 (1950).
7. R. H. Dicke, "Coherence in spontaneous radiation processes," Physical Review **93**, 99 (1954).
8. R. J. Glauber, "Coherent and incoherent states of the radiation field," Physical Review **131**, 2766 (1963).
9. P. Y. Wong, C. K. Hess, and I. N. Miaoulis, "Coherent thermal radiation effects on temperature-dependent emissivity of thin-film structures on optically thick substrates," OPTICE **34**, 1776-1781 (1995).
10. O. Kollyukh, V. Kyslyi, A. Liptuga, V. Morozhenko, V. Pipa, and E. Venger, "Coherent thermal radiation of Fabry-Perot resonator structures," Semiconductor Physics, Quantum Electronics & Optoelectronics **10**, 94-102 (2007).
11. C. Ma, "Modeling and Signal Processing of Low-Finesse Fabry-Perot Interferometric Fiber Optic Sensors," (2012).

12. F. Shen, and A. Wang, "Frequency-estimation-based signal-processing algorithm for white-light optical fiber Fabry?Perot interferometers," Applied Optics **44**, 5206-5214 (2005).

13. M. Han, and A. Wang, "Exact analysis of low-finesse multimode fiber extrinsic Fabry-Perot interferometers," Applied optics **43**, 4659-4666 (2004).

14. M. N. Polyanskiy, "Refractive index database," https://refractiveindex.info.

15. D. C. Harris, *Materials for infrared windows and domes: properties and performance* (SPIE press, 1999).

16. Y. Zhu, Z. Huang, F. Shen, and A. Wang, "Sapphire-fiber-based white-light interferometric sensor for high-temperature measurements," Opt. Lett. **30**, 711-713 (2005).

17. Z. Tian, Z. Yu, B. Liu, and A. Wang, "Sourceless optical fiber high temperature sensor," Opt. Lett. **41**, 195-198 (2016).

18. J. Wan, R.-G. Duan, M. J. Gasch, and A. K. Mukherjee, "Methods of processing Si 3 N 4/SiC nano-nano composites from polymer precursor," Materials Science and Engineering: A **424**, 105-116 (2006).

19. A. Rose, "Devitrification in annealed optical fiber," J. Lightwave Technol. **15**, 808-814 (1997).

20. K. Shiraishi, Y. Aizawa, and S. Kawakami, "Beam expanding fiber using thermal diffusion of the dopant," Lightwave Technology, Journal of **8**, 1151-1161 (1990).

21. J. Stone, "Stress-optic effects, birefringence, and reduction of birefringence by annealing in fiber Fabry-Perot interferometers," J. Lightwave Technol. **6**, 1245-1248 (1988).

22. J. Juergens, G. Adamovsky, R. Bhatt, G. Morscher, and B. Floyd, "Thermal evaluation of fiber Bragg gratings at extreme temperatures," in *43rd AIAA Aerospace Science Meeting and Exhibit, Reno, NV*(2005).

23. M. Han, Y. Zhang, F. Shen, G. R. Pickrell, and A. Wang, "Signal-processing algorithm for white-light optical fiber extrinsicFabry-Perot interferometric sensors," Opt. Lett. **29**, 1736-1738 (2004).

24. C. Ma, and A. Wang, "Signal processing of white-light interferometric low-finesse fiber-optic Fabry–Perot sensors," Applied Optics **52**, 127-138 (2013).

25. C. Ma, E. M. Lally, and A. Wang, "Toward Eliminating Signal Demodulation Jumps in Optical Fiber Intrinsic Fabry?Perot Interferometric Sensors," J. Lightwave Technol. **29**, 1913-1919 (2011).

26. Y. Shen, L. Tong, Y. Wang, and L. Ye, "Sapphire-fiber thermometer ranging from 20 to 1800 C," Applied optics **38**, 1139-1143 (1999).

27. G. Keiser, *Optical fiber communications* (Wiley Online Library, 2003).

28. "Total emissivity of various surfaces," https://www.google.com/url?sa=t&rct=j&q=&esrc=s&source=web&cd=1&ved=0ahUKEwiWi6LZ9fjWAhUH5yYKHZdWA0EQFggoMAA&url=https%3A%2F%2Fwww.researchgate.net%2Ffile.PostFileLoader.html%3Fid%3D5922eb07615e2799d907cb5c%26assetKey%3DAS%253A496811984470017%25401495460615482&usg=AOvVaw1c9KN03HsOF5fE7cPqiWdO.

CHAPTER 3 Low-cost Optical Fabry-Perot Interrogation

3.1 Introduction to the Fabry-Perot Signal Demodulation

Signal demodulation of an optical Fabry-Perot (F-P) interferometer is essential for the optical F-P sensors. While Light Interferometry (WLI) is a commonly used algorithm, which calculates the absolute optical path length of an F-P cavity to sub-nanometer accuracy. WLI includes two major methodologies, the full-spectral WLI and the Scanning white light interferometry (S-WLI). The traditional WLI must record the full-length optical spectrum by a spectrometer. In this desertation, we use WLI to represent the full-spectral WLI.

Usually, A spectrometer is expensive. Take a fiber-coupled spectrometer as an example, a compact 'low-cost' spectrometer (Ocean Optics. Inc.), sells nearly $3000 in the market. Besides, an optical sensor system, such as a fiber optic high-temperature sensor [1] built with the spectrometer, requires more optical components, such as a light source and driver, an optical coupler, etc. Thus, the price of the entire optical temperature sensor is much higher than its commercial competitor, the thermocouple. Reading temperatures of a thermocouple is much cheaper; it costs no more than $400.

A low-cost signal demodulation system is desirable for commercialization of the optical Fabry-Perot sensors. Our effort in this research focuses on developing a novel low-cost interrogator for the Fabry-Perot optical sensors, and establishing a new signal demodulation algorithm.

3.1.1 Theory of the Scanning White Light Interferometry

The scanning white light interferometry is one of the important methods to demodulate the optical path length (OPD) of an F-P interferometer. S-WLI provides large dynamic range [2], high speed [3] and good resolution [4].

A typical S-WLI system includes a sensing F-P interferometer and an OPD-tunable F-P interferometer as the reference. The two F-Ps are connected in series. The OPD tuning range of the reference F-P must be wide enough to cover the entire OPD variation of the sensing F-P cavity. A single photodetector collects the total power of the broadband light source, while the reference interferometer is scanning. An optical intensity fringe pattern is created during the scanning process. The maximum fringe peak occurs when the OPDs of the two interferometers match each other [5-7]. Therefore, the OPD scanning process projects the time-dependent optical signal to the spatial domain. With a carefully calibrated OPD-time curve, one can recover the sensing OPD by simply finding the maximum peak in the scanning. Due to a relatively simple signal demodulation algorithm, as well as high resolution [8] and large dynamic range [9], the S-WLI method is adopted in many sensing applications, as long as the physical parameter can be converted to the optical path change of the sensing cavity.

For S-WLI algorithm, usually, the reference OPD scanners are built by moving reflectors, such as movable mirrors [10, 11]. They are driven by a mechanical or a piezoelectric stage. The moving stages are usually very expensive if one needs to achieve a precise displacement scanning in a sub-nanometer scale. While a moveable component is required, the entire system faces issues of mechanical stability and reliable repeatability in the long term.

The examples of an OPD scanner being constructed by a fixed optical component are rare. Wang et al. [12] put a birefringent wedge before a CCD array. The parallel beams, which transmit through the wedge, experience different OPDs. A Fizeau interferometer is also being used, similarly, as the OPD scanner [13]. Even in the above designs, high-quality optical components are needed, such as a wedge-style optical element, which limits the potential of building a low-cost system.

3.1.2 Optical Behavior of a Scanning White Light Interferometer

When an S-WLI optical system is built similar to Figure *3-1*, its behavior can be described by Equation (3.1) [14] In which, OPD_1 represents the target optical path length to be determined, while OPD_2 indicates the reference Fabry-Perot cavity. $I(\lambda)$ is a broadband light source, ranges from wavelength λ_1 to λ_2. λ_1 and λ_2 appear in Equation

(3.1) as the integration limit. F_1 and F_2 indicate the fringe contrast of the two Fabry-Perot cavies, respectively [14].

$$I=\int_{\lambda_1}^{\lambda_1}\frac{1}{2}I(\lambda)F_1F_2\cos[\frac{2\pi}{\lambda}\cdot(\mathrm{OPD}_1-\mathrm{OPD}_2)]\mathrm{d}\lambda \tag{3.1}$$

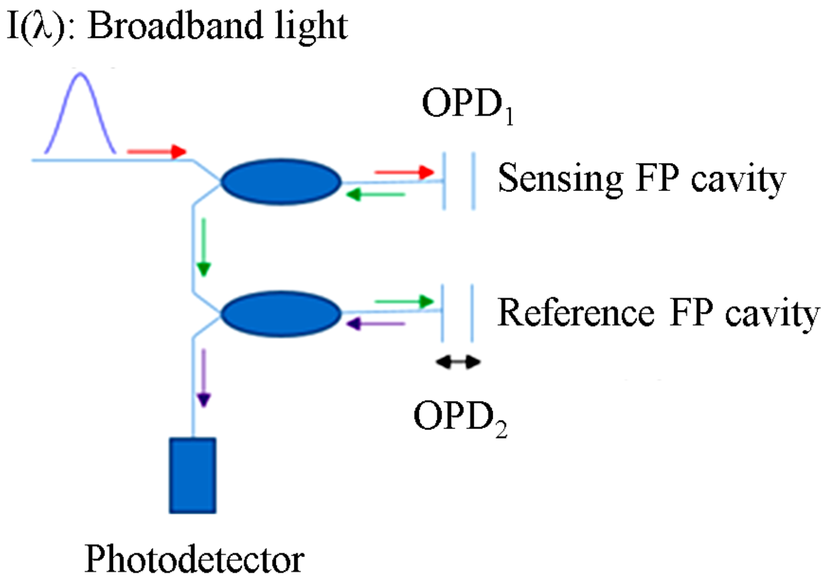

Figure 3-1 General optical system for an S-WLI interferometry.

Figure *3-2* shows the S-WLI behavior, simulated based on Equation (3.1). We used an LED as the broadband source. The optical length of the sensing F-P cavity (OPD_1) is set to 140 μm, similar to the OPD of the sapphire fiber EFPI sensor being discussed in this dissertation. The reference F-P (OPD_2) scans from 125μm to 155μm. We use a Gaussian-shaped function ($f(\lambda)$) to describe the LED spectrum [15],

$$f(\lambda)=\frac{1}{(2\pi)^{1/2}\Delta\lambda/(8ln2)^{1/2}}e^{-(\lambda-\lambda_0)^2/(\Delta\lambda^2/4ln2)} \tag{3.2}$$

The central wavelength, λ_0, is set to 850nm. The calculated result reaches the maximum value when OPD_2 exactly equals to OPD_1, marked by the red arrow in *Figure 3-2*. Except for the maximum peak, there exist several local peaks when,

$$\mathrm{OPD}_1-\mathrm{OPD}_2=N\lambda_c,(N=...-2,-1,0,1,2,...) \tag{3.3}$$

λ_c indicates the mean wavelength of the light source. Equation (3.1) can be approximately simplified as,

$$\begin{aligned} I &= \int_{\lambda_1}^{\lambda_1} \frac{1}{2} I(\lambda) F_1 F_2 \cos[\frac{2\pi}{\lambda} \cdot (\mathrm{OPD}_1 - \mathrm{OPD}_2)] \, \mathrm{d}\lambda \\ &\sim \int_{\lambda_1}^{\lambda_1} \frac{1}{2} I(\lambda) F_1 F_2 \cos(\frac{2\pi}{\lambda} \cdot N\lambda_c) \, \mathrm{d}\lambda \end{aligned} \tag{3.4}$$

Given the nature of the broadband source, we obtain the neighboring local peaks when λ_c satisfies,

$$\frac{2\pi}{\lambda} \cdot N\lambda_c \approx 2\pi N \tag{3.5}$$

Therefore,

$$\int_{\lambda_1}^{\lambda_1} \frac{1}{2} I(\lambda) F_1 F_2 \cos(\frac{2\pi}{\lambda} \cdot N\lambda_c) \, \mathrm{d}\lambda \approx \int_{\lambda_1}^{\lambda_1} \frac{1}{2} I(\lambda) F_1 F_2 \, \mathrm{d}\lambda \tag{3.6}$$

It is noticed that the cosine term $\cos(\frac{2\pi}{\lambda} \cdot N\lambda_c)$ does not strictly equal to 1. Thus, the integration of Equation (3.6) gives a smaller value, showing as the weaker neighboring peaks.

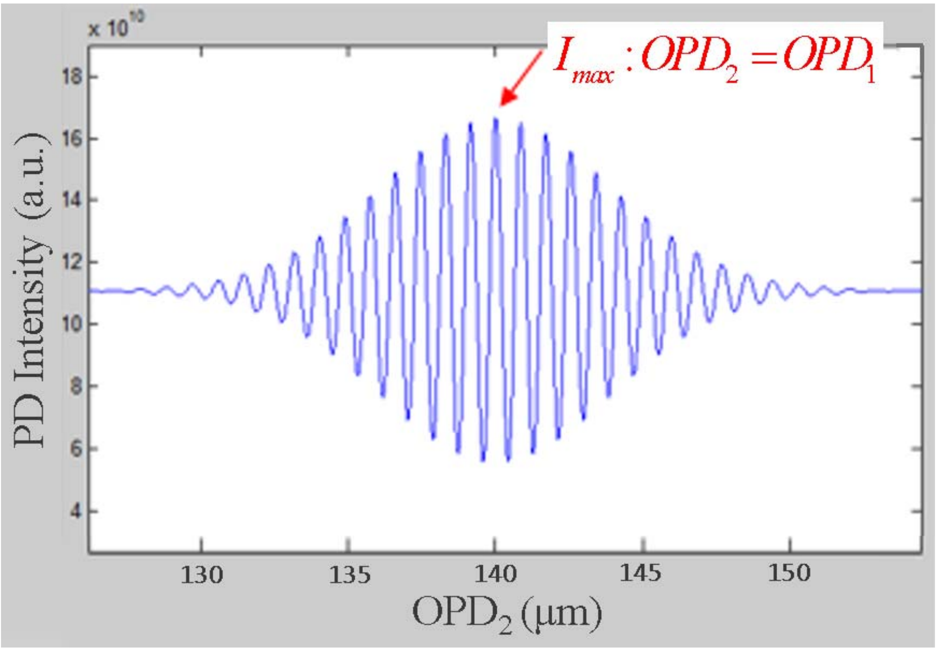

Figure 3-2 Simulated S-WLI spectrum.

When the OPD difference is large, such as,

$$|OPD_2 - OPD_1| > 10\lambda_c \tag{3.7}$$

The integration of Equation (3.1) shows significantly reduced peak fringe, as compared to the maximum value. Such behavior is a result of the broadband source, which has a wavelength range, for example, from λ_1 to λ_2 ($\lambda\epsilon[\lambda_1, \lambda_2]$). When λ_c is considered as the central wavelength, we get the following equation,

$$\frac{\lambda_c}{\lambda_2} < 1 < \frac{\lambda_c}{\lambda_1} \tag{3.8}$$

Equation (3.8) can be approximately rewritten as,

$$\begin{aligned} &1 - \delta < \frac{\lambda_c}{\lambda} < 1 + \delta \\ &\delta \approx \lambda_c - \lambda_1 \approx \lambda_2 - \lambda_c \end{aligned} \tag{3.9}$$

δ is usually a small and positive number. Its value dependents on the spectral width of the broadband light and the central wavelength λ_c. Thus, the variable in the cosine term has a range,

$$2N\pi - 2N\pi\delta < \frac{2\pi}{\lambda} \cdot N\lambda_c < 2N\pi + 2N\pi\delta \tag{3.10}$$

Deduced from Equation (3.5) and (3.10), when the integer N is small, $\frac{2\pi}{\lambda} \cdot N\lambda_c \approx 2\pi N$, then $\cos(\frac{2\pi}{\lambda} \cdot N\lambda_c)$ nearly equals 1. However, when the fringe order N is large, the absolute value of $|2N\pi\delta|$ could be large enough to beyond a half period,

$$|2N\pi\delta| \geq \pi \tag{3.11}$$

Instead of getting the maximum value, the cosine term $\cos(\frac{2\pi}{\lambda} \cdot N\lambda_c)$ reaches its minimum value when doing the integration of Equation (3.12). In the simulation, the optical spectrum of the LED is set to 850nm ± 60nm, which gives that $\delta = 0.071$. Therefore, beyond ±15th fringe order, the fringe pattern becomes negligible, shown in *Figure 3-2*.

$$I = \int_{\lambda_1}^{\lambda_1} \frac{1}{2} I(\lambda) F_1 F_2 \cos(\frac{2\pi}{\lambda} \cdot N\lambda_c) \, \mathrm{d}\lambda \tag{3.12}$$

3.1.3 Application of Scanning White Light Interferometry in Optical Sensors

The S-WLI method has been widely used in many optical systems for interferometry-based optical measurements [7, 16]. A typical application is a surface profiler [17] (*Figure 3-3* (a)). In which a beam splitter reflects the interference signal to a 2-D camera, while moving the reference objective interferometer by a Piezoelectric Transducer (PZT), the camera, therefore, calculates an area of the surface profile of the object. A similar optical system was applied to measure the thin film thickness [2], with terrace structure on the substrate, shown in *Figure 3-3* (b). In the system, a movable mirror reflector tunes the reference F-P cavity.

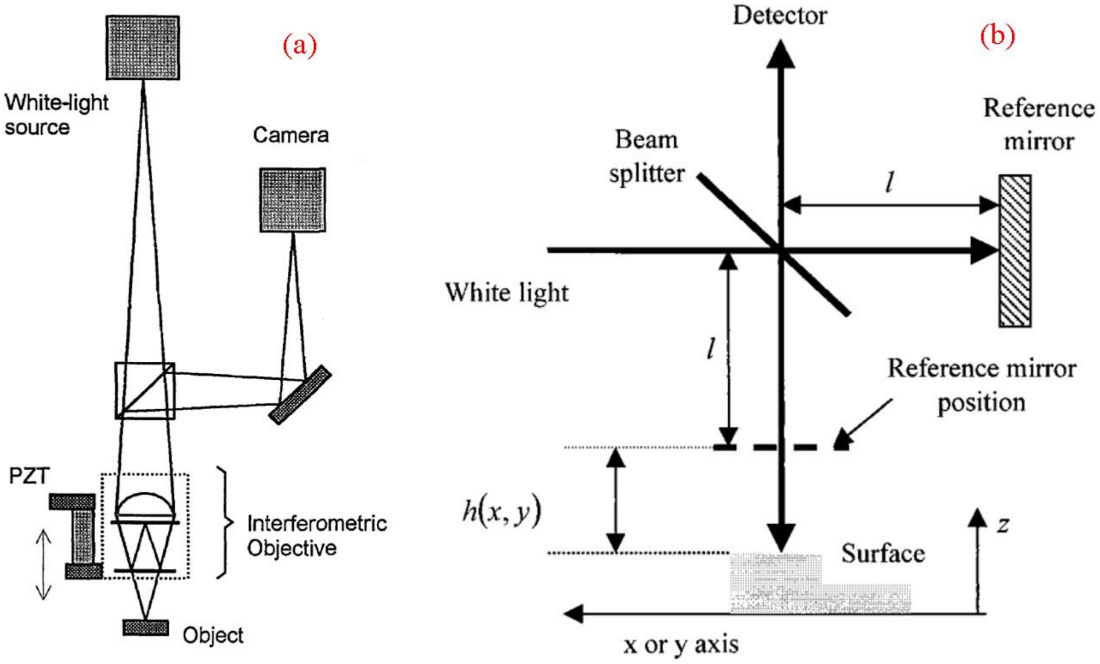

Figure 3-3 Applications of the S-WLI interferometers in (a) 2-D surface profiler [17] and (b) thin film thickness measurement [2].

Some sensing applications are designed to adopt S-WLI algorithm into the optical-fiber-based Fabry-Perot sensors. In 1991, Chen et al. [18] developed a strain sensor, which mounted a segment of the optical fiber on a cantilever beam as a strain gauge. The optical fiber deforms together with the cantilever, which provides the OPD scanning. Wang et al.[12] use the S-WLI to demodulate the fiber FPI pressure sensors. Examples were demonstrated in several other applications, such as the absolute distance measurement [5, 19], the strain sensor [13], and the position sensing [20], etc. Although the S-WLI have been demonstrated in many sensing applications, their constructions are usually complex and bulky. Besides, some components used in the system are expensive, such as a nano-scale precise piezoelectric translation stage, or a high-quality optical wedge. Therefore, the total cost is relatively high. S-WLI technique for fiber optic sensor also suffers from high cost and instability issue. Researchers were trying to build low-cost S-WLI systems in the past decades. Li et al. [21] introduced a compact and potentially low-cost optical path scanner by a segment of sealed diesel liquid in a hollow tube. A thermoelectric-cooling chip controls and tunes the diesel F-P. Due to the relatively large thermal expansion, the diesel length changes a lot, which is capable of covering a relative large OPD range. However, the liquid sealing and the evaporation issue reduces its reliability. Other examples, such as avoid using any moving component [12, 13], do not essentially reduce the system cost.

3.2 Design of Low-Cost S-WLI interrogator

3.2.1 Silica Glass Wafer Optical Path Scanner

In this study, we introduce a novel low-cost optical path scanner for the F-P sensor. It is built with only a piece of silica glass wafer and a linear CCD array. It works by using light divergence of an optical fiber. It is well known that the optical fiber emits a diverged light within a solid angle. It is determined by the fiber's numerical aperture (NA). Therefore, when an optical fiber illuminates a parallel silica wafer, the incident angles to the wafer hold a range, as scketched in Figure *3-4*. The diverged reflection beams, from the wafer surface, can be collected by a linear CCD array.

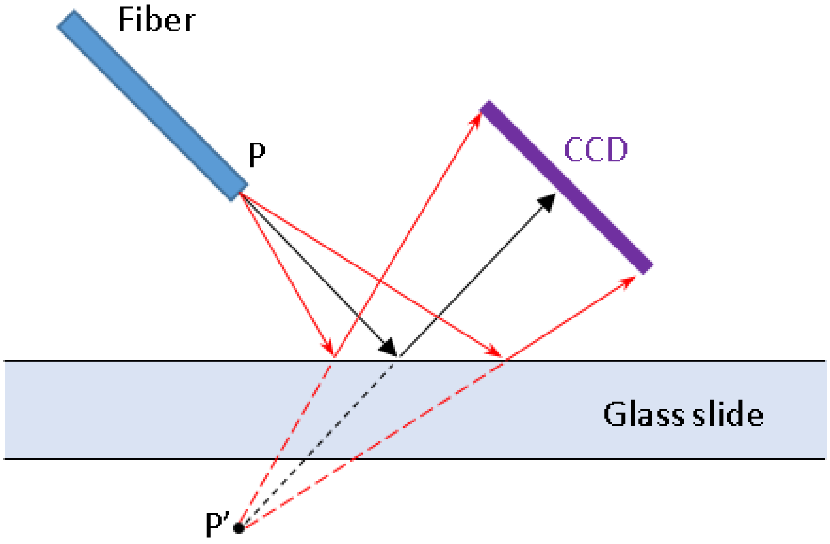

Figure 3-4 The diagram showing an optical fiber illuminates a silica glass wafer.

As shown in Figure *3-5*, when the incident light is reflected by the top and bottom surfaces of the silica wafer, a detector lays at the reflection angle receives a coherent optical signal. The optical power depends on the status of the interference, which is determined by the optical path difference between the two surficial reflectors. At the incident angle *i*, the *OPD* is calculated by,

$$\begin{aligned} OPD &= \overline{OA} + \overline{OB} - \overline{OC} \\ &= \frac{2dn_{silica}}{cos(\gamma)} - 2d \cdot tan(\gamma) sin(i) \end{aligned} \tag{3.13}$$

d and n_{silica} represent the thickness and the refractive index of the silica wafer, respective. According to Snell's Law,

$$\sin(i) = n_{silica} sin(\gamma) \tag{3.14}$$

The OPD of the silica wafer is deduced as,

$$OPD = \frac{2d(n_{silica} - \sin^2 i)}{\sqrt{n_{silica}{}^2 - \sin^2 i}} \tag{3.15}$$

According to Equation (3.15), the OPD of the silica wafer depends on the incident angle *i* and the wafer thickness *d*. In practice, *d* is usually constant. Thus, the silica wafer OPD is only a function of the incident angle. Since an optical fiber launches a diverged light to the silica wafer, a range of incident angles means a range of OPDs. The so-called "OPD scanner" is not a construction of mechanical scanning, but using a linear CCD array to record light intensities at different reflection angles, and read the pixel intensities along the CCD. Of cause, other parameters, such as the length and the position of the CCD, the pixel size, and the angle of the CCD facing to the silica wafer, affect the indicated OPD range. The silica wafer OPD scanner benefits from no moving component. Hence, it has a good potential to show an excellent mechanical stability and repeatability; and more important, a low-cost.

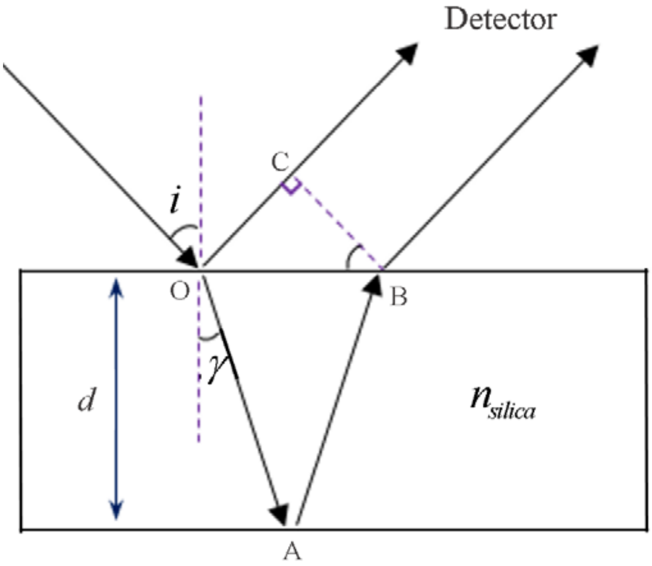

Figure 3-5 OPD of a silica glass wafer at angular incidence.

3.2.2 Optical System Design for Wafer-Based Interrogator

Figure *3-6* shows the schematic the optical sensing system. It includes an LED broadband light source, a sensing Fabry-Perot interferometer, a silica wafer OPD scanner, an optical coupler, and a computer for signal demodulation. The LED, centered at ~850 nm, has ~60 nm FWMH. The sensing F-P interferometer can be any F-P structures. In the preliminary test, it is an air gap cavity. The LED illuminates the sensing F-P cavity through a 2×2 coupler. The reflected light from the air gap F-P propagates through the coupler again and illuminates the silica wafer OPD scanner. A CCD array is positioned at around 45° tilted angle records the optical power.

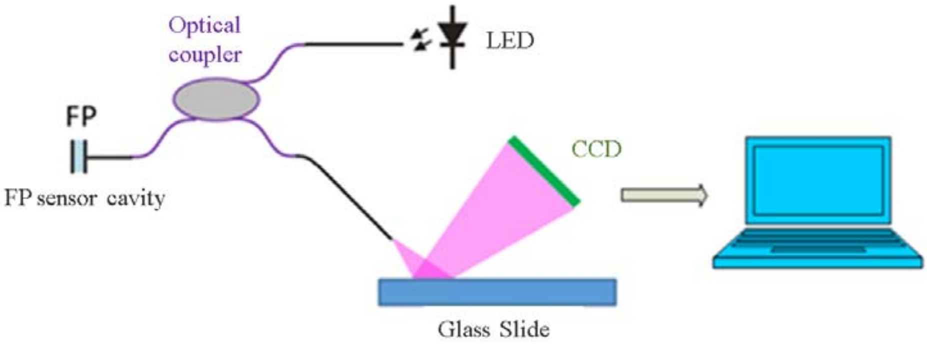

Figure 3-6 The silica wafer F-P interrogator for an air gap FP cavity.

3.2.3 Dynamic Range Analysis

As discussed by Equation (3.15), a silica-wafer-based Fabry-Perot interrogator can project the OPD information to the spatial distribution of a photodetector array, by relating it to the fiber incidence angles. It is important to analyze its dynamic range and the linearity, to get a deep understanding to this F-P interrogator. A more precise model is established based on the coordinate system shown in Figure *3-7* [22].

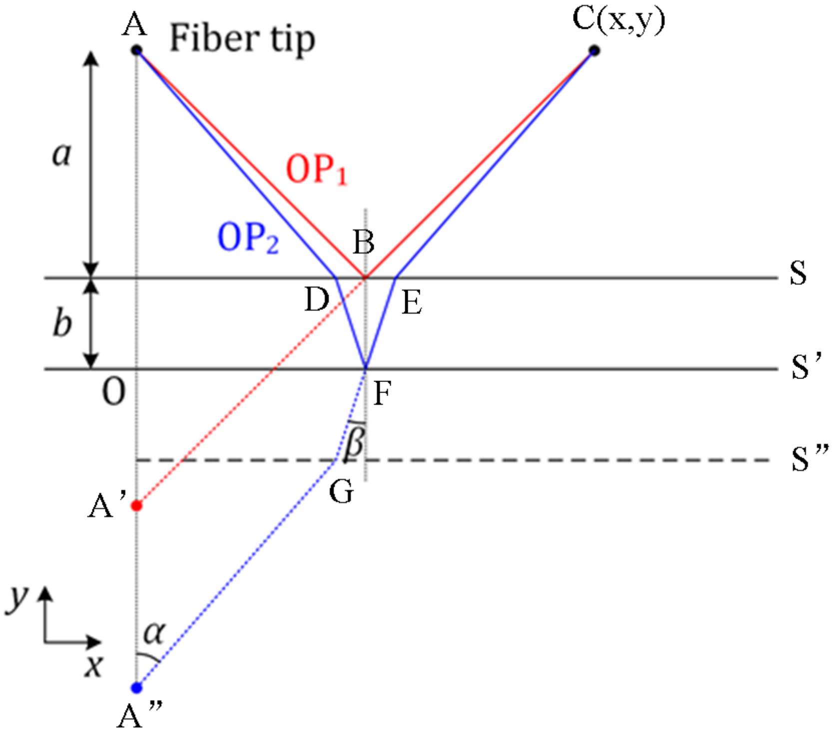

Figure 3-7 Optical geometry of the wafer based interrogator [22].

The fiber end surface is marked as Point A. The vertical distance between the fiber tip, and the upper wafer surface (s) equals *a*. The wafer thickness is *b*. The image of Point A regarding to surface aS is noted as A'. Light reflected by the upper surface is collected at point C(x,y), which represents the position of an image sensor pixel. The optical path distance $OP_1(x,y)$ between A and C can be calculated as,

$$\begin{aligned} OP_1(x,y) &= \overline{AB} + \overline{BC} \\ &= \sqrt{x^2 + (y-b+a)^2} \end{aligned} \tag{3.16}$$

Similarly, the image of the fiber tip A to the lower surface (s') is denoted as A". According to the theory of Geometric Optics, A" can be obtained by imaging both Point A and the upper surface (s) regarding to the lower surface (s'). The optical path length ($OP_2(x,y)$), reflected by the lower surface, can be written as,

$$
\begin{aligned}
OP_2(x,y) &= \overline{AD}+\overline{DF}+\overline{FE}+\overline{EC} \\
&= \overline{A''G}+\overline{GE}+\overline{EC} \\
&= \frac{a}{\cos\alpha}+\frac{y-b}{\cos\alpha}+\frac{2bn}{\cos\beta}
\end{aligned}
\tag{3.17}
$$

In Equation (3.17), α and β represent angles of the incident light outside and inside the silica wafer, respectively. *n* is the refractive index of silica. Based on Snell's law,

$$\sin\alpha = n\sin\beta \tag{3.18}$$

Deduced from the above equations, two expressions were obtained for $OP_2(x, y)$, in which sin β is the only wavelength independent variable,

$$
\begin{aligned}
OP_2(x,y) &= \frac{y-b+a}{\sqrt{1-n^2\sin^2\beta}}+\frac{2bn}{\sqrt{1-\sin^2\beta}} \\
&= \frac{2b}{\sqrt{1-\sin^2\beta}}\cdot\left(n-\frac{1}{n}\right)+\frac{x}{n\sin\beta}
\end{aligned}
\tag{3.19}
$$

By solving Equation 3.19, we can calculate sinβ first, and then $OP_2(x, y)$. Thus, the Optical Path Difference (OPD) between the two interfering light is calculated by,

$$OPD(x,y) = OP_2(x,y) - OP_1(x,y) \tag{3.20}$$

OPDs of any other light receiving points can be calculated similarly. Besides the OPD between the two reflecting light, we need to consider a potential phase shift during the second reflection. The additional phase shift occurs at total internal reflection [23]. In such situation, the incidence angle is greater than the critical angle. Given the system geometry, it will not exist in our case. Specifically, the critical angle for fused silica is 43.5°. When a fiber points to the wafer at 45°, the incidence angle inside the wafer is about 29.1°, which assures that no additional phase shift will be introduced.

For building an applicable wafer-scanner, we need a linear CCD array to collect the spatially distributed optical power. In fact, the CCD can be installed at any angle facing to the silica wafer, shown in *Figure 3-8*. All types of installations collect optical power within a range of incident angles. Therefore, further analysis is needed to choose the best construction.

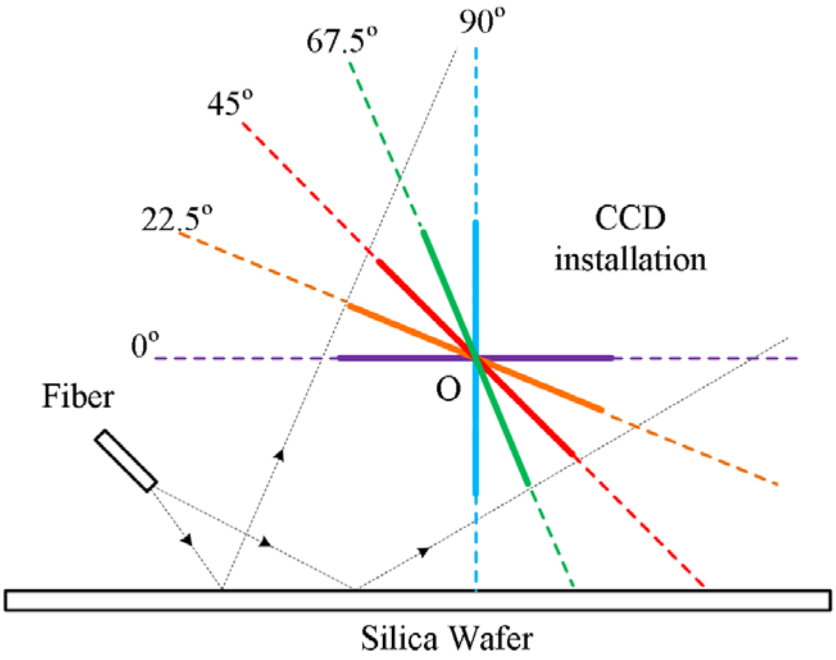

Figure 3-8 Different angled CCD installations for light collection.

Our simulation is based on the structure set in *Figure 3-7*. Instead of using the x-y coordinate, we describe the CCD model according to *Figure 3-9*. It sets a natural coordinate via using the length of the CCD (L) as the coordinate. The new coordinate relates to the x-y coordinate by the incident angle i,

$$\begin{aligned} dy &= dL\cos(i) \\ dx &= -dL\sin(i) \end{aligned} \tag{3.21}$$

We then relate the silica wafer OPD, to the position of the CCD camera. The OPD calculation for a detector at any point (x,y) is deduced from Equations (3.16) to (3.20). Therefore, when substituting Equation (3.21) to the above equations, the relationship between the OPD and the length of the CCD is established.

In the simulation, the center of the CCD locates at (x_0, y_0). It is set as the origin. All the parameters, defined in *Figure 3-7*, are set as a = 0.3 mm and b = 54 μm. We roughly set the origin point by 45° incidence, which gives that x_0=40mm and y_0=40mm. Accordingly, all the other points along the CCD can be projected to the x-y coordinates by,

$$\begin{aligned} x &= x_0 - L\sin(i) \\ y &= y_0 + L\cos(i) \end{aligned} \tag{3.22}$$

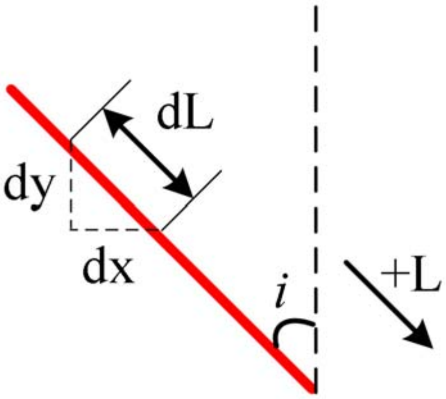

Figure 3-9 Natural coordinate set for simulation.

We then substitute Equation (3.22) into Equations (3.16) to (3.20). The calculated result is illustrated in *Figure 3-10*. The horizontal axis indicates the spatial position of the CCD camera. Its zero position displays the camera center. The vertical axis presents the corresponding wafer OPD.

The 2-D CCD camera, used in the experiment, has a 2/3" image sensor with 1388×1024 pixels. The pixel is a 4.7μm× 4.7μm square. Therefore, the CCD is ~6.5mm long. The two vertical dash lines denote the region where the CCD camera locates. The simulation is done in a much larger region in case a longer CCD is used in the future.

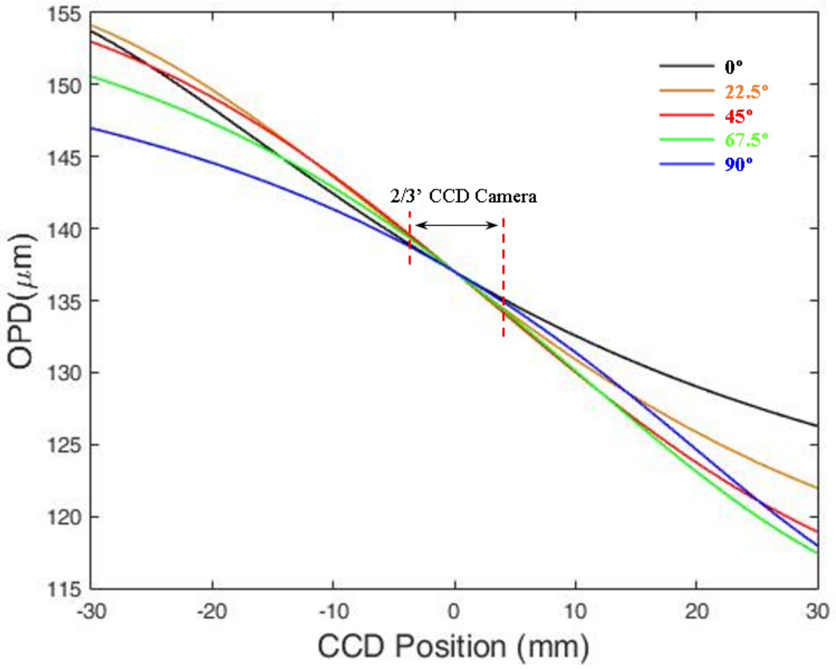

Figure 3-10 Simulation for OPD distribution along the CCD at different angles (0°, 22.5°, 45°, 67.5°, and 90°) facing the silica wafer. The 2/3" CCD is placed at 45° to the wafer and 40 mm away from the wafer surface.

Figure 3-11 is the enlarged central region of *Figure 3-10*. It shows the dynamic range of the reference wafer OPD as a function of the CCD length. Given the same CCD length, the dynamic range has the maximum value when the CCD faces the wafer at 45°. Our CCD is able to cover ~5.5µm OPD scan range. It is crucial to make sure that the sensor OPD must lie within this range. In the actual implementation, we roughly estimate the sensing OPD in advance and then polish or etch the fused silica wafer to the desired thickness to cover this range.

It is noticed that the dynamic range of the other case when the CCD tilts at a different angle, such as 22.5° or 62.5°, does not have a significant reduction. We, therefore, need a deeper analysis to guide the optical system design.

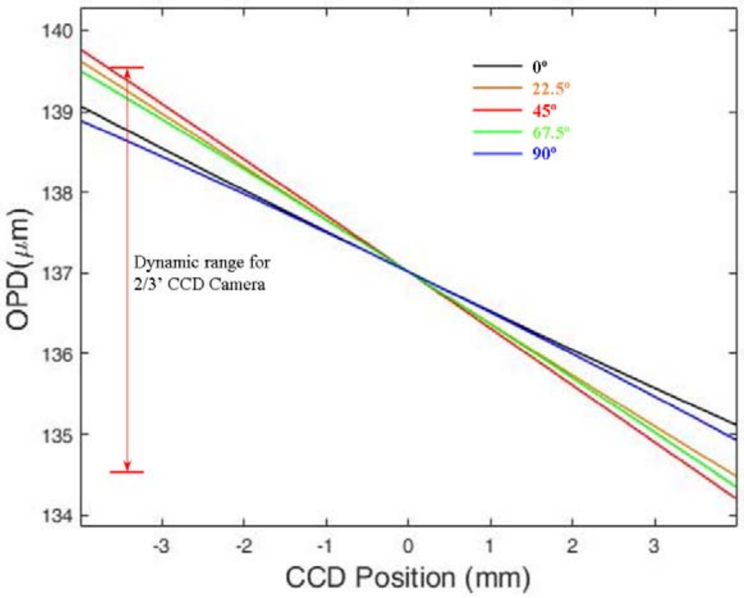

Figure 3-11 The enlarged image showing the dynamic range of a 2/3” CCD camera used in the current experiment. The length of the CCD camera allows covering approximately 5.5μm reference OPD.

3.2.4 Linearity Analysis

The linearity property describes the spatial distribution uniformity of the silica wafer OPDs. We characterize it by two expressions, $\frac{dOPD}{dL}$ and $\frac{d^2OPD}{dL^2}$. $\frac{dOPD}{dL}$ describes the OPD change, over the unit length of the CCD camera. $\frac{d^2OPD}{dL^2}$ quantifies the rate of the OPD change. Both of them can be calculated from the OPD vs. CCD Position curves illustrated in *Figure 3-10*.

The coordinate system is defined the same as *Figure 3-9*. Compared the result in *Figure 3-12*, the CCD camera, which tilts at 45º to the silica wafer, has the best linearity. From the simulation, the OPD change, over the unit CCD length, is almost constant in a certain region, marked in the dash-circle.

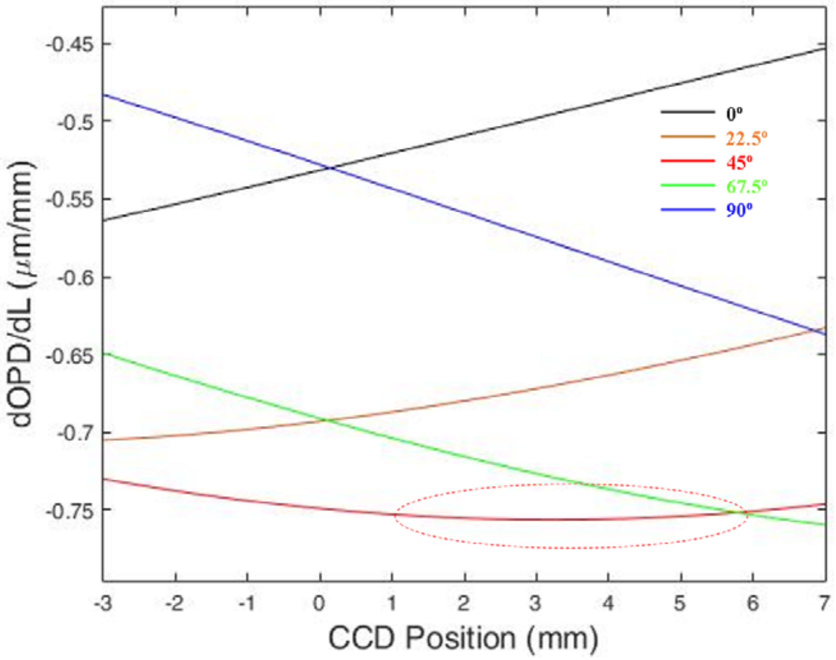

Figure 3-12 Simulation of the OPD change over the unit length of the CCD position. The CCDs are set to 0º, 22.5º, 45º, 67.5º, and 90º facing the silica-wafer-interrogator.

Figure 3-13 shows the second derivative of the OPD vs. CCD position curve. It describes quantitively, the rate of the OPD change along the CCD length. Similar to the first derivative calculations, the best region locates at ~3mm away from the origin, with 45º tilted angle, pointed by the red arrow. Within that region, the OPD change rate, over 1mm CCD length, is smaller than 0.1%.

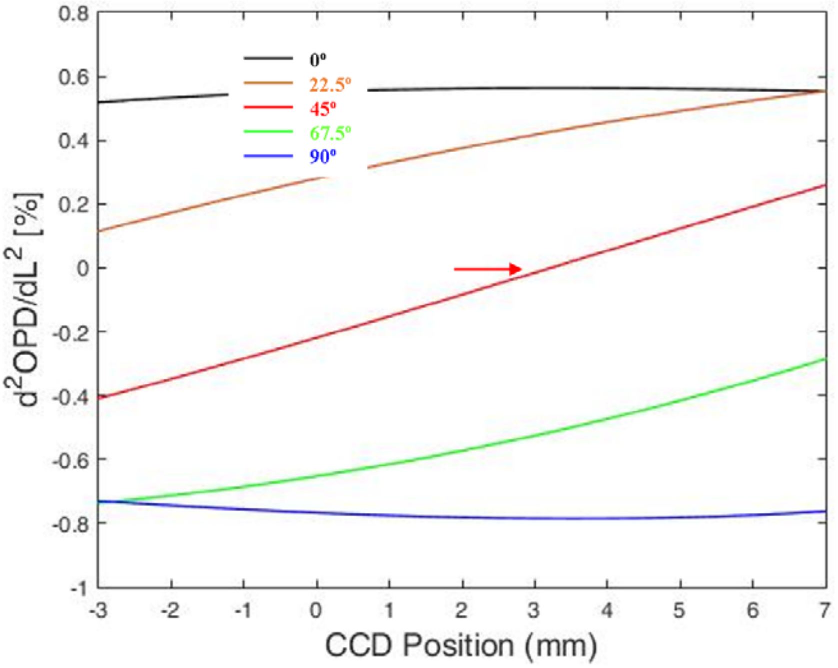

Figure 3-13 The OPD change rate along the CCD positions. Simulations were done for CCDs facing the wafer interrogator at 0º, 22.5º, 45º, 67.5º, and 90º.

The above calculations provide a good guide to build the optical system. It is noticed that the position with the best linearly for a 2/3” CCD camera, is approximately 3 mm away from the origin set for simulation. We, hence, arrive at the conclusion that the CCD, which places at 45º to the silica-wafer-interrogator, has the largest dynamic range and the best linearity.

3.2.5 Effective OPD

The model set for *Figure 3-8* considers the fiber tip as a point source. However, a commonly used optical fiber has a core size range from 9μm to several hundreds of microns, depending on the type of fiber being installed in the system. The extended fiber core diameter broadens the OPD value that is represented by a given imaging pixel, which would lead to a reduced fringe contrast. In this part, a simulation is done to investigate the influence of the fiber core diameter.

The sapphire fiber has a relatively large core diameter (75μm). Therefore, a multimode fiber will be spliced after it in order to reduce the transmission loss of fiber core size mismatch. The actual setup uses a 105/125 step-index multimode fiber. Since the broadband source illuminates the sapphire wafer F-P sensing cavity at almost all angles, especially in the case that using environmental thermal radiation as the light source. We, hence, assume that all modes are excited. The power distribution in the multimode fiber is not a Gaussian shape but more evenly distributed in the core region. Therefore, as a simple estimation, we consider the multimode fiber tip as an area source, as shown in *Figure 3-14*. The two points on the opposite edges of the multimode fiber, launch light beams that travel through different optical paths and therefore, show different OPDs when collected by the same CCD pixel.

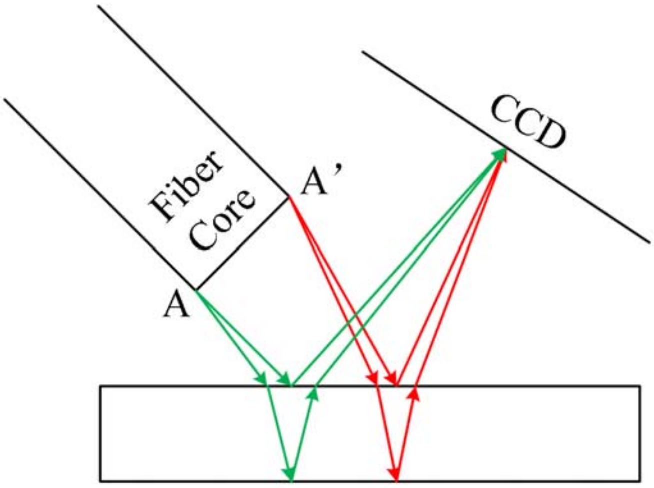

Figure 3-14 Schematic of multimode fiber illuminates the silica wafer.

A simulation was done in the 2-D plane cutting across the fiber diameter. The other points on the multimode fiber tip outside this plane can be calculate similarly by rotation. When two different points on the fiber tip illuminate the wafer and then reflect to the same imaging pixel, the light beams experience different OPDs. The two points located at the opposite edges of the fiber core will generate the largest OPD differences between the two paths; we consider this difference to be the reference OPD range represented by a single image pixel. The OPD range at the same imaging pixel as a function of the fiber core diameter is shown in *Figure 3-15*.

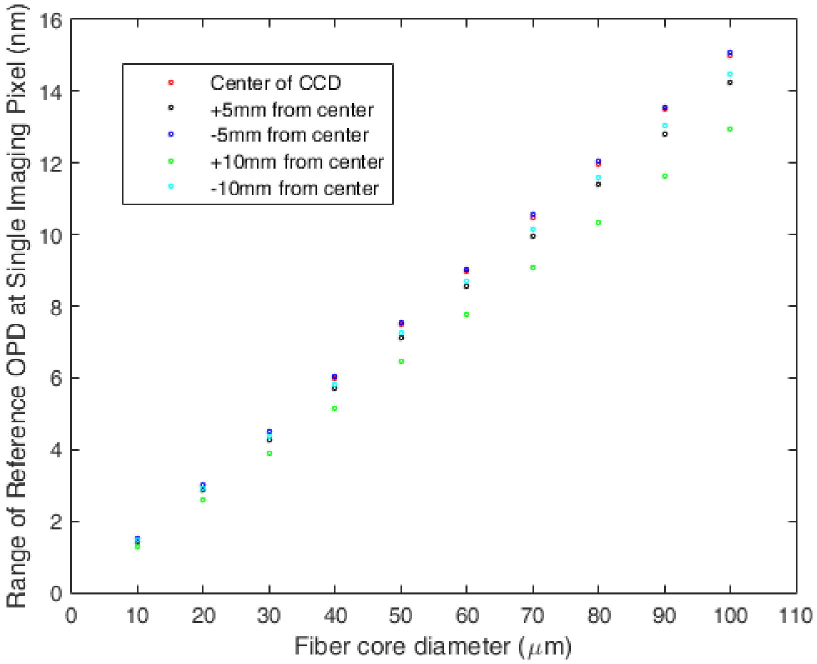

Figure 3-15 Reference OPD range at single pixel position as a function of fiber core diameter.

The calculation is based on Equations 3.16 ~ 3.22. The coordinate is the same as Figure 3-8. The fiber center is set at (0, 0.3), which is 300μm away from the silica wafer; the wafer thickness is set to 54μm. The calculated CCD imaging pixels setting at points (30, 50), (35, 45), (40, 40), (45, 35), (50, 30), which is based on the optimized 45° CCD installation, discussed in the previous section. Since a 2/3" CCD was used, the calculation was done in a length ±10mm away from the CCD center at 5mm spacing. The fiber core diameter varies from 10μm to 100μm, at 10μm spacing. The calculation shows that the fiber core diameter influence the reference OPD being represented by a CCD image sensor. In the ideal case when the fiber tip is considered as a point source, a CCD pixel represents only one reference CCD, supposing the pixel size is small enough to be negligible. When considering the fiber core size, an imaging pixel will be covered by a range of OPD values. Generally, a larger core diameter shows a larger OPD range at the same pixel. Besides, the OPD range is position dependent. It is slightly affected by the positions of the pixel along the CCD because the incident angle from the fiber tip to the wafer will be different in order to illuminate the same target pixel. The simulation gives the maximum value of 15.1nm when using a 100μm-core multimode fiber to illuminate a 17mm (2/3”) long CCD, which is installed 40mm away from the silica wafer. The corresponding image pixel locates at approximately -5mm away from the simulated CCD center.

The simulation indicates that a pixel on the CCD presents an effective OPD, which covers a small range of OPD values; the variation is approximately in ten-nanometer scale. According to Equation 3.1, the total power (*I*) received by an imaging sensor is proportional to,

$$I \sim \int_{\lambda_1}^{\lambda_1} \cos[\frac{2\pi}{\lambda} \cdot (\mathrm{OPD}_1 - \mathrm{OPD}_0)] \mathrm{d}\lambda \tag{3.23}$$

In the above function, OPD_0 represents the optical path distance of the sensing F-P cavity, which is a given number under certain status. In the ideal case, the integration gets its wavelength independent maximum value when the single value of reference OPD_1 equals OPD_0. If the reference OPD has a range, the integration cannot get its theoretical maximum value. However, it still get a peak value when the effective OPD, which can be defined by the center of the reference OPD, equals the sensing OPD. In this case, the fringe contrast reduces.

Similarly, the range of reference OPD at any single sensing imaging pixel should not cause the value in the cosine term has a range that beyond π/2. Otherwise, the constructive and the destructive interferences cancel each other, which flattens the fringe pattern. This requirement is written as,

$$\frac{2\pi}{\lambda_c} \cdot \delta OPD < 0.5\pi \tag{3.24}$$

When δOPD uses the maximum value (15.1nm) of reference OPD range and λ_c = 850nm, $\frac{2\pi}{\lambda_c} \cdot \delta OPD = 0.036\pi << 0.5\pi$. The calculation indicates that, the cosine term still has a value that closely equals 1. When integrating over that small range of reference OPD, it get the local peak value, compare to the other effective OPDs that is further away from OPD_0.

As a conclusion, the amount of reference OPD expending caused by the 100μm core size multimode fiber, only reduce the fringe contrast.

3.2.6 Signal Demodulation Algorithm

This section discusses the signal demodulation algorithm in detail, according to the optical system shown in *Figure 3-6*. We denote the optical path length of the sensing F-P interferometer and the silica wafer interrogator as OPD_0 and *OPD'*, respectively. The electric field, $E_1(\lambda)$, which is reflected by the sensing F-P can be written as,

$$E_1(\lambda) = e^{j\psi_0}(C_1 e^{j\pi} + C_2 e^{j\phi_0}) \tag{3.23}$$

ψ_0 represents the initial phase, and ϕ_0 equals to $2\pi OPD_0/\lambda$. The two coefficients C_1 and C_2 equal to $\sqrt{R_1}$ R_1 and , respectively. is the reflection coefficient of the F-P cavity. The coherent light will then illuminates the silica wafer F-P interrogator at a certain incident angle, the electrical field $E_2(\lambda)$, which corresponds to a certain *OPD'*, can be written as,

$$E_2(\lambda) = E_1(\lambda)e^{j\psi'}(C_3 e^{j\pi} + C_4 e^{j\phi'}) \tag{3.24}$$

C_3 and C_4 approximately equal to $\sqrt{R_2}$ and $\sqrt{R_2(1-R_2)}$, respectively. R_2 is reflection coefficient at silica-air interface. ϕ' is defined as $2\pi OPD'/\lambda$, where *OPD'* is optical path distance of the silica wafer, which relates to this certain incident angle. Therefore, the optical power received by the CCD, at a certain imaging pixel, can be written as,

$$I_{OPD'} = \int_0^\infty s(\lambda)E_2(\lambda)E_2^*(\lambda)d\lambda \tag{3.25}$$

$s(\lambda)$ denotes the power spectrum of the LED. We can expand Equation (3.25) to be,

$$
\begin{aligned}
I_{OPD'} = & \int_0^\infty s(\lambda)(C_1^2 + C_2^2)(C_3^2 + C_4^2)d\lambda \\
& -2\int_0^\infty s(\lambda)C_1C_2(C_3^2 + C_4^2)\cos(\phi_0)d\lambda \\
& -2\int_0^\infty s(\lambda)C_3C_4(C_1^2 + C_2^2)\cos(\phi')d\lambda \\
& +2\int_0^\infty s(\lambda)C_1C_2C_3C_4\cos(\phi_0 + \phi')d\lambda \\
& +2\int_0^\infty s(\lambda)C_1C_2C_3C_4\cos(\phi_0 - \phi')d\lambda
\end{aligned}
\tag{3.26}
$$

In the above equation, ϕ_0, ϕ' and $\phi_0+\phi'$ represent $2\pi OPD_0/\lambda$, $2\pi OPD'/\lambda$, and $2\pi(OPD_0+OPD')/\lambda$, respectively. They are wavelength-dependent phase terms. The first line of integration indicates the DC component. The integrations from Lines 2 to 4 are ignorable if OPD_0 and OPD' are much larger than the spectrum-dependent equivalent central wavelength (λ_c) of the light source, which must be true for most of the WLI measurements. It is a result of integrating over a broad wavelength range, such as tens of nanometers. The cosine term, as a modulation in the integration, will have many full periods, which cancel each other to make the integration value negligible. A similar discussion is deduced from Equations (3.7) to (3.12), where we discuss the gradually reduced neighboring peaks. In the simulation, we set R_1=0.076, which is the reflection between sapphire and air interface. And R_2, the reflection between silica and air interface, equals 0.034. The LED is described by a Gaussian power distribution [21],

$$
s(\lambda) = \frac{1}{4\Delta\lambda\sqrt{\pi \ln 2}} e^{-\frac{(\lambda-\lambda_c)^2}{4\ln 2\Delta\lambda^2}}
\tag{3.27}
$$

The central wavelength λ_c equals 850nm. When integrating from λ_1 (750nm) to λ_2 (950nm), the calculated values of Line 2 to 4 is approximately six orders of magnitude smaller as compared to the DC component, and the integration of the last line.

$$\begin{aligned}&\frac{2\int_{\lambda_1}^{\lambda_1} s(\lambda)C_1C_2(C_3^2+C_4^2)\cos(\phi_0)d\lambda}{\int_{\lambda_1}^{\lambda_1} s(\lambda)(C_1^2+C_2^2)(C_3^2+C_4^2)d\lambda}\\ \sim&\frac{2\int_{\lambda_1}^{\lambda_1} s(\lambda)C_3C_4(C_1^2+C_2^2)\cos(\phi')d\lambda}{\int_{\lambda_1}^{\lambda_1} s(\lambda)(C_1^2+C_2^2)(C_3^2+C_4^2)d\lambda}\\ \sim&\frac{2\int_{\lambda_1}^{\lambda_1} s(\lambda)C_1C_2C_3C_4\cos(\phi_0+\phi')d\lambda}{\int_{\lambda_1}^{\lambda_1} s(\lambda)(C_1^2+C_2^2)(C_3^2+C_4^2)d\lambda}\\ \sim&10^{-6}\end{aligned} \tag{3.28}$$

The last line of Equation (3.26) shows the interference. If the spectrum of a white light source is not too broad, we can assume that $\lambda_c/\lambda\approx 1$. In the cases of, ϕ_0-$\phi'=2N\pi$,

$$\begin{aligned}&\phi_0-\phi'=2N\pi,(N=0,\pm1,\pm2,\ldots)\\ &\Rightarrow OPD_0-OPD'=N\lambda_c,\end{aligned} \tag{3.29}$$

The cosine term $\cos(\phi_0-\phi')\approx 1$. Therefore, the integration presents a maximum local value. In a special case, *N=0*, is noted as the zero-order fringe. In this case, the cosine term strictly equals zero, which is wavelength independent. Hence, the zero-order fringe appears as the strongest peak in the spectrum. Similarly,

$$OPD_0-OPD'=(N+\frac{1}{2})\lambda_c,\ (N=0,\pm1,\pm2,\ldots) \tag{3.30}$$

indicates the local minimum value.

According to the analysis in Chapter 3.2.1, the linear CCD array, which receives optical power from different reflection angles, projects the silica wafer OPDs to the corresponding imaging pixels. In other words, the pixel position directly relates to the OPDs of the sensing F-P cavity. It is how we use a fixed wafer to achieve a variable OPD scanning.

3.2.7 Fringe Contrast of the S-WLI System

For an F-P sensor, a better signal fringe contrast (F_v) is usually more desirable, which is defined as,

$$F_v = \frac{(I_{OPD'})_{max} - (I_{OPD'})_{min}}{(I_{OPD'})_{max} + (I_{OPD'})_{min}} \tag{3.31}$$

Therefore,

$$\begin{aligned} F_v &= \frac{4\int_{\lambda_1}^{\lambda_1} s(\lambda) C_1 C_2 C_3 C_4 d\lambda}{2\int_{\lambda_1}^{\lambda_1} s(\lambda)(C_1^2 + C_2^2)(C_3^2 + C_4^2) d\lambda} \\ &= \frac{2C_1 C_2 C_3 C_4}{(C_1^2 + C_2^2)(C_3^2 + C_4^2)} \end{aligned} \tag{3.32}$$

When considering the fringe contrast of the sensing Fabry-Perot cavity (F_{v0}), we get,

$$\begin{aligned} F_{v0} &= \frac{[E_1(\lambda)E_1{}^*(\lambda)]_{max} - [E_1(\lambda)E_1{}^*(\lambda)]_{\min}}{[E_1(\lambda)E_1{}^*(\lambda)]_{max} + [E_1(\lambda)E_1{}^*(\lambda)]_{\min}} \\ &= \frac{2C_1 C_2}{C_1^2 + C_2^2} \end{aligned} \tag{3.33}$$

Similarly, the silica wafer F-P interrogator has a fringe contrast (F_{v1}), which equals,

$$F_{v1} = \frac{2C_3 C_4}{C_3^2 + C_4^2} \tag{3.34}$$

Substitute Equations (3.33) and (3.34) to Equation (3.32), we get,

$$F_v = \frac{1}{2} F_{v0} F_{v1} \tag{3.35}$$

The above equation indicates that if the two F-P cavities being connected in series, the overall fringe contrast (F_v), will be affected by fringe contrast of both F-Ps.

3.3 Result and Discussion

3.3.1 Test in the Single Mode Fiber System

The actual performance of the silica wafer S-WLI interrogator is investigated by a tunable air gap FP. Figure *3-16* shows the optical system. The air gap F-P cavity is constructed by pointing a single-mode fiber PC connector to a silica reflector (Figure *3-17*). The silica reflector has the same reflectivity as the silica fiber. The reflector is mounted on a 3-axis piezoelectric stage (Melles Griot Inc.). This piezo stage tunes the air gap in nanometer resolution. The entire setup is built on a floated optical table to maintain a stable air gap. The broadband light source is a superluminescent LED (SLED) with an FWHM of ~30 nm. Its central wavelength locates at ~850 nm. A 2-D CCD camera collects the optical signal.

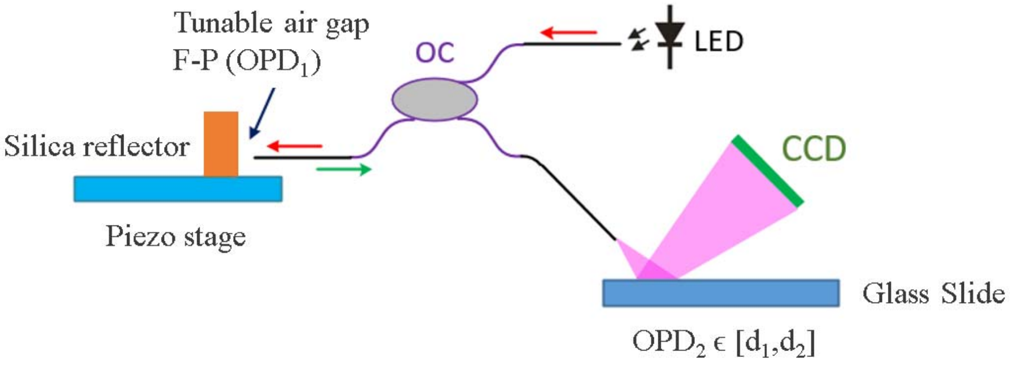

Figure 3-16 Wafer-based S-WLI interrogator investigates in a single-mode fiber system.

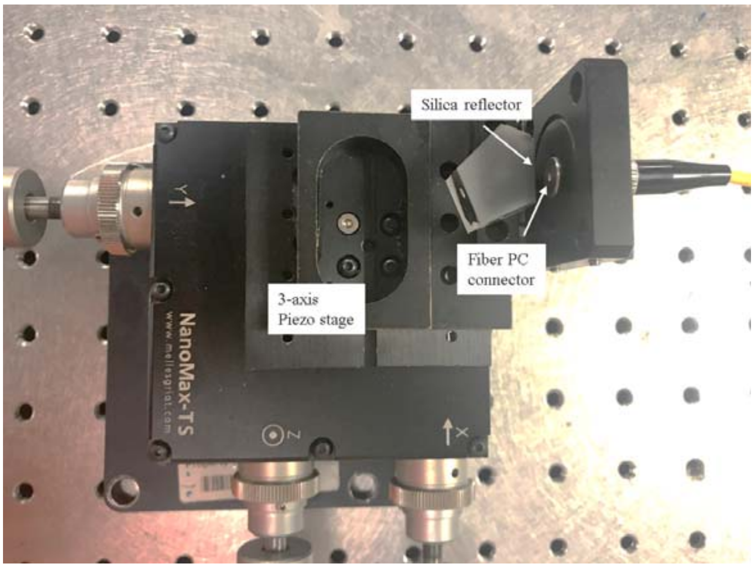

Figure 3-17 Tunable air gap Fabry-Perot cavity built with a fiber connector and a silica reflector.

3.3.2 Data acquisition

Before collecting the optical signal, the air gap was set much larger than the optical length of the silica wafer interrogator. According to Equations (3.7) to (3.11), no interference fringe was observable. The camera collected only the DC component, named as the background signal. While adjusting the air gap to get close to the silica wafer OPD, the interference fringe gradually appeared in the camera. Kept adjusting the air gap until the best fringe shows in the CCD, then the correct position was set. At the same time, we set the CCD camera to a proper distance away from the silica wafer interrogator to collect the most of the beam spot of the fiber.

Figure *3-18* illustrates the intensity on a 1388×1024 2-D CCD after removing the background. The beam spot locates almost in the center of the camera. Except for some points on the edge of the CCD, the major parts in the central area show a good fringe pattern. The dashed line along Column 550 approximately indicates the optical beam diameter.

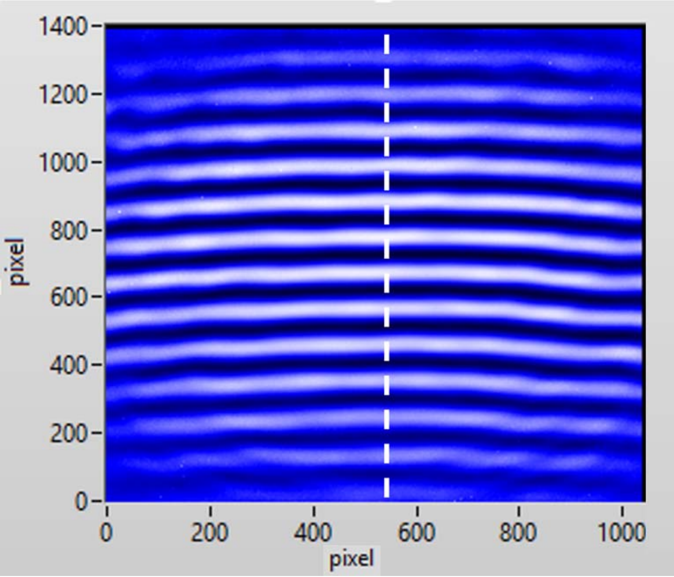

Figure 3-18 Fringe pattern on a 2D CCD [22].

As a preliminary result, a simple signal demodulation algorithm is conducted by calculating the pixel intensities along a central column of the CCD. *Figure 3-19* shows the intensities along column 550. In the first step, we find all the peaks and valleys. The curve fitting obtains two envelopes, corresponding to the peak and the valley positions, respectively. The maximum gap between the two envelopes is identified. The fringe peak, which is nearest to this point, is considered as the zero-order fringe, pointed by the red arrow in *Figure 3-19*.

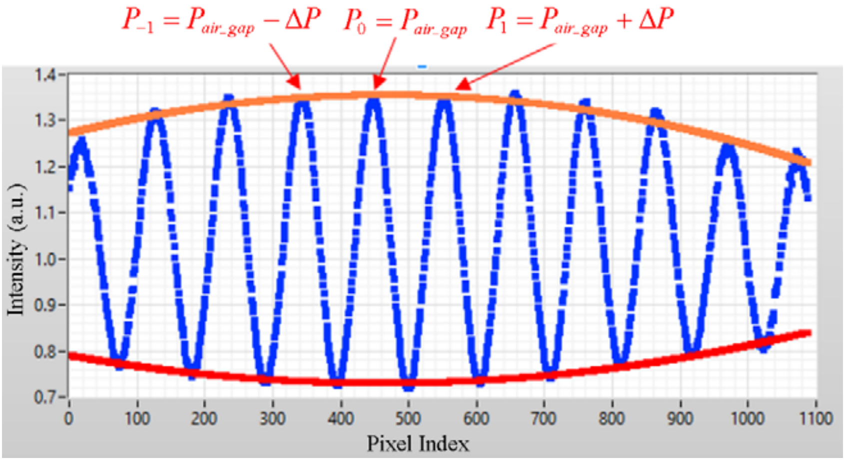

Figure 3-19 Intensities along Column 550 of the 2-D CCD.

$$\mathrm{OPD}_1 - \mathrm{OPD}_2 = N\lambda_c \tag{3.36}$$

The local peaks are generated when the OPD difference $\mathrm{OPD}_1 - \mathrm{OPD}_2$ satisfies Equation (3.29). Here OPD_2 indicates the optical distance of the silica wafer interrogator; while OPD_1 denotes the air gap OPD. N is an integer. The interrogator OPDs can be projected as the pixel indexes, by a one-to-one mapping. Therefore, the air gap OPD, represented by the zero-order peak index P_{air_gap}, relates to the other neighboring peek indexes (P_N) by,

$$P_N = N\Delta P + P_{air\_gap},\ (N = \ldots -3, -2, -1, 0, 1, 2, 3) \tag{3.37}$$

ΔP, is a constant value, which indicates the index difference between any two adjacent peaks. In fact, All the peak positions P_N and the fringe order N are known, read from the CCD camera. Therefore, the zero-order fringe calculation can be further improved via a linear regression, by using the P_N vs. N curve. In the linear regression, $P_{air-gap}$ is obtained by the intercept, at $N=0$.

3.3.3 Calibration

Once the pixel index of the air gap OPD is obtained, in practice, it can be related to the actual OPD via a calibration. Figure 3-20 shows the calibration curve, which is the air gap OPD vs. CCD pixel number. The pixel index is not an integer, but the value after peak fitting and linear regression. The air gap OPDs are calculated simultaneously by the traditional WLI algorithm as the reference. The calibration curve shows a good linearity. It matches the predicted result, which states that when the CCD is placed at 45° to the silica wafer, the pixels along the CCD reflects a linear OPD change.

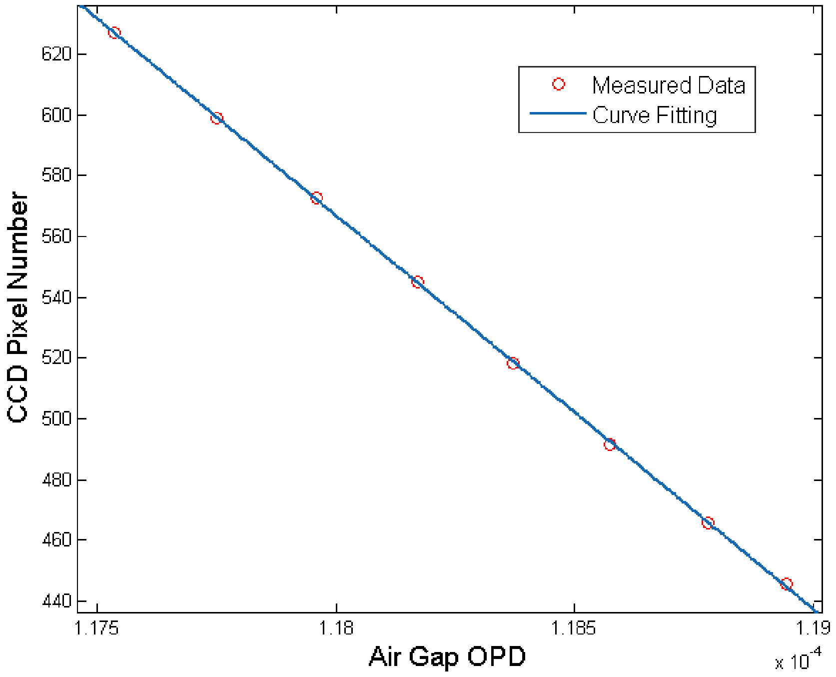

Figure 3-20 air gap OPD vs. CCD pixel number calibration curve [22].

3.3.4 Test in the Multimode Fiber System

Developing a low-cost sapphire-fiber Fabry-Perot temperature sensor is the research goal of the project. Therefore, a test in the multimode fiber system is necessary because the sapphire fiber optical sensors are built with all multimode fibers. Figure *3-21* shows schematic of the optical system with the MMF. An LED is used instead of single-mode-fiber-coupled superluminescence source. The LED spectrum centers at ~850nm with the FWHM of approximately 60 nm. In the setup, a second optical coupler is used to split one-half of the optical power to an Ocean Optics spectrometer (USB2000). The spectrometer and the camera acquire signals simultaneously. We hence calculate the air gap OPD as a calibration, based on the total phase WLI demodulation.

Compared to the single mode fiber test system (Figure *3-16*), a cylindrical lens is placed between the silica wafer interrogator and the CCD camera. It focuses the diverged light to only several lines of the 2-D CCD camera. We will discuss the functionality of the cylindrical lens in the next chapter. According to this setup, the optical power received by each imaging pixel increases more than one order of magnitude. A significantly improved signal to noise ratio was observed.

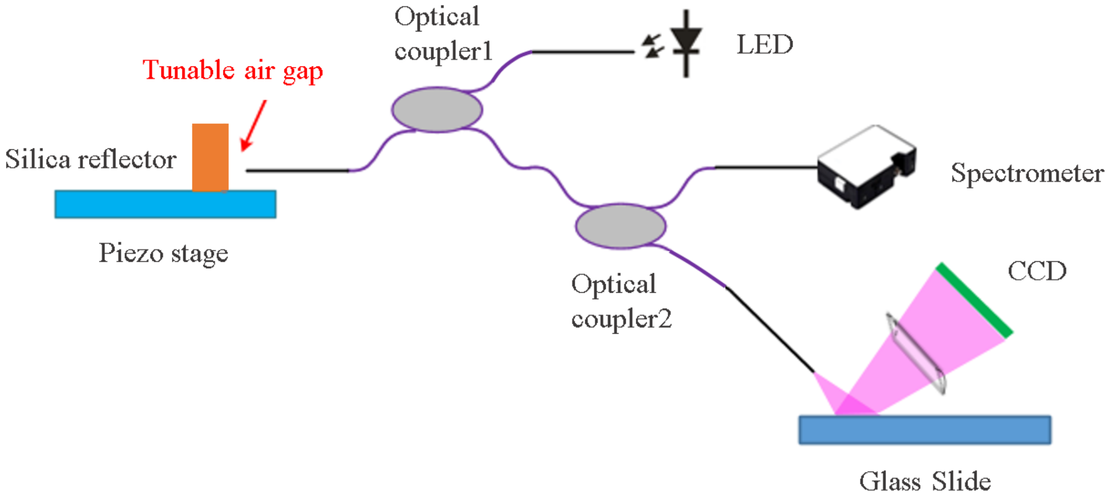

Figure 3-21 Wafer-based S-WLI interrogator works with single-mode fiber system, for demodulating a tunable air gap F-P.

The OPD vs. peak-pixel-index calibration curve is illustrated in Figure 3-22. The y-axis represents the OPDs calculated by the total phase WLI. The x-axis indicates the zero-order-peak index, calculated by the proposed S-WLI. The piezo stage was set at several steps. We took ten measurements at each step. However, the RMS of the piezo stage is ~15 nm. Thus, the OPDs at the set piezo-control voltage was not stable. They appeared to form a cluster of data points. However, all measured points still lay along the fitted curve; and shows a linear relationship between the WLI and the S-WLI method, which means the two algorithms match well with each other. In the next chapter, this new interrogation technology is applied to an actual sapphire wafer F-P temperature sensor. A solid wafer F-P cavity is more stable than an air gap for the performance investigation.

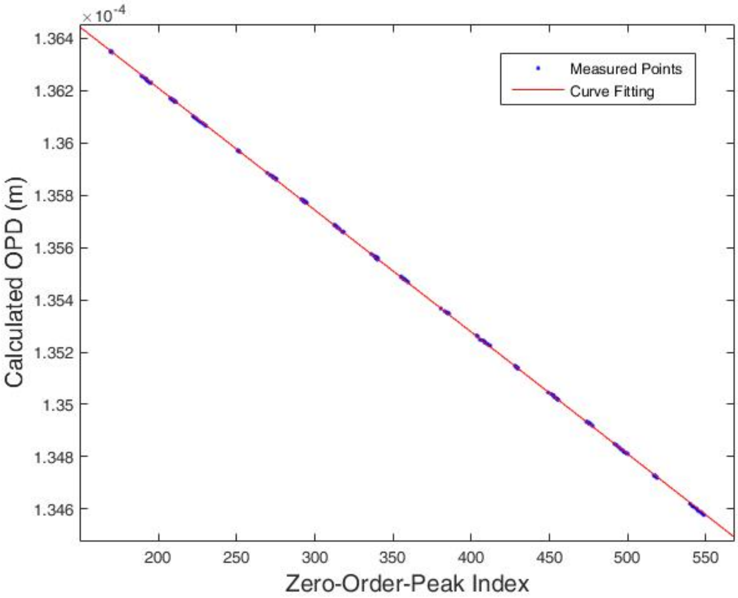

Figure 3-22 Calculated OPD vs. zero-order-peak index calibration curve in the multimode fiber system.

3.4 Challenges and Solutions

The challenges of the silica wafer Fabry-Perot S-WLI interrogator exist in several aspects, such as the dynamic range, the temperature compensation, and the quality of the optical interference signal.

First, as discussed in section 3.1, the OPD of the wafer interrogator must cover the full OPD variation of the target sensing F-P cavity. Limited by the size of the current 2-D image sensor, the OPD range of the wafer interrogator is approximate 5.5 μm, set at 45° fiber incidence. The small sized CCD sometimes prevents getting the full envelope of fringes. Therefore, one needs to estimate the OPDs of the sensing F-P in advance, to a very accurate level. Moreover, it requires a precise etching procedure to thin the wafer to the desired thickness for showing the zero-order fringe in the central area of the CCD camera. This issue can be dissolved by focusing the optical signal to a much longer 1-D CCD array. A low-cost silicon detector CCD array is commercially available. It can be as long as 3 cm, five times longer than the currently image sensor. Meanwhile, the system response will be much faster with a 1-D CCD array.

The thermo-optical and the thermal expansion effects influence the silica-wafer-based interrogator since the wafer OPD is temperature dependent. Therefore, this interrogator, in practice, needs to equip with a low-cost thermistor for temperature compensation.

It is noted that the silica wafer reflects only ~4% of optical power on each side, which leads to a significant insertion loss, and a reduction to the signal to noise ratio. For the future work, increasing the reflectivity of the silica wafer by depositing thin films on its surfaces is expected to be a direct and applicable optimization.

3.5 Conclusion

In this chapter, we introduce a novel and potential low-cost S-WLI interrogator for demodulating an F-P cavity at a low-cost. The interrogator includes only a piece of silica wafer and a CCD image sensor. With this setup, we simply deduce the optical length of an F-P cavity in the spatial domain by the pixel index of the CCD image sensor. With no moving parts and no expensive optical components, the new demodulation system is potentially stable and repeatable in the long term, and more importantly, low-cost.

3.6 Reference

1. Y. Zhu, and A. Wang, "Surface-mount sapphire interferometric temperature sensor," Applied optics **45**, 6071-6076 (2006).
2. S.-W. Kim, and G.-H. Kim, "Thickness-profile measurement of transparent thin-film layers by white-light scanning interferometry," Applied Optics **38**, 5968-5973 (1999).
3. S. Chen, A. Palmer, K. Grattan, and B. Meggitt, "Digital signal-processing techniques for electronically scanned optical-fiber white-light interferometry," Applied Optics **31**, 6003-6010 (1992).
4. F. Gao, R. K. Leach, J. Petzing, and J. M. Coupland, "Surface measurement errors using commercial scanning white light interferometers," Measurement Science and Technology **19**, 015303 (2007).
5. T. Li, A. Wang, K. Murphy, and R. Claus, "White-light scanning fiber Michelson interferometer for absolute position–distance measurement," Opt. Lett. **20**, 785-787 (1995).
6. K. G. Larkin, "Efficient nonlinear algorithm for envelope detection in white light interferometry," JOSA A **13**, 832-843 (1996).
7. P. Sandoz, "Wavelet transform as a processing tool in white-light interferometry," Opt. Lett. **22**, 1065-1067 (1997).
8. M.-C. Park, and S.-W. Kim, "Direct quadratic polynomial fitting for fringe peak detection of white light scanning interferograms," OPTICE **39**, 952-960 (2000).
9. I. V. Kassamakov, H. O. Seppänen, M. J. Oinonen, E. O. Hæggström, J. M. Österberg, J. P. Aaltonen, H. Saarikko, and Z. P. Radivojevic, "Scanning white light interferometry in quality control of single-point tape automated bonding," Microelectron Eng **84**, 114-123 (2007).

10. Y. J. Rao, and D. A. Jackson, "Improved synthesised source for white light interferometry," Electronics Letters **30**, 1440-1441 (1994).

11. A. Harasaki, J. Schmit, and J. C. Wyant, "Improved vertical-scanning interferometry," Applied optics **39**, 2107-2115 (2000).

12. S. Wang, T. Liu, J. Jiang, K. Liu, J. Yin, Z. Qin, and S. Zou, "Zero-fringe demodulation method based on location-dependent birefringence dispersion in polarized low-coherence interferometry," Opt. Lett. **39**, 1827-1830 (2014).

13. C. Belleville, and G. Duplain, "White-light interferometric multimode fiber-optic strain sensor," Opt. Lett. **18**, 78-80 (1993).

14. M. Fleischer, R. Windecker, and H. J. Tiziani, "Theoretical limits of scanning white-light interferometry signal evaluation algorithms," Applied optics **40**, 2815-2820 (2001).

15. K. Fazel, and S. Kaiser, *Multi-carrier Spread-spectrum: Proceedings from the 5th International Workshop, Oberpfaffenhofen, Germany, September 14-16, 2005* (Springer Science & Business Media, 2006).

16. J. Schmit, and A. Olszak, "High-precision shape measurement by white-light interferometry with real-time scanner error correction," Applied optics **41**, 5943-5950 (2002).

17. L. Deck, and P. De Groot, "High-speed noncontact profiler based on scanning white-light interferometry," Applied optics **33**, 7334-7338 (1994).

18. S. Chen, B. Meggitt, and A. Rogers, "Electronically scanned optical-fiber Young's white-light interferometer," Opt. Lett. **16**, 761-763 (1991).

19. A. Koch, and R. Ulrich, "Fiber-optic displacement sensor with 0.02 μm resolution by white-light interferometry," Sensors and Actuators A: Physical **25**, 201-207 (1990).

20. T. Bosselmann, and R. Ulrich, "High-accuracy position-sensing with fiber-coupled white-light interferometers," in *2nd Intl Conf on Optical Fiber Sensors: OFS'84*(International Society for Optics and Photonics1984), pp. 361-365.

21. Z. Li, J. Gong, B. Dong, C. Ma, J. Wang, and A. Wang, "Compact optical path scanner and its application for decoding fiber-optic interferometers," Opt. Lett. **35**, 1284-1286 (2010).

22. Z. Yu, Z. Tian, and A. Wang, "Simple interrogator for optical fiber-based white light Fabry–Perot interferometers," Opt. Lett. **42**, 727-730 (2017).

23. R. Azzam, "Phase shifts that accompany total internal reflection at a dielectric–dielectric interface," JOSA A **21**, 1559-1563 (2004).

CHAPTER 4 Low-Cost Sapphire Fiber Temperature Sensing System

4.1 Introduction

As discussed in Chapters 2 and 3, a low-cost sapphire-fiber-based Extrinsic Fabry-Perot Interferometer (EFPI) high-temperature sensing system can be built by using environmental thermal radiation as the broadband light source [1]. Also, the Optical Path Length (OPD) of an air gap Fabry-Perot cavity can be demodulated according to a new scanning white light interferometry (S-WLI) [2], using only a fused silica wafer and a low-cost CCD camera as the interrogator.

The application of thermal radiation to generate optical interference pattern avoids using an internal light source. Thermal radiation at high temperature offers broadband light as need, making the optical sensing system sourceless. Although thermal radiation spectrum changes with temperature [3, 4], the radiation background can be removed via filtering [5], when using white light interferometry for signal demodulation. The proposed S-WLI algorithm discussed in Chapter 3, uses only a piece of fused silica wafer and a 2-D CCD camera to translates the interference signal from the spectral to the spatial domain. The silica wafer, together with the CCD camera, functions as a tunable F-P interrogator. It tunes the reference OPDs by pointing an optical fiber at 45° to the double-side-polished fused silica wafer. Due to the light divergent nature of an optical fiber, the angle of incidence to the silica wafer has a distribution. Thus, the OPDs between the two surficial reflectors are angularly dependent. As a result, if a linear CCD is placed at an angle of 45° facing the fused silica wafer on the other side, a spatial distribution of the optical power indicates the OPD distribution of the silica-wafer interrogator.

Given the above two innovations, it is natural to construct a high-temperature fiber optic sensor system that combines the advantages of both designs.

In Chapter 3, the low-cost silica-wafer-based interrogator was preliminarily investigated via an air gap Fabry-Perot cavity. However, the stability of the air gap prevents further investigation. For a high-temperature sensor, a stable solid-wafer

Fabry-Perot cavity is preferred, because of its better thermal stability and corrosion resistivity, as well as the strain insensitive nature to avoid strain-temperature cross sensitivity [6]. In this chapter, we discuss in detail the novel low-cost optical sensor design, which uses the sapphire wafer F-P sensing cavity, together with the S-WLI demodulation algorithm.

4.2 Sapphire Wafer High-Temperature Sensor with 2-D CCD Design

4.2.1 Wafer-based Fabry-Perot interrogator

The schematic of the white light Fabry-Perot interrogator based on the S-WLI method is shown in Figure *4-1* [2].

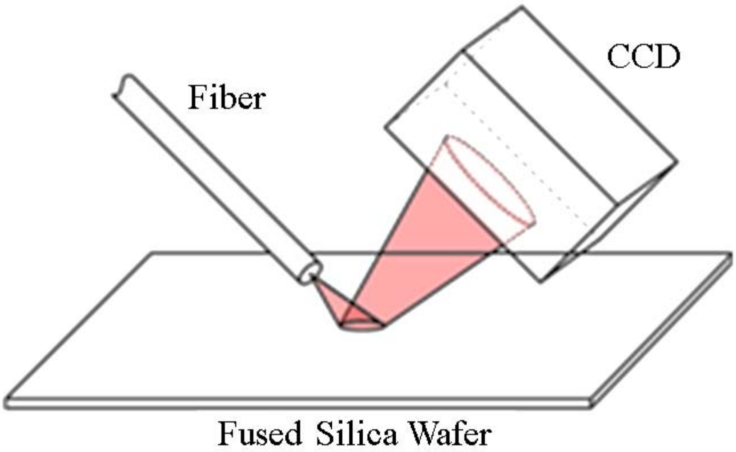

Figure 4-1 Schematic of the fused-silica-wafer-based interrogator. It includes a double-side-polished silica wafer and a 2-D CCD camera [2].

A simulation (*Figure 3-11*) gives that the reference OPD range covered by the 2/3” CCD sensor in this setup is approximately 5.5µm. Thus, it is crucial to make sure that, the actual sensing OPD must lie within this range. In practice, we roughly estimate the dynamic range of the sensing OPD in advance, and then polish or etch the fused silica wafer interrogator to the desired thickness to cover this range.

The sapphire-fiber temperature sensor uses a piece of the solid sapphire wafer as the temperature-sensing cavity. The wafer is 40μm thick at room temperature, which gives an initial OPD_0 as,

$$OPD_0 = 2n_0L_0 \tag{4.1}$$

At room temperature, the sapphire refractive index n_0 along c-axis equals 1.765 [7] at 850nm. The initial thickness L_0 equals 40μm. The average linear thermal expansion coefficient of sapphire (α) is ~7×10^{-6}/°C [8]; while the thermos-optical coefficient of sapphire α_T is ~8.2×10^{-6}/°C [9]. Hence, the OPD of the sapphire wafer, from room temperature T_0 to T, can be calculated as,

$$OPD_T = 2n_0[1+\alpha_T(T-T_0)]L_0[1+\alpha(T-T_0)] \tag{4.2}$$

Therefore, the total OPD change (ΔOPD) is,

$$\begin{aligned} \Delta OPD &= OPD_T - OPD_0 \\ &= 2n_0[1+\alpha_T(T-T_0)]L_0[1+\alpha(T-T_0)] - 2n_0L_0 \\ &= 2n_0L_0(\alpha_T+\alpha)(T-T_0) + 2n_0L_0\alpha_T\alpha(T-T_0)^2 \\ &\approx 2n_0L_0(\alpha_T+\alpha)(T-T_0) \end{aligned} \tag{4.3}$$

In the third line, the multiplication of α_T and α is too small, compared to the other terms. Thus, the term $2n_0L_0\alpha_T\alpha(T-T_0)^2$ is negligible. When T and T_0 are set to 1600°C and 25°C, respectively, the ΔOPD is calculated ~3.4μm. It is much smaller than the 5.5μm of the reference OPD range. Therefore, the wafer based interrogator is intended to work with a specifically sapphire wafer Fabry-Perot high-temperature sensor.

4.2.2 Optical System Design

We built a benchtop sapphire fiber F-P temperature sensor to investigate the performance of the proposed interrogator. The cavity being measured was a sapphire-wafer Extrinsic Fabry-Perot Interferometer. It had a sapphire fiber functioning as the lead-in fiber, aligned to the sapphire wafer perpendicularly, as described in [10]. The thickness of the fused-silica wafer was carefully designed according to Equation (3.20) . The silica wafer was etched in 50% HF solution at high speed (~1.5μm/min), and then in a buffer HF solution at a lower rate (1~2 nm/min) to reach the desired thickness. A broadband LED, centered at 850 nm, was used as the light source. We installed a 2/3" 2D CCD camera (Stingray F145B, Allied Vision) with no IR filter as the detector. The multi-mode fiber (105/125) was used to connect all components. Although using a multimode fiber instead of a single-mode fiber leads to a reduction of signal contrast [11], it couples significantly stronger light power into the optical system. At the same time, the larger diverge angle also expands the OPD measurement range of the interrogator.

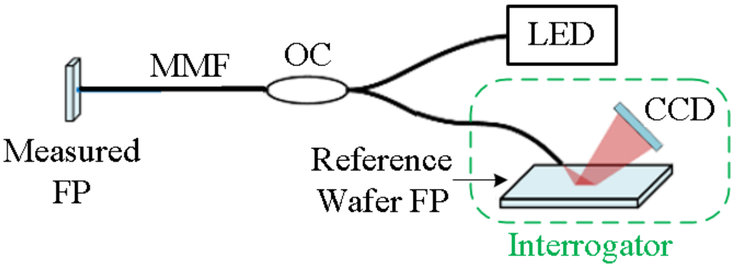

Figure 4-2 optical system for wafer-based S-WLI interrogator investigation.

4.2.3 Experimental Setup for Wafer-Based F-P Interrogator

Figure *4-3* (a) and (b) show a demonstration setup of the silica-wafer-based interrogator. The interrogator is simply constructed by a multimode bare fiber pointing at 45° to a piece of etched fused silica wafer. The multimode fiber is finely polished. The lens in front of the camera has been removed. A 2-D image sensor collects the optical power. The bare image sensor exposes in the air at 45° facing the fused silica wafer.

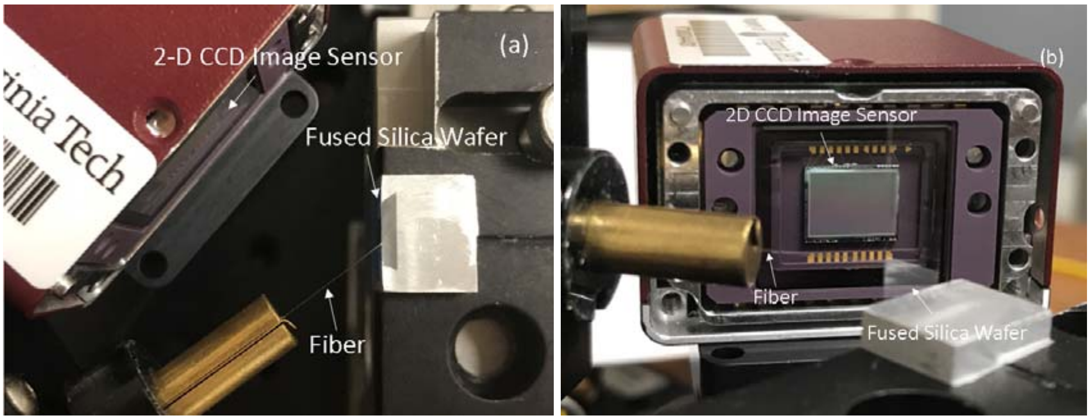

Figure 4-3 Experimental setups for the silica-wafer-based Fabry-Perot interrogator.

4.2.4 Optical Background Treatment

During the signal demodulation, we collect the DC background in the first step. In fact, the two sides of the wafer may not be perfectly parallel and flat over a large area. Luckily, in the setup shown in Figure *4-2*, only a small area of the wafer is used as the reflector, which significantly lowers its quality requirement. By placing the fiber tip at 300µm from the wafer, the light exposure region is as small as <500µm in diameter. Even there are inevitable surface imperfections within this active region; they will only lead to slight distortion on the 2-D raw signal, which can be removed by the background subtraction process.

The DC background was obtained before assembling the sapphire wafer F-P sensing cavity. In this case, only the reflection from the sapphire fiber tip was collected. Figure *4-4* (a) and (b) illustrates a typical background signal indicated by the camera. Without a sensing F-P cavity, no interference pattern was observed. The intensity distribution of the background is determined by the light divergence of the multimode fiber, which is a 2-D Gaussian shape. Carefully adjusting the camera position, we were able to get a clear Gaussian beam located in the center of the camera. Contaminations and damages on the CCD pixels and the surface of the etched fused silica wafer, or on the polished multimode fiber induce visible spots on the background, circled in Figure *4-4* (a). Besides, imperfect surficial conditions, such as non-flatness and scratches, on the etched silica wafer or the polished fiber tip would cause distortions on the background. Background signal along Row 550 is illustrated in Figure *4-4* (b). Small ripples are observed. Given the observation, recording the background signal is essential. It will be used to normalize the actual optical signal.

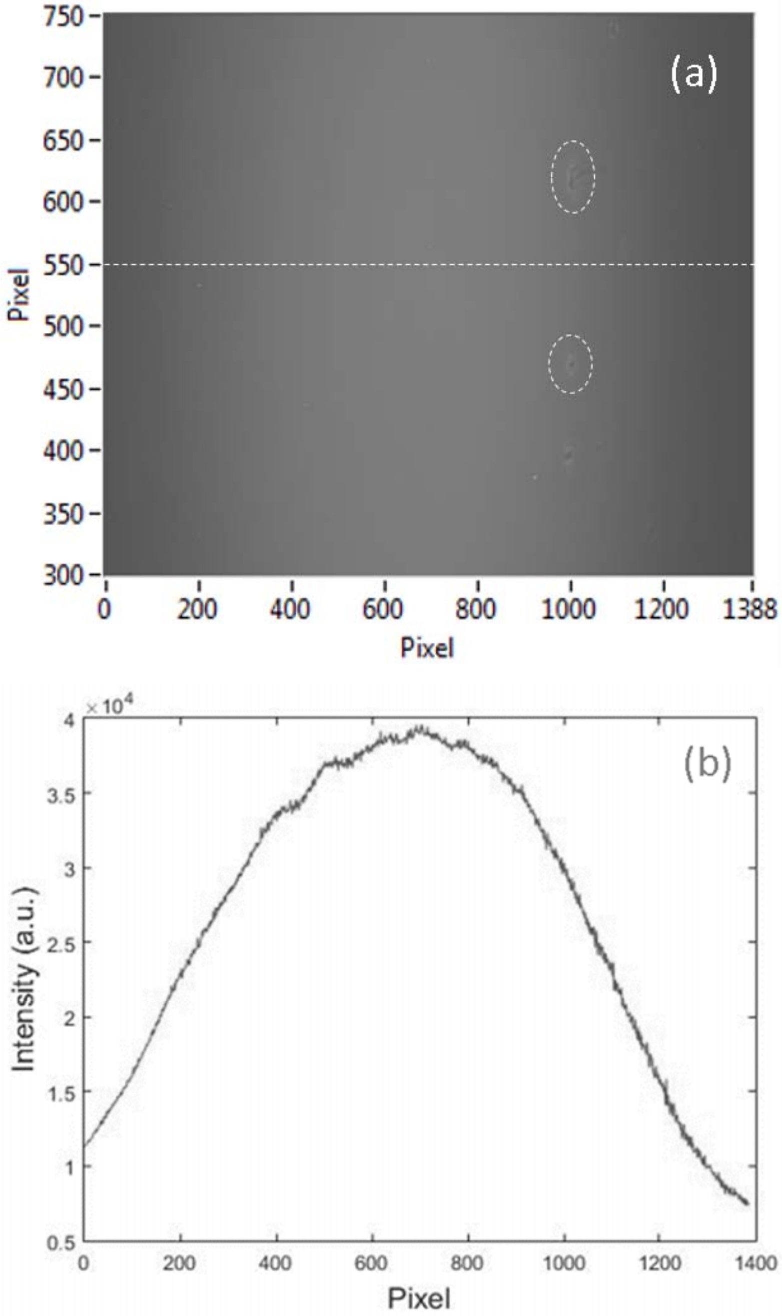

Figure 4-4. Optical background without a sensor head shown in the 2-D camera (a) and the intensity along Row 550 (b) [2].

An interference pattern was observed after installing the sapphire wafer sensing F-P. Figure *4-5* (a) and (b) illustrates a typical interference pattern before removing the background. Figure *4-5* (a) shows the image of the entire camera, while Figure *4-5* (b) shows the signal along Row 550. The interference signal appears as a superposition over the background. According to Figure *4-5* (b), the DC background equals approximately 0.975. Thus, the fringe contrast of Figure *4-5* (b) curve is calculated to be ~0.046. The contamination spots, which are circled in Figure *4-4* (a), are still visible.

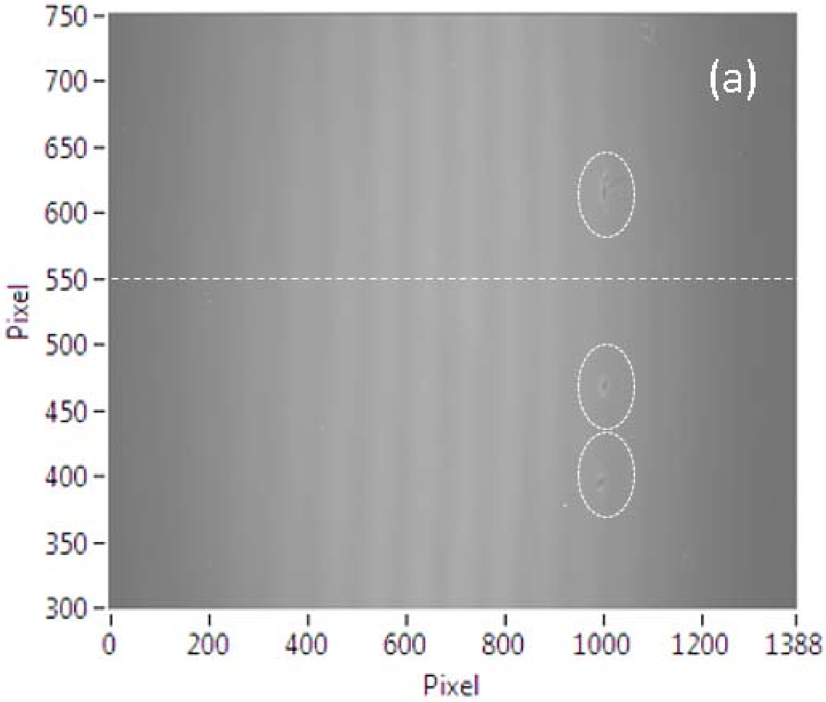

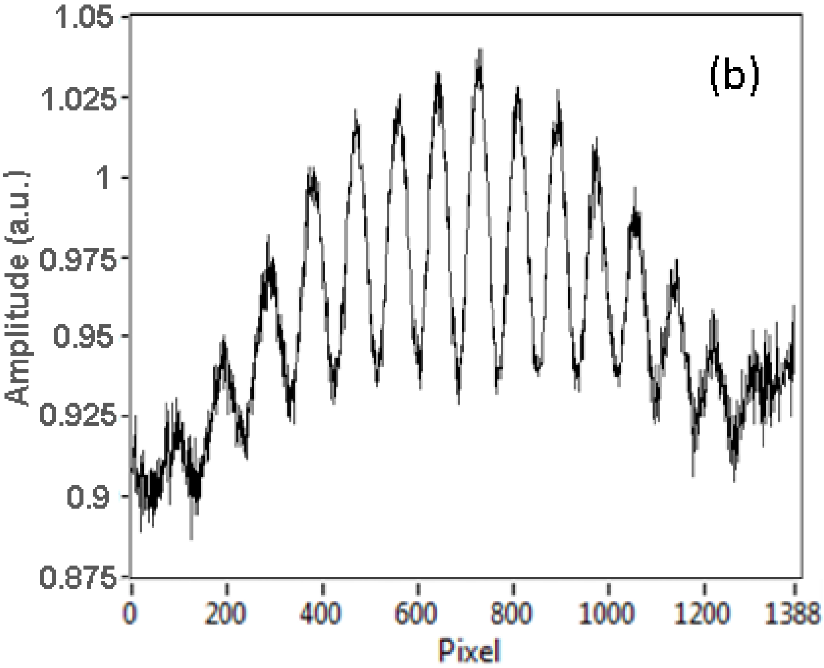

Figure 4-5 The 2-D S-WLI interference pattern before removing the background (a) [2], and the intensity along Row550 (b).

Figure *4-6* (a) and (b) [2] illustrates the interference fringe after the background is removed. Figure *4-6* (b) shows the fringe pattern along Row 550. As a comparison, the fringe contrast without the background is calculated to be ~ 0.048. It is similar to the value calculated with the background. The result fits the analysis in Equation (3.35), the fringe contrast of the entire optical system, with two F-Ps connected in series, will be determined by the fringe contrast of both F-Ps. Background removal procedue does not improve the fringe contrast. However, the DC component is flattened as expected. The peak envelop is clear for signal demodulation.

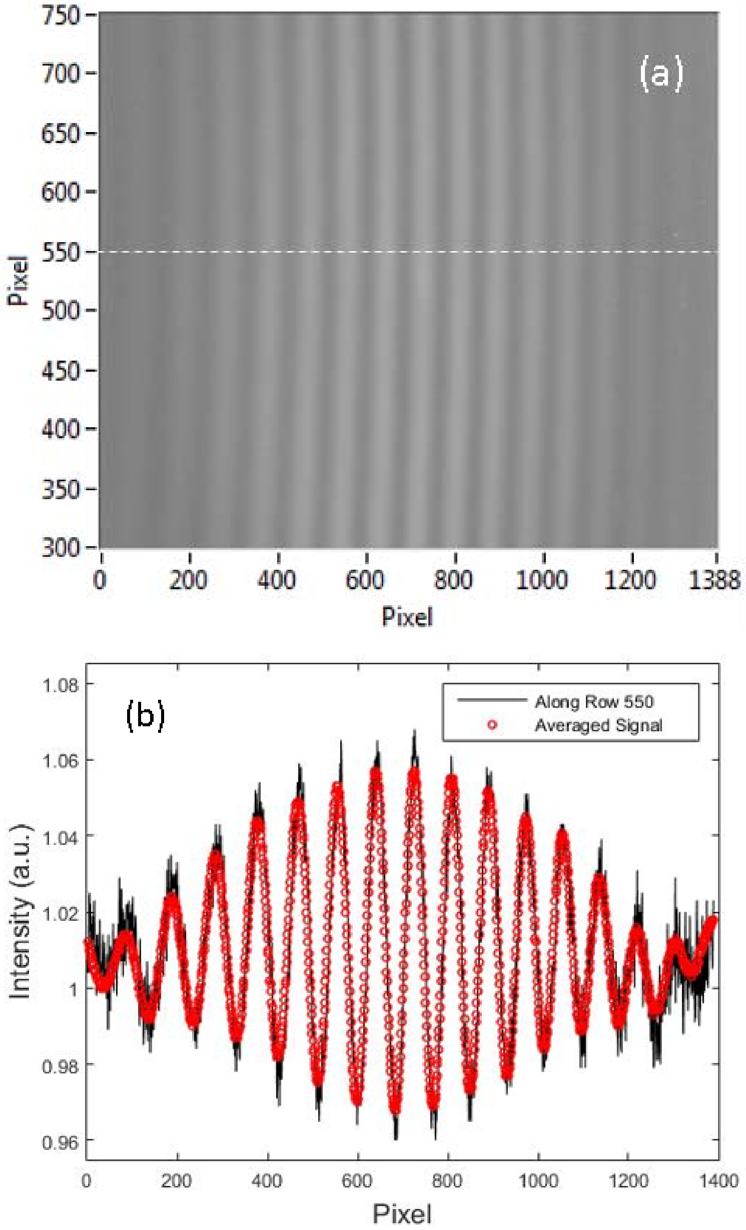

Figure 4-6 The 2-D S-WLI interference pattern after removing the background (a), and along Row 550 (b) [2].

In the experimental setup, the distance between the CCD camera and the wafer interrogator was made adjustable to collect the most of the diverging optical power. Given the rotational symmetry of the configuration, a slightly curved pattern appeared on the 2-D image (Figure *4-6* (a)). Compared to the size of the CCD sensor, the distortion is negligible. All the rows in the horizontal direction show interference fringes. The fringes were then averaged along the vertical direction to convert the 2-D raw data into a 1-D data, indicated by the red points of Figure *4-6* (b). By averaging all the rows, the signal-to-noise ratio improves significantly. It is noticed that the signal quality at the edge of the 2-D image is relatively poor due to the weaker light intensity, which can be observed from Figure *4-4* (b) and Figure *4-5* (b). It is a result of the Gaussian power distribution of the multimode fiber. Therefore, during the signal demodulation, borders of 200 pixels wide on all sides were excluded from the further calculation.

4.2.5 Signal Demodulation

A two-step signal demodulation algorithm was developed for the silica-wafer-based S-WLI, given by the averaged date shown in Figure *4-6* (b). In the first step, all local maximum and minimum points are found in the 1-D averaged signal (Figure *4-6* (b)). The two envelopes of this 1-D signal are obtained by the second-order polynomial curve fitting, according to all peaks and valleys, respectively. The pixel index at the maximum gap between the two envelopes curves is found, which coarsely indicates the location of the zero-order fringe. In the second step, the peak closest to the estimated center obtained in the first step is selected, indicated by the red triangles in Figure *4-7* (a) and (b). It is named as the zero-order fringe, according to the S-WLI algorithm. Its position represents the sensing OPD by a one-to-one projection function, discussed in Chapter 3.

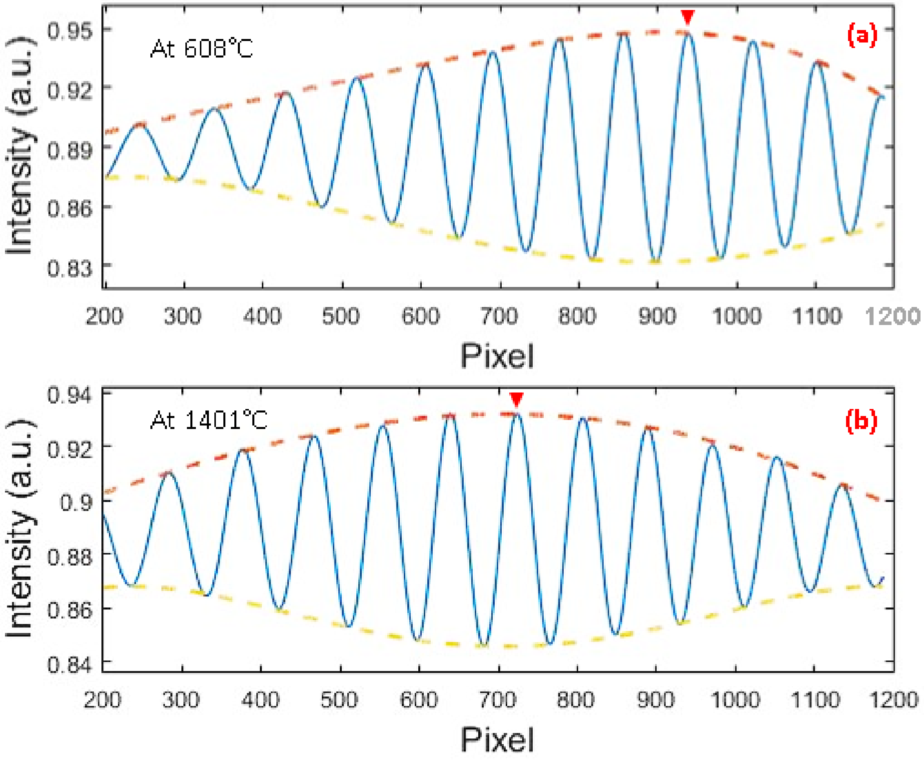

Figure 4-7 The Fitted envelopes for the fringe patterns obtained at (a) 608°C and (b) 1401°C, respectively. The zero-order peaks are marked by the red triangles [2].

Figure 4-7 shows the fringe signals obtained at 608°C (a) and 1401°C (b), respectively. When the sensor was heated, the OPD of the sapphire wafer cavity increases due to the thermo-optical effect induced refractive index enlarge and the thermal expansion, leading to a larger OPD and a shift of the entire fringe. The zero-order fringe, which is indicated by the maximum peak, shifts as expected.

4.2.6 Sapphire wafer F-P Temperature Sensor with S-WLI interrogator

An optical system was built to investigate the wafer-based interrogator. The schematic of the setup is shown in Figure *4-8*. A sapphire-wafer-based external Fabry-Perot interferometer sensor head functions as the temperature sensor. The sensor head is fabricated according to [12]. A spectrometer (Ocean Optics, USB2000) was connected in the system to record the full interferometric spectra and calculate the Fabry-Perot cavity length of the sapphire wafer using the well-known WLI method as a reference.

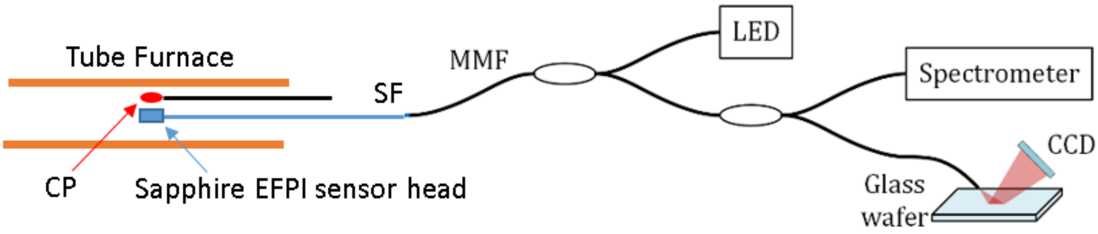

Figure 4-8 Experimental setup for temperature sensor investigation.

The sapphire wafer F-P sensor head was heated in a tube furnace (GSL1500X, MTI Corp.). A B-type thermocouple placed near the sensor head to record the actual temperature. The temperature rose from 600°C to 1400°C at approximately 100°C intervals. With the signal demodulation algorithm introduced in the previous section, an OPD vs. zero-order pixel curve was obtained (Figure *4-9*). The OPDs on the vertical axis was calculated by the WLI method [13]. The zero-order fringe position value for the horizontal axis was calculated by S-WLI algorithm developed in this work. The simulation result shown in *Figure 3-12* predicts a linear OPD distribution along the CCD image sensor. It is proved in the actual investigation.

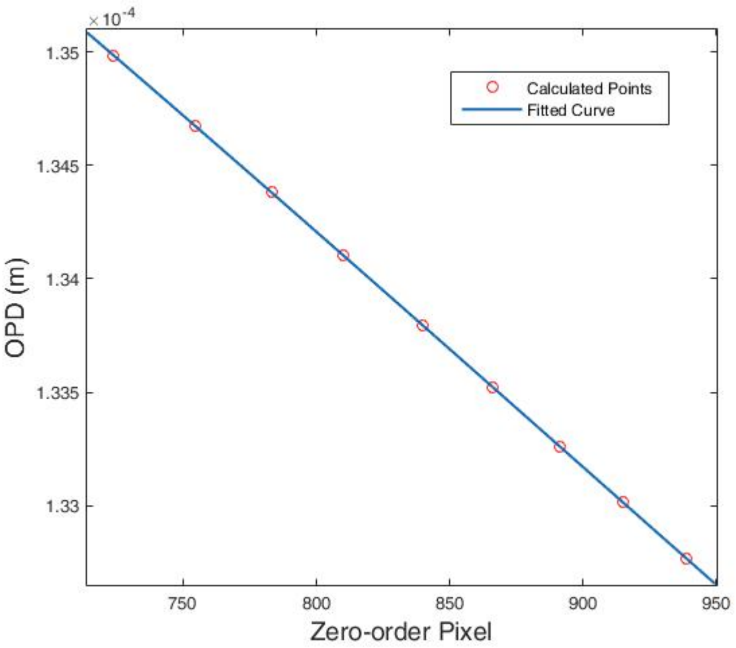

Figure 4-9 OPD vs. zero-order pixel index calibration curve obtained by WLI (for OPD) and S-WLI (for pixel index) method [2].

4.2.7 Temperature Resolution

In the thermal test, twenty measurements were performed at each temperature step. The standard deviations (SDs) of OPD (σ_{WLI}) and pixel index (σ_{Pixel}) were calculated. They relate to each other via,

$$\sigma_{S-WLI} = |\frac{dOPD}{dPixel}|\sigma_{Pixel} \tag{4.4}$$

$dOPD / dPixel$ is the slope of the calibration curve shown in Figure *4-9*. Comparisons between the WLI and S-WLI methods are listed in Table *4-1*, in which σ_{WLI} and σ_{S-WLI} show close values for different temperatures. Thus, the proposed S-WLI algorithm is expected of have similar accuracy as the traditional WLI method. The larger σ_{Pixel} at high temperatures is a result of temperature fluctuation in the furnace. Larger σ_{WLI} appears in the traditional WLI demodulation as well. By using the σ_{Pixel} values at a lower temperature as the indicator of the system resolution, the dynamic range of the system can be estimated to be about 10^5 [2]. It is not as high as a spectrometer-based WLI interrogation due to its limited measurement range but still sufficient for most interrogation applications of wafer-based Fabry-Perot sensors.

Table 4-1 OPD standard deviation comparisons between WLI and S-WLI methods [2].

Temperature [°C]	σ_{WLI} [μm]	σ_{S-WLI} [μm]	σ_{Pixel}
608.6	5.20E-5	7.37E-5	0.0071
705.1	8.43E-5	7.07E-5	0.0068
800.1	5.31E-5	4.16E-5	0.0040
898.5	8.21E-5	9.04E-5	0.0087
997.0	1.22E-4	1.53E-4	0.0148
1106.3	3.71E-4	3.25E-4	0.0315
1200.5	2.52E-4	3.06E-4	0.0298
1300.6	6.33E-4	9.13E-4	0.0894
1401.9	7.65E-4	1.17E-3	0.1157

Figure *4-10* illustrates the temperature vs. Pixel index curve.

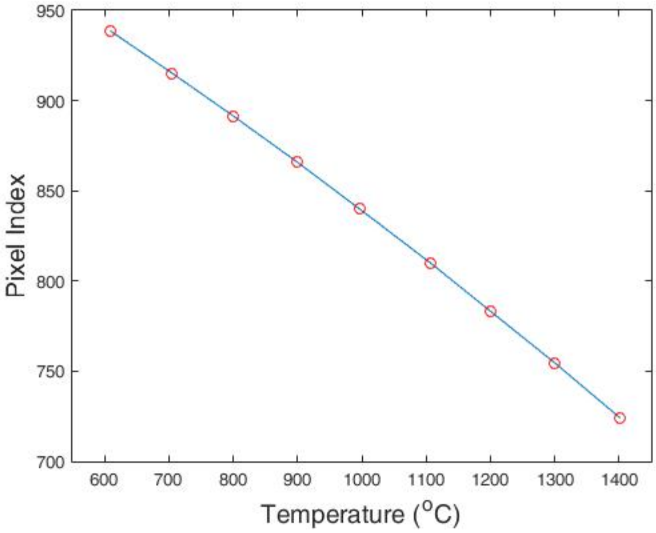

Figure 4-10 Temperature vs. pixel index calibration curve.

As a temperature sensor, we defined the temperature resolution by the standard deviation of the system. According to the S-WLI algorithm, it is calculated as,

$$\sigma_T = \left| \frac{dT}{dPixel} \right| \sigma_{Pixel} \tag{4.5}$$

where $dPixel / dT$ is the slope of the temperature vs. pixel index curve, illustrated in Figure *4-10*. Table *4-2* lists the standard deviations at different temperature levels. In industry, the temperature resolution is usually defined as $2\sigma_T$ or $4\sigma_T$. Thus, according to the test result, the silica-wafer-based S-WLI interrogator achieves temperature resolution of about and better than 1ºC, which is enough for most industrial applications.

Table 4-2 List of standard deviations at different test temperatures.

Temperature [°C]	σ_{Pixel}	σ_T (ºC)
608.6	0.0071	0.026
705.1	0.0068	0.025
800.1	0.0040	0.015
898.5	0.0087	0.032
997.0	0.0148	0.055
1106.3	0.0315	0.116
1200.5	0.0298	0.110
1300.6	0.0894	0.330
1401.9	0.1157	0.427

4.3 Sapphire Wafer High-Temperature Sensor with Focused Light Interrogator

Given the geometry of an optical fiber, light reflected from the silica-wafer F-P interrogator spatially distributes in an area. Therefore, a 2-D CCD camera was installed to collect the power distribution. While using an external LED as the broadband source, light exposure to a single image sensing pixel is high enough to generate a good signal. However, for the situations where light exposure is extremely weak, such as using thermal radiation as the light source [1], a much longer exposure time is needed to enhance the signals until they are strong enough for demodulation. In this case, focusing light to fewer imaging pixels helps reduce the exposure time, and improve the signal-to-noise ratio. This section discusses a design that uses a cylindrical lens to enhance the sensor performance under weak radiation exposure.

4.3.1 Wafer-Based Focused-Light Fabry-Perot Interrogator

The focused-light interrogator is illustrated in Figure *4-11*. It is similar to Figure *4-1*. Instead of using a 2-D CCD only, a cylindrical lens (f = 20mm, L = 25mm, D = 15mm) is mounted in between the fused silica wafer and the camera. It focuses the diverged light to only a few lines on the CCD to increase the signal-noise-ratio, and help shorten the light exposure. As shown in Figure *4-6*, the optical signal displays a vertical interference pattern. The cylindrical lens must be mounted perpendicularly to the fringe. Essentially, it functions as a signal averaging process along the vertical direction.

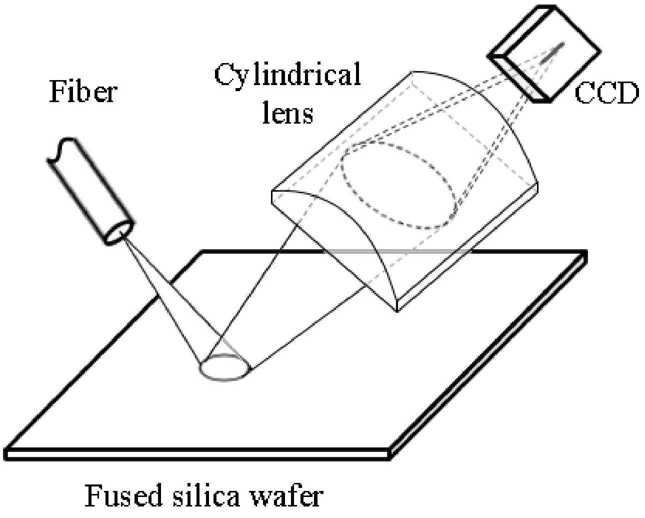

Figure 4-11 Focused light silica-wafer interrogator.

Figure *4-12* shows the actual optical setup for the preliminary test. A fiber points to a polished and etched fused silica wafer at 45°; the cylindrical lens focuses the reflected light from the silica wafer to a 2-D CCD camera (Stingray F145B, Allied Vision). The lens of the camera has been removed, leaving the 2-D image sensor exposed to the air without any filter on top of the sensing pixels. We name this structure the focused-light Fabry-Perot interrogator.

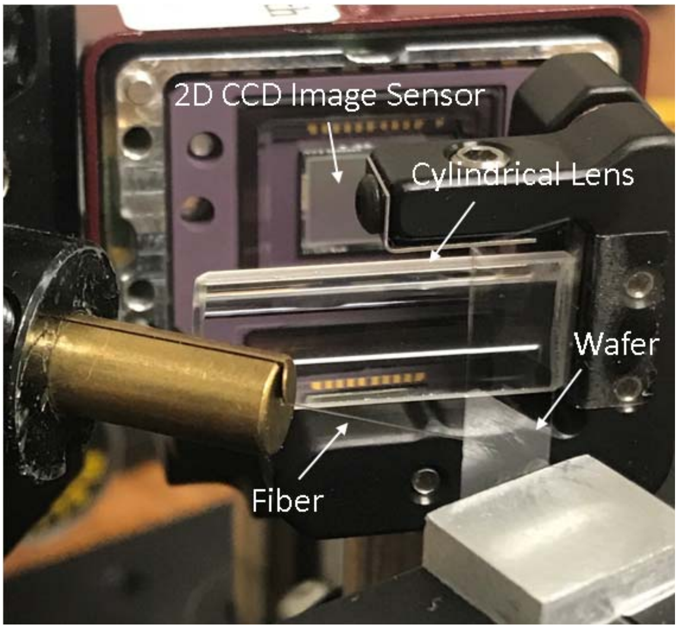

Figure 4-12 Experimental setups of the focused-light Fabry-Perot interrogator.

The optical evaluation system was built like Figure *4-13*. Similar to Figure *4-2*; an LED was used in the preliminary test to provide a strong exposure to the CCD sensors for getting a better evaluation. The interferometric optical signal reflected from the sapphire wafer F-P sensing cavity propagates through an optical coupler and then launches to the new interrogator. We used the same 2-D CCD camera (Stingray F145B, Allied Vision) to acquire optical power.

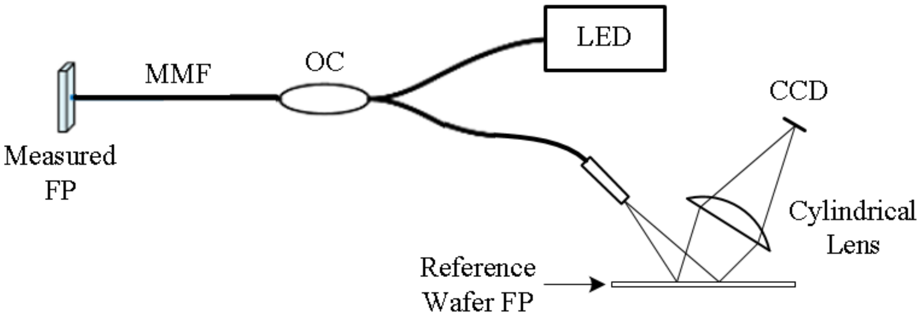

Figure 4-13 Optical design for focused light silica wafer Fabry-Perot interrogator.

4.3.2 Optical Signal Acquisition

The optical system constructed like Figure *4-13* was investigated with a LED light source. A regular 105/125 multimode fiber (MMF) guided the optical signal to the interrogator. The focused background signal was recorded (Figure *4-14*.) before installing the sapphire wafer F-P sensing cavity. Only several central lines on the CCD received the optical signals.

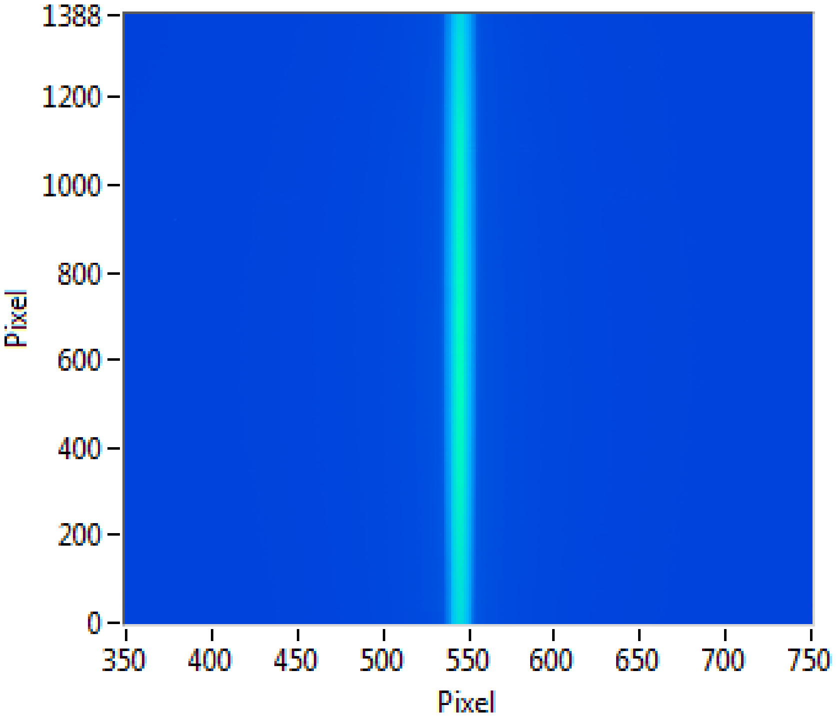

Figure 4-14 background signal of the focused light F-P interrogator.

Figure *4-15* plots the background intensity along Line 545, which is the center of the focused region. Similar to the 2-D background without focusing (Figure *4-4*), the optical signal along line 545 is not smooth, showing small ripples. They are a result of the imperfect surface conditions on the fused silica wafer or the multimode fiber; and the contaminations on some areas of the image sensor. Although focusing light to fewer lines can be considered as an averaging process to reduce the random noise, it does not eliminate the above issues. Thus, the background has to be recorded for signal demodulation.

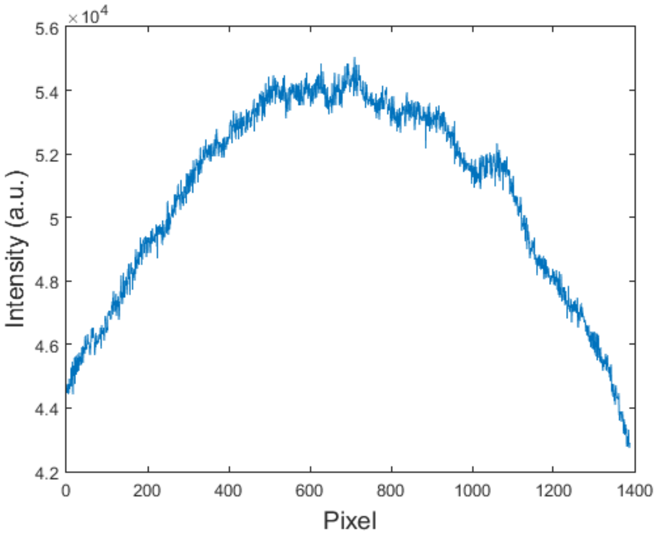

Figure 4-15 Background signal along Line 545.

After installing the sapphire wafer F-P cavity, a clear interference pattern was observed over the background signals. Figure *4-16* is an enlarged image of Figure *4-14* from Line 525 to Line 565. The fringe pattern occupies around 20 lines of the CCD camera, which centers at Line 545. Given the 4.7µm×4.7µm pixel size, the cylindrical lens focus light to approximately 100 µm, which is about the core diameter of the multimode fiber.

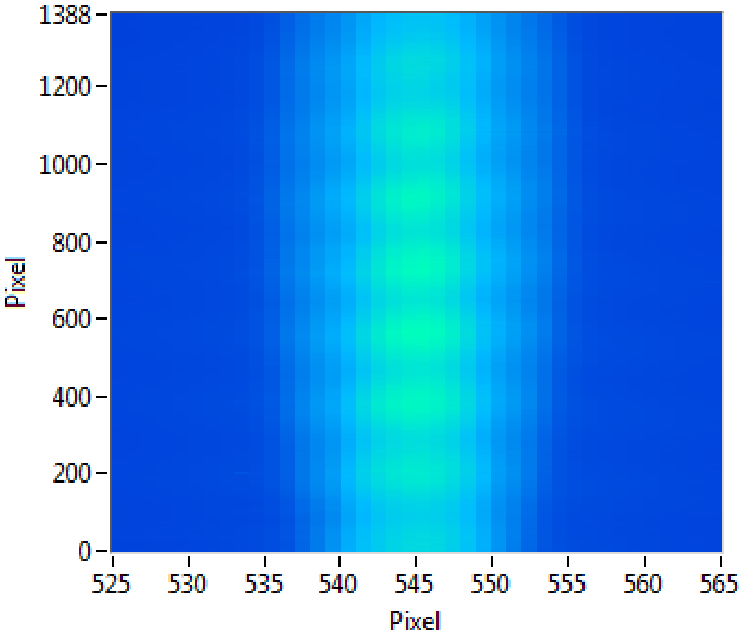

Figure 4-16 Optical signals focused on the 2D CCD.

Figure *4-17* (a) and (b) illustrate the signal along Line 545, before and after removing the background, respectively. Similarly, the intensity is low at the very edge of the image sensor. Therefore, 200 points at both ends of the fringe pattern are not included in the signal demodulation.

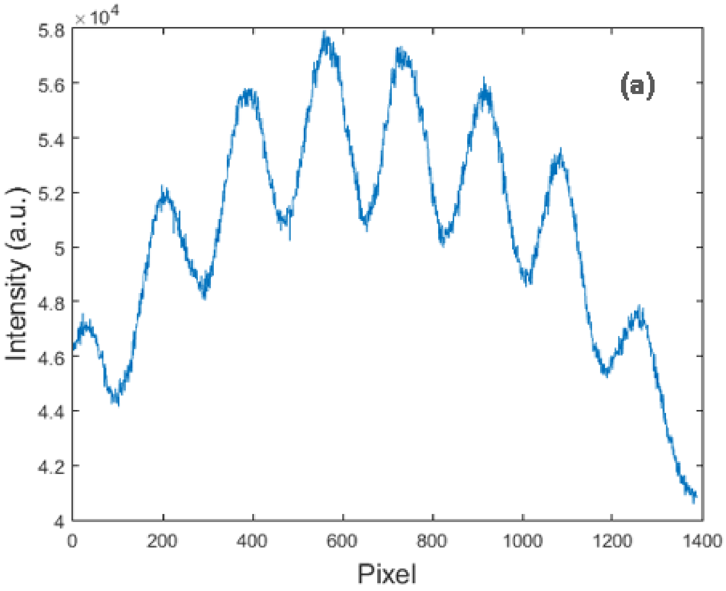

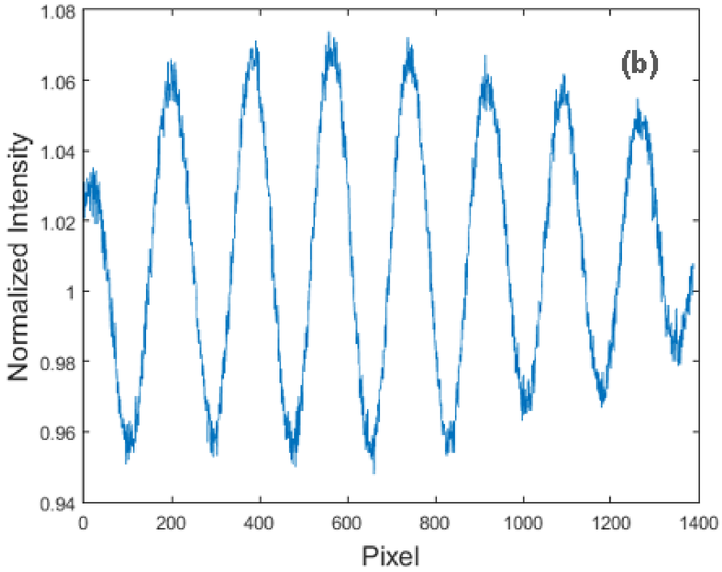

Figure 4-17 The interferometric signal along Line 545 with a sensor head installed, before (a) and after (b) removing the background.

4.3.3 Signal Demodulation of the Focused Light Wafer Interrogator

The signal demodulation procedure is similar to what is described in Chapter 4.2. According to the actual CCD recording, only twenty lines, which center at Line 545, are valid. Signals of these lines are averaged and then smoothed via a low pass digital filtering. In Figure *4-18*, a second-order polynomial function is applied to fit the local maximum and minimum points separately. Thus, two envelops are obtained, displayed as the red and yellow curve in Figure *4-18*. The Zero-order fringe, defined by the S-WLI algorithm, is determined by the greatest gap between the two envelops [2]. It is the peak which is nearest to the largest gap position, marked by the purple arrow in Figure *4-18*. When the optical length of the sapphire wafer F-P changes, the position of the zero-order fringe shifts accordingly.

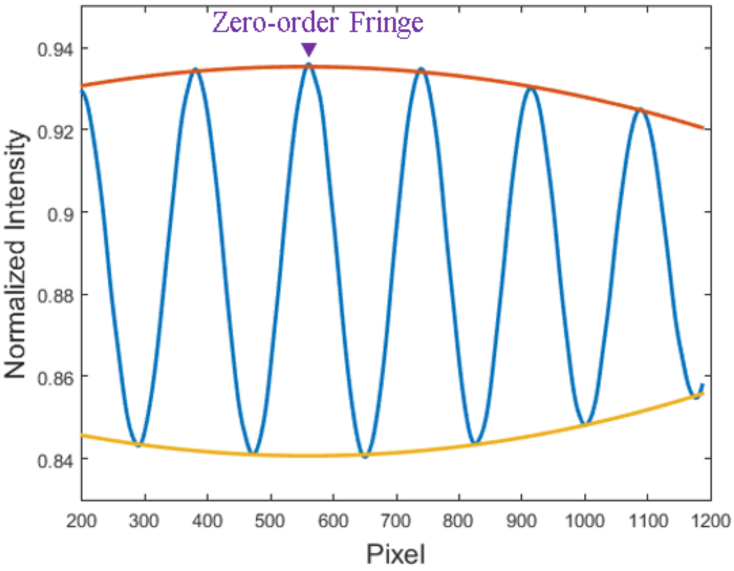

Figure 4-18 Zero-order fringe determined by the curve fitting.

Comparing between *Figure 4-18* and Figure *4-6*, the interference pattern obtained by the focused light methodology shows fewer peaks. It is a result of the long distance between the fused silica wafer and the image sensor. Theoretically, this helps improve the spatial resolution. However, it is noticed that the longer distance means a smaller solid angle, and further, a reduction of the dynamic range. One needs to consider this change before constructing the optical system with simulation, and then choosing the proper cylindrical lens and CCD.

4.3.4 Signal-to-Noise Ratio

Focusing light from a 2-D area to fewer lines of the CCD camera help increase the signal-to-noise ratio. The noise of a CCD image sensor is positively related to the light exposure, or “integration time”. To simplify the analysis, we roughly assume that optical power distributes uniformly across the entire CCD, which is valid, especially in the central region of the camera. When a given total power I_0 uniformly spreads over K lines, each line records a signal power of,

$$I_S = \frac{I_0}{K} \tag{4.6}$$

Under a fixed exposure, a stable noise (I_N) will be obtained. The SNR of a single line can be expressed as,

$$SNR \sim \frac{I_S}{I_N} = \frac{I_0}{KI_N} \tag{4.7}$$

When signals of all K lines are averaged, the SNR improves by a factor of $\sqrt{K}$, which gives the signal-to-noise ratio proportional to,

$$SNR \sim \frac{I_0}{I_N\sqrt{K}} \tag{4.8}$$

The above equation proves the concept that focusing light to fewer lines generates a better SNR under the given light exposure. In our case, the cylindrical lens focuses the reflected light from 1388 lines to only 20 lines, which, theoretically, enhances the SNR by approximately eight times.

4.3.5 Temperature Sensor Performance with LED

The performance of the Focused-light Fabry-Perot interrogator was investigated by demodulating the sapphire wafer F-P temperature sensor. The test system was constructed like Figure *4-19*. Similar to Figure *4-8*, a spectrometer (Ocean Optics USB2000) was included in the system. A PC recorded the full spectrum and calculated sapphire wafer OPD via WLI method [16] as the comparison. A thermocouple was installed with the sensor head for temperature reference. The thermocouple, the F-P interrogator, and the spectrometer were acquiring data simultaneously.

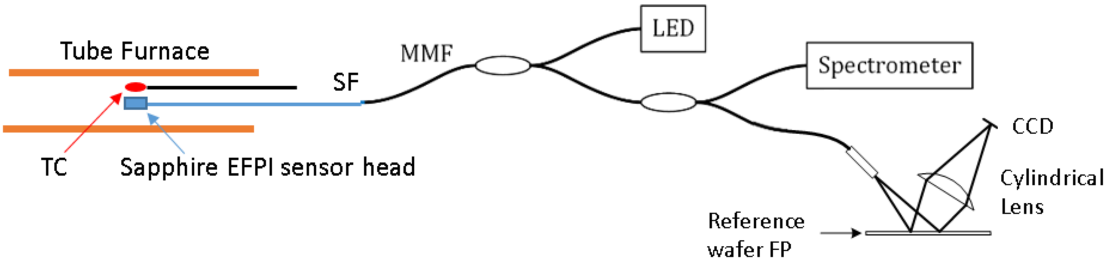

Figure 4-19 Evaluation system for the focused light Fabry-Perot interrogator.

We tested the system at several temperatures from 500°C up to 1400°C at 100°C each step. 20 samples were recorded at each temperature level. *Figure 4-20* illustrates two calibration curves, the pixel position (calculated by S-WLI) vs. temperature calibration curve and the OPD (calculated by full-spectrum WLI) vs. temperature calibration curve, respectively. The points on the calibration curves are the mean value of the samples. Both curves include error bars at each set temperature. However, the error bar is too small to be observed clearly. Therefore, their values are listed in Table 4-3 as well, in Column 4 and 5. According to the calibration curve, the temperature-dependent zero-order peak pixel index (P_{Index}) and OPD (calculated by spectrometer WLI method) are described by the second-order polynomial functions.

For the S-WLI method,

$$P_{Index} = -7.47\times10^{-5}T^2 - 0.4263T + 1.2000\times10^3 \tag{4.9}$$

For the full-spectrum WLI method,

$$OPD = 3.80\times10^{-13}T^2 - 1.989\times10^{-9}T + 1.31432\times10^{-4} \tag{4.10}$$

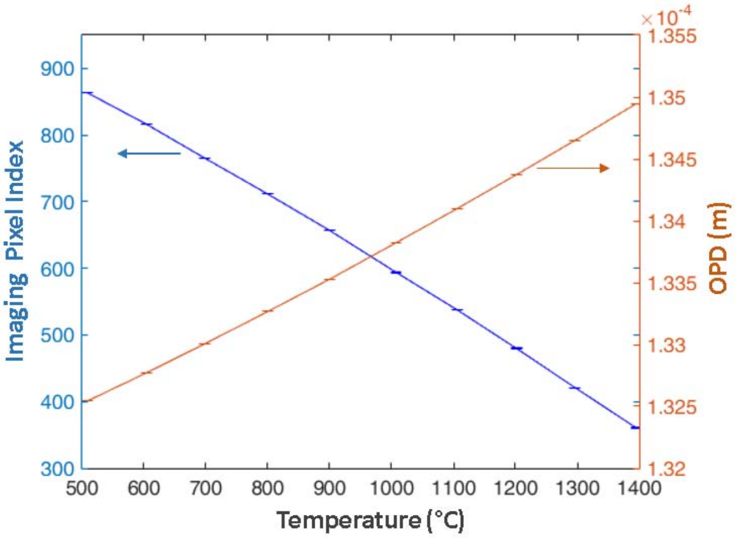

Figure 4-20 Temperature calibration curves of S-WLI and WLI methods.

Given the above two equations, together with the thermocouple readings, we have three sets of temperature values. One of them is directly obtained from the thermocouple, noted as T. Its standard deviation is denoted as σT. Another set of temperature values are calculated from the S-WLI calibration curve described by Equation 4.9. Once the Zero-order peak position is obtained, Equation 4.9 can calculate the indicated temperature. Since we have 20 measurements at a set temperature, the standard deviation of the Zero-order peak position (σ_{Pixel}) is obtained. Therefore, the indicated temperatures has a standard deviation as well, noted as σT_{S-WLI}. σT_{S-WLI} can be calculated according to,

$$\sigma T_{S-WLI} = \left|\frac{dT}{dPixel}\right| \sigma_{Pixel} \tag{4.11}$$

$\frac{dT}{dPixel}$ represents the slop of the Zero-order pixel position vs. temperature calibration curve.

Similarly, a set of temperature value can be calculated from the OPD vs. temperature calibration curve. Once the OPD was obtained from the optical spectra recorded by the spectrometer, Equation 4.10 can calculate the indicated temperatures. Since we acquired 20 optical spectra at each set temperature, the standard deviation of OPD (

σ_{OPD}) is obtained. Therefore, the indicated temperatures has a standard deviation, noted as σT_{WLI}, which can be calculated according to,

$$\sigma T_{WLI} = \left| \frac{dT}{dOPD} \right| \sigma_{OPD} \tag{4.12}$$

$\frac{dT}{dOPD}$ represents the slop of the OPD vs. temperature calibration curve.

Now we have three sets of temperature standard deviations as well, σT, $\sigma T_{S\text{-}WLI}$ and σT_{WLI}. The first one (σT) can be calculated from the thermocouple reading, the second ($\sigma T_{S\text{-}WLI}$) and the third (σT_{WLI}) one denote the standard deviation of temperature, calculated by the S-WLI and WLI methods, respectively. Figure shows three standard deviations that are obtained from thermocouple, S-WLI and WLI method, respectively. As mentioned in Chapter 2.4.5, Limited by the display digits, using the temperature readings from the thermocouple as temperature reference at higher than 1000ºC will leads to a larger error bar. However, as temperature cools down, the furnace would provide a better control to the thermal environment, which can be observed from the thermocouple readings.

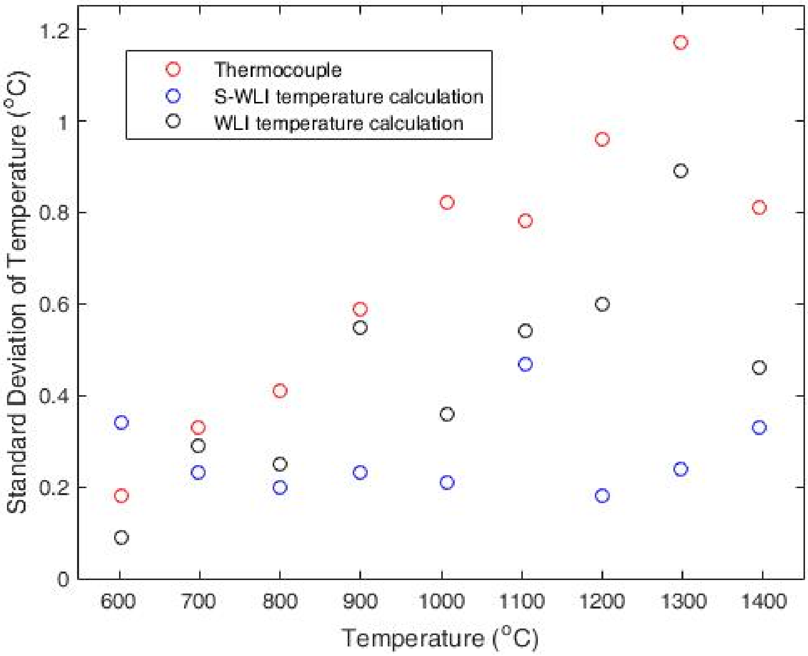

Figure 4-21 Temperature standard deviation comparison between three methods, the thermocouple reading, the S-WLI method and WLI method, separately.

Comparisons between S-WLI and WLI methods are listed in Table 4-3, in Columns 7 and 8. Clearly, both approaches show similar performances. It was observed that at lower temperature, the furnace could achieve better thermal control, both S-WLI and WLI methods show ~0.3ºC temperature standard deviation. We might assume the low temperature performance is a better representation to the optical sensor performance. In this case, the low-cost S-WLI sensor, with 1 second integration time, has a capability to achieve ~0.3 ºC temperature standard deviation. This is good for most of the high temperature applications.

Table 4-3 Comparison between the wafer-based S-WLI and the WLI method.

Mean Temperature (°C)	Zero Pixel Index	OPD (µm)	STD_Pixel (σ_{Pixel})	STD_OPD (σ_{OPD}) (nm)	σT (°C)	($\sigma T_{S\text{-}WLI}$) (°C)	σT_{WLI} (°C)
1396	460.3	134.9474	0.18	1.2	0.81	0.33	0.46
1297	520.9	134.6519	0.12	2.2	1.17	0.24	0.89
1201	579.9	134.3702	0.09	1.5	0.96	0.18	0.60
1105	637.5	134.0981	0.24	1.3	0.78	0.47	0.54
1007	693.9	133.8219	0.11	0.9	0.82	0.21	0.36
899.7	756.9	133.5280	0.11	1.3	0.59	0.23	0.55
799.9	811.4	133.2665	0.10	0.6	0.41	0.20	0.25
698.2	865.3	133.0060	0.11	0.6	0.33	0.23	0.29
603.4	916.5	132.7699	0.16	0.2	0.18	0.34	0.09
508.5	963.4	132.5441	0.16	0.5	0.33	0.34	0.23

4.4 Sourceless Optical Temperature Senor with Focused Light Design

In Chapter 2, we introduce a sourceless fiber optic F-P interferometer, in which the environmental thermal radiation serves as the broadband light source. The sourceless design greatly simplifies the optical structure. Besides, we have improved the performance of a low-cost silica-wafer interrogator by focusing the diverged light to a few lines of the 2-D CCD, to enhance the signal quality. The focused light interrogator thus allows the new S-WLI method to work with relatively weak light, such as in the thermal radiation environment.

4.4.1 Temperature Sensing System

In this section, a sourceless sapphire wafer F-P temperature sensor is investigated. The optical system is built like *Figure 4-22*. The sourcelsss sensor head was constructed as described in Chapter 2.3.1. A sapphire fiber aligns perpendicularly to a sapphire wafer through an alumina tube. A one-end-sealed alumina cap covers the sapphire wafer. The cap generates a stable thermal radiation field at high temperature. When thermal radiation propagates through the sapphire wafer, the directly transmitted light interferes with a portion of light, which reflects twice inside the wafer. Therefore, the sapphire wafer works as the sensing Fabry-Perot cavity. The sapphire fiber, and the multimode fiber spliced after it, guides the coherent light to the interrogator for signal demodulation.

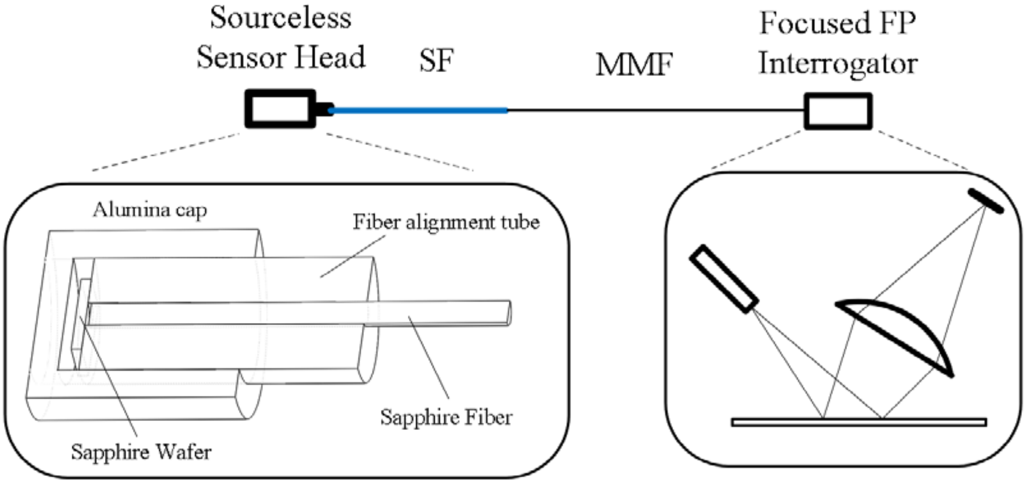

Figure 4-22 Optical system of the sourceless high-temperature sensor.

4.4.2 Temperature Sensor Characterization

We heated the sourceless sensor head in a tube furnace to investigate its sensing performance; with a thermocouple recording the temperature for calibration. Figure *4-23* shows a typical signal acquired at 1400°C. Due to relatively weak radiation power, the original signal is noisier, compared to what is shown in Figure *4-18*. However, the peaks are identifiable after averaging over 20 lines and then smoothing. The highest peak displays apparently stronger than the neighboring peaks. Thus, the strongest peak is identified as the zero-order fringe. Based on Equation (3.35), the fringe contrast is determined by both sapphire wafer F-P cavity and the fused silica F-P interrogator. Since the sourceless sensor head shows a relatively low fringe contrast [1], the overall fringe is weak, calculated to be ~0.019. However, it is still well observable at high temperatures.

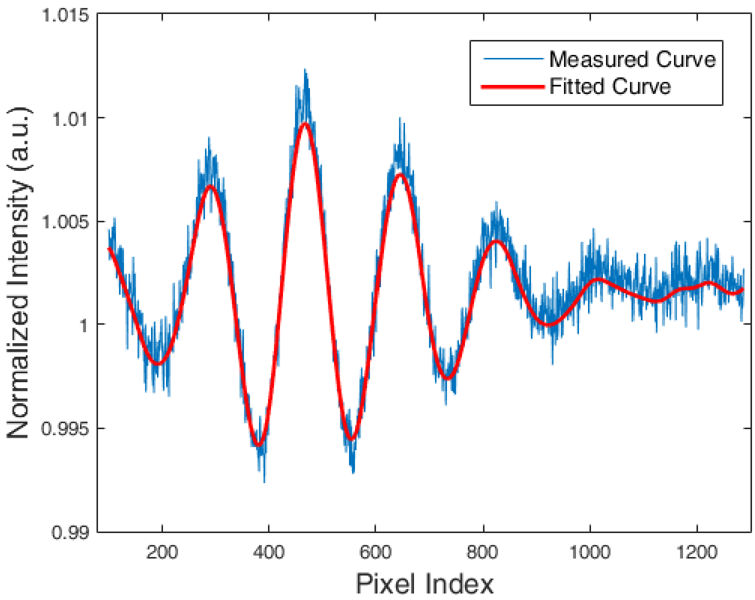

Figure 4-23 Signal of the sourceless sensor system at 1400 °C.

Figure 4-24 illustrates the zero-order peak position vs. temperature calibration curve. It was obtained when cooling the sensor head from 1400°C. Twenty samples were taken at every 100°C step. The light exposure was set to 30 seconds.

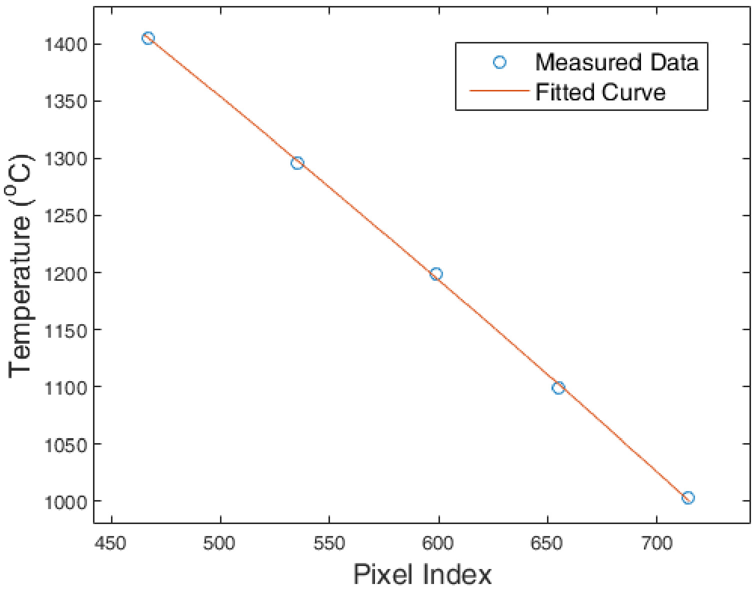

Figure 4-24 Temperature vs. zero-order fringe index calibration curve.

The calibration curve can be described by,

$$T = -0.0003749 \cdot Pixel^2 - 1.189 \cdot Pixel + 2042 \tag{4.13}$$

Once the Pixel position (*Pixel*) was determined by the CCD image, the indicated temperature can be calculated according to the calibration curve. *Figure 4-25* illustrates the pixel position measurements at different temperature levels. The temperature values denoted in *Figure 4-25* are the average temperatures acquired by the thermocouple. The standard deviations of the pixel position are included in *Figure 4-25* as well.

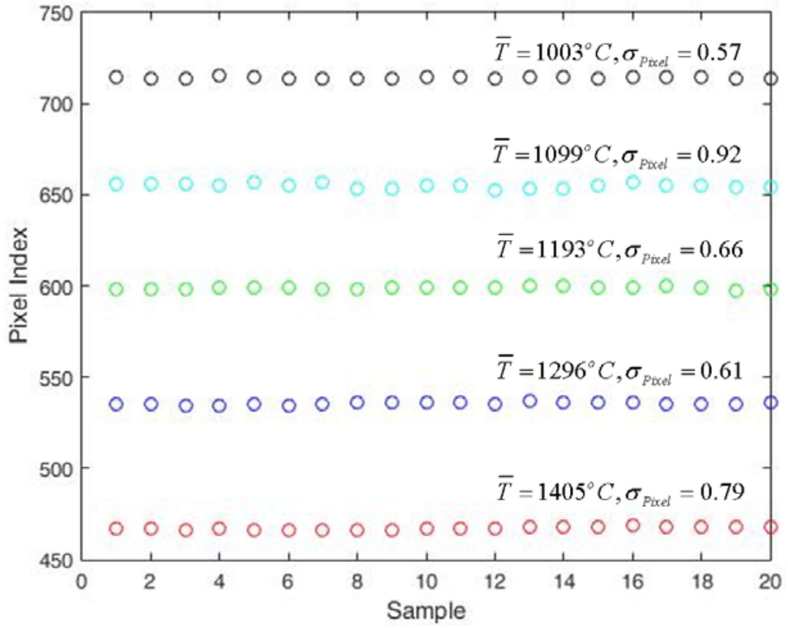

Figure 4-25 Zero-order pixel position at different temperatures.

Figure 4-26 shows the temperatures obtained by a type B thermocouple. The standard deviations (σT) at different temperatures are calculated and noted in *Figure 4-26*.

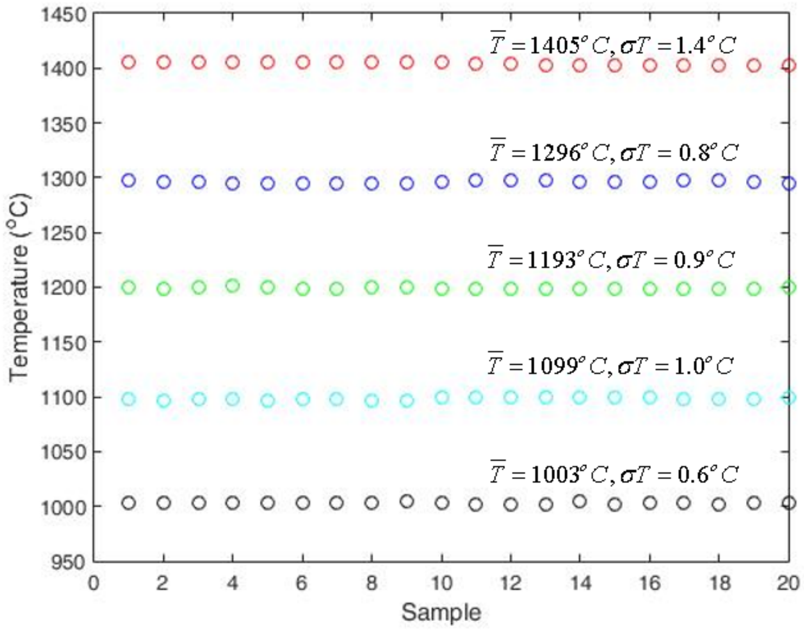

Figure 4-26 Temperature values recorded by the thermocouple and the calculated standard deviations at different temperature levels.

4.4.3 Low-Temperature Sensing Limit

It is a common issue that the thermal radiation intensity, governed by Stefan Boltzmann Law [18], is temperature dependent. The radiation power reduces rapidly as the temperature cools down [1]. Therefore, all radiation-based thermometers have low-temperature limitations, usually hundreds of degrees. In this case, the lower temperature limit of the sourceless S-WLI sensor is defined at the temperature when the signal is so weak that the zero-order fringe is not distinguishable from the neighboring ±1 peak, leading to a fringe order jump. In the setup, at 30 seconds light exposure, jumps were observed at ~900°C.

4.5 Challenges and Future work

To conclude, in this chapter, we introduce a simple wafer-based Fabry-Perot interrogator to demodulate the sapphire-fiber temperature sensor, in which a piece of a thin sapphire wafer functions as the F-P sensing cavity. The interrogator is designed based on the scanning white light interferometry. We make the essential part of the interrogator using the divergence of an optical fiber and a piece of flat silica wafer to achieve a tunable reference F-P cavity, which is required by the S-WLI method.

We successfully acquired the diverged optical interference signal with a 2-D CCD camera. The signal demodulation algorithm shows a good performance. Temperature resolution of better than 1ºC was achieved; similar to the result demodulated by the well-known white light interferometry algorithm.

The optical system was further improved by focusing light reflected from the wafer interrogator to fewer lines of the CCD camera. This approach improves the signal to noise ratio, which potentially allows the system to work with weaker light or responses at a higher speed. With the focused light design, the system achieved better than 1ºC temperature resolution.

We finally combined the two technologies, the sourceless sensor (introduced in Chapter 2) and the low-cost Fabry-Perot interrogator (introduced in Chapter 3) to build a significant low-cost optical sensing system, used explicitly for demodulating solid wafer based F-P temperature working at ultra-high temperatures. Considerable temperature resolution of ~ 1.3ºC was achieved.

Although the technology demonstrates a potentially low-cost fiber-optic temperature sensor system, it is worth noting that the environmental thermal radiation reduces rapidly as the temperature cools down, leading to a low-temperature sensing limitation, which is an issue that all radiation-based temperatures has not solved yet. Besides, the reflection of the reference fused silica wafer is relatively low, approximately 4% in the silica-air boundary, which causes significant power loss at the interrogator and a low fringe contrast of the overall signal.

Future work will focus on further improvement of the system. Depositing thin films on both sides of the silica wafer interrogator to increase the surficial reflection facilitates the collection of the optical power and improve the low-temperature limit. Besides, using an actual 1-D CCD is desirable for a simple optical system and the circuit design. Besides, a professional 1-D CCD for a spectrometer is just $10 in today's market, which is much cheaper than the 2-D CCD camera with similar performance.

4.6 Reference

1. Z. Tian, Z. Yu, B. Liu, and A. Wang, "Sourceless optical fiber high temperature sensor," Opt. Lett. **41**, 195-198 (2016).
2. Z. Yu, Z. Tian, and A. Wang, "Simple interrogator for optical fiber-based white light Fabry–Perot interferometers," Opt. Lett. **42**, 727-730 (2017).
3. M. Gottlieb, and G. B. Brandt, "Fiber-optic temperature sensor based on internally generated thermal radiation," Applied Optics **20**, 3408-3414 (1981).
4. D. P. DeWitt, and G. D. Nutter, *Theory and practice of radiation thermometry* (Wiley Online Library, 1988).
5. F. Shen, and A. Wang, "Frequency-estimation-based signal-processing algorithm for white-light optical fiber Fabry?Perot interferometers," Applied Optics **44**, 5206-5214 (2005).

6. Y. Zhu, Z. Huang, F. Shen, and A. Wang, "Sapphire-fiber-based white-light interferometric sensor for high-temperature measurements," Opt. Lett. **30**, 711-713 (2005).

7. M. N. Polyanskiy, "Refractive index database," https://refractiveindex.info.

8. W. Yim, and R. Paff, "Thermal expansion of AlN, sapphire, and silicon," Journal of Applied Physics **45**, 1456-1457 (1974).

9. G. N. Merberg, and J. A. Harrington, "Optical and mechanical properties of single-crystal sapphire optical fibers," Applied optics **32**, 3201-3209 (1993).

10. Y. Zhu, and A. Wang, "Surface-mount sapphire interferometric temperature sensor," Applied optics **45**, 6071-6076 (2006).

11. M. Han, and A. Wang, "Exact analysis of low-finesse multimode fiber extrinsic Fabry-Perot interferometers," Applied optics **43**, 4659-4666 (2004).

12. Y. Zhu, Z. Huang, M. Han, F. Shen, G. Pickrell, and A. Wang, "Fiber optic high-temperature thermometer using sapphire fiber," in *Proc. SPIE*(2004), pp. 19-26.

13. C. Ma, B. Dong, J. Gong, and A. Wang, "Decoding the spectra of low-finesse extrinsic optical fiber Fabry-Perot interferometers," Opt. Express **19**, 23727-23742 (2011).

14. M. Han, Y. Zhang, F. Shen, G. R. Pickrell, and A. Wang, "Signal-processing algorithm for white-light optical fiber extrinsicFabry-Perot interferometric sensors," Opt. Lett. **29**, 1736-1738 (2004).

15. I. Montvay, and E. Pietarinen, "The Stefan-Boltzmann law at high temperature for the gluon gas," Physics Letters B **110**, 148-154 (1982).

CHAPTER 5 Summary

This dissertation introduces new technologies for development of an ultra-low-cost sapphire-fiber-based high-temperature sensor. The work is divided into two major parts, for solutions toward building low-finesse fiber optical Fabry-Perot-interferometry-based sensors.

The first approach is building a sourceless sapphire-wafer-based F-P temperature sensing system, in which the thermal radiation is used as the broadband light source. It was experimentally proven that the thermal radiation collected from sapphire-fiber sensor head is dominant in the system. Hence, an alumina cap was designed to cover the sapphire-wafer F-P cavity, as to generate a stable radiation field. With this design, a clear optical interference pattern is obtained when environmental thermal radiation propagates through the sapphire wafer F-P sensing cavity. We, therefore, demodulate the temperature by the well known full-spectrum white-light-interferometry algorithm. Temperature resolution better than 1ºC was achieved. The sourceless design avoids using an external light source and its driver, as well as an optical coupler. Hense, the entire optical system is greatly simplified.

A novel approach to demodulate an optical F-P cavity is discussed in Chapter 3. We demonstrated a simple interrogator, which is based on the scanning-white-light-interferometry. In the system, a piece of fused silica wafer, together with a linear CCD array, can transform the F-P demodulation from the optical frequency domain to the spatial domain. By using the light divergence of an optical fiber, we were able to project a variable optical length of a reference F-P onto an intensity distribution along an image sensor array. A model for S-WLI demodulation was established. With a rigorous analysis, we get a deep understanding of the interference signal behavior, especially the fringe-peak generation, and the relationship between the peak position and the OPD of the sensing F-P cavity. The model is validated by experiments. Comparisons between the new S-WLI method and traditional full-spectrum WLI algorithm show a good agreement. Our new design avoids using any moving parts and costly optical components. It provides a good potential to significantly reduce the cost of the widely used S-WLI demodulation algorithm.

At last, the advantages of the sourceless system design and the low-cost F-P interrogator were combined, to make an ultra-low-cost sapphire-wafer F-P temperature sensor. The two technologies were applied to a sapphire fiber sensor. The wafer-based F-P interrogator was optimized by inserting a cylindrical lens between the wafer interrogator to focus light onto the linear image sensor to enhance the signal-to-noise ratio, which allows the interrogator be able to work with low light, especially with the relatively weak thermal radiation. With the help of the focusing cylindrical lens, we achieved a clear optical fringe pattern when the environmental radiation was employed as the light source. Better than 1.3ºC temperature resolution was achieved. By comparing with the result calculated by the traditional WLI method, our proposed S-WLI functions as predicted. The experimental results prove that the sourceless optical sensor and the simple F-P interrogator can work together to build a potentially low-cost optical Fabry-Perot temperature sensors.